THE UNIVERSITY *of* EDINBURGH

This thesis has been submitted in fulfilment of the requirements for a postgraduate degree (e.g. PhD, MPhil, DClinPsychol) at the University of Edinburgh. Please note the following terms and conditions of use:

This work is protected by copyright and other intellectual property rights, which are retained by the thesis author, unless otherwise stated.
A copy can be downloaded for personal non-commercial research or study, without prior permission or charge.
This thesis cannot be reproduced or quoted extensively from without first obtaining permission in writing from the author.
The content must not be changed in any way or sold commercially in any format or medium without the formal permission of the author.
When referring to this work, full bibliographic details including the author, title, awarding institution and date of the thesis must be given.

Photochemical Kinetics and Fluorescence Spectroscopy in Photonic Crystal Fibres

---

Gareth Owen Scott Williams

THE UNIVERSITY *of* EDINBURGH

Doctor of Philosophy by Research

2013

Abstract

This thesis describes work carried out to demonstrate the use of photonic crystal fibres for the study of photochemistry reaction kinetics and fluorescence spectroscopy. Photonic crystal fibre allows the guidance of light, in a well-defined mode, over long path lengths. When the fibre's microstructure is filled with a sample solution this, therefore, provides a greatly increased measurement path length and greater light-sample interaction than is possible in conventional spectroscopic systems, leading to enhanced sensitivity whilst greatly reducing the required sample volumes.

The use of photonic crystal fibre as a micro reaction chamber for carrying out photochemical reactions and the study of their kinetics was achieved through monitoring the photoisomerisation of two azobenzene-based dyes, Disperse Red 1 and Disperse Orange 1, using real-time UV/Vis absorption spectroscopy. Both the 488 nm excitation laser and the broadband light source for the measurements were co-coupled through the fibre, giving perfect overlap of both with the sample. The fibre used for the measurements was a hollow core kagomé-type fibre with a core diameter of 19µm, giving a sample volume of 2.8 nL cm^{-1}. The 30 cm path-length of the fibre allowed the use of sample concentrations down to 5×10^{-6} M, over an order of magnitude lower than in a conventional 1cm cuvette, with a sample volume of 90 nl in the core, a reduction of five orders of magnitude over conventional measurements.

The kinetics of the photoisomerisation from the *trans* to the *cis* isomers of the dyes and the thermally driven *cis*-to-*trans* isomerisation could be tracked on the ms timescale, using a grating spectrometer which recorded the entire absorption spectrum of the dye. The data were numerically fitted using a custom model to take into account the properties of the fibre system. This led to the calculation of rate constants for the isomerisation processes in good agreement with those previously measured for these dye systems in bulk solution. Furthermore, the measurement of the dyes in pentane, in which they are highly insoluble, could be achieved due to the

low concentrations that could be used; such measurements have not previously been reported.

For the study of photonic crystal fibre as a system for the excitation and collection of fluorescence, two types of fibre were used; the same kagomé hollow-core fibre used for the photochemistry absorption measurements and a suspended-core "Mercedes" fibre. This allowed for the excitation of fluorophores in two contrasting environments. In the kagomé fibre fluorophores in bulk solution are excited whilst, in the Mercedes fibre, only fluorophores either on or in close proximity to the silica core interact with the evanescent field of the excitation light. The Fluorescein fluorophore was used initially to measure the detection limits in both fibre types and limits of 2×10^{-11} M in the kagomé and 10^{-9} M in the Mercedes fibre were obtained. This equates to 10^{6} molecules in the kagomé fibre, which displays the lower detection limit due to greater light-sample interaction. Two-photon excitation of the Fluorescein fluorophore was then carried out using a mode-locked Ti-Sapphire laser as an excitation source, demonstrating the ability of the fibre system to sustain two-photon excitation of a long (30 cm) path length. The two-photon measurements showed remarkable detection sensitivity allowing detection of fluorescence from 10^{-9} M solutions of Fluorescein, showing the potential of using PCF for two-photon based experiments which are of particular interest in fields such as photodynamic therapy.

A further study was carried out, using the two fibre types, for measurement of the fluorescence lifetime of the Rhodamine B fluorophore. Unperturbed lifetimes could be measured in the fibres showing no interference from the fibre. The measurements confirmed, in reference to known lifetime values, that in the kagomé fibre the excited fluorophores are in the bulk solution with only a minor influence from surface effects, whilst in the Mercedes fibre all of the excited molecules experience interaction with the surface of the silica core. This, therefore, gives a method of locating the fluorophores with respect to the fibre surface and the ability to choose between measurement of bulk solution and long path-length evanescent field-induced fluorescence.

Declaration

I declare that the work presented in this thesis is my own unless otherwise stated by a reference.

Signed:

Gareth Williams

Acknowledgements

Firstly I would like to thank my supervisor Dr. Anita Jones for taking me on and her tireless, patience, support and encouragement through the course of my PhD. I would like to thank the rest of the Jones group and all of the occupants of office 252, past and present, for making my time enjoyable throughout the highs and lows. In particular I would like to thank Dr. Patricia Richardson for all of her help with experiments and knowledge.

A big thank you to Professor Philip Russell of the Max Planck Institute for setting up the Kroeber project, of which this work was a part, and letting me use the wonderful facilities you have out at Erlangen. And to the rest of the Russell division who made my stays in Germany welcoming and pleasant, thank you. I would especially like to thank Dr (congratulations!) Jocelyn Chen with whom I worked closely in Germany to develop the experimental techniques performed in this thesis, and giving me a huge amount of time and help learning all the new techniques in optics I required.

To all my friends outwith chemistry; Hanna Vesterinen, Samantha Capewell, Mhairi Beaton, Valerie Martinot, Alex Urquhart-Taylor, Nicky Craig, Alasdair Macleod and everyone else (!) my time here would have been so much harder and less enjoyable without the fun, mutual support, and friendship I have enjoyed with you all over the years. Thank you so much.

Lastly for my family who have always supported me in everything I have done, I love you all.

Table of Contents

List of Figures

List of Tables

Abbreviations

CCD	Charged-coupled device
DO1	Disperse Orange 1
DR1	Disperse Red 1
ESM	Endlessly single mode
FACS	Fluorescence activated cell sorting
FLIM	Fluorescence lifetime imaging
FRET	Förster resonance energy transfer
HC	Hollow core
HOMO	Highest occupied molecular orbital
IC	Internal conversion
ID	Inner diameter
IR	Infrared
ISC	Inter-system crossing
LUMO	Lowest unoccupied molecular orbital
MPL	Max Planck Institute for the Science of Light
NA	Numerical aperture
OD	Outer diameter
OPE	One–photon excitation
PBG	Photonic band gap
PCF	Photonic crystal fibre
PSS	Photostationary state
SC	Solid Core
SEM	Scanning electron micrograph
TCSPAD	Time correlated single photon avalanche detector
TEM	Transmission electron micrograph
TIR	Total internal refection
TPE	Two–photon excitation
UV	Ultraviolet

1. Introduction

The development of photonic crystal fibre (PCF) by Professor Phillip Russell in 1996[1], whilst working at the University of Bath, opened up revolutionary new fields of study for the application of optical fibres. The versatile design properties of PCF allows for their use in a wide range of applications, from low-loss communications[2], rivalling traditional fibre designs, to super-continuum generation[3], high power lasers[4] and spectroscopic studies[5]. The latter area is the focus of the work presented here. The unique guidance properties of PCF allow the construction of low loss, hollow core fibres. This provides the ability to perform traditional spectroscopy measurements, such as UV–Vis absorption and fluorescence excitation/detection, from within tiny sample volumes contained within the fibre structure. This work shows that PCF has the potential for providing drastic increases in spectroscopic sensitivity whilst requiring only pico or attomoles of sample. The confinement of light into the fibre allows for near perfect light–sample overlap and interaction at very high power densities, leading to efficient two–photon excitation process being possible over long path lengths, something which is very hard to achieve by any other means.

The work presented was performed as part of a collaborative project setup by Russell after being awarded the European Kroerber prize for his ground-breaking work on the development of PCF. The aim of the project is to find novel applications exploiting the use of PCF in the areas of Chemistry, Physics and Biology. To this end, collaboration between the Russell division at the Max Plank Institute for the Science of Light in Erlangen (MPL) and the Universities of Edinburgh, Bath, Warwick, Cambridge and Queens College London was setup. Each member of the group used PCF to aid the development of new techniques throughout the physical science areas, from in-fibre particle guidance, to in-vivo chemical sensors to chemical reaction chambers. Regular meetings where representatives of all of the groups were present allowed for highly engaging exchange of ideas.

1.1 Outline of Thesis

The following chapters of this thesis will cover the work performed to unitize PCF designs for their application to high sensitivity UV–Vis absorption measurements of a reversible photochemical process. The process studied is the photochemical isomerisation of two azobenzene–based dyes, induced and monitored by pump/probe spectroscopy, from with a hollow core fibre. Further, the one and two–photon excitation of fluorophores in contrasting fibre types is explored, allowing for excitation of molecules in bulk solution and on, or in, very close proximity to a silica surface, with extremely high sensitivity.

Chapter 2 covers the background and theory to the main types of PCF, giving a brief history of its development along with the types of guidance mechanisms they employ. This is followed by the theory behind the photochemistry and fluorescence processes studied in the experiments performed in the later chapters.

Chapter 3 presents development of the application of PCF for the use of photochemistry induced within the fibre core and monitored via UV–Vis spectroscopy. The experimental work for these measurements was carried out at MPL in collaboration with the Russell group, where notably Jocelyn Chen was involved in aiding the development of the experimental setup, through its many iterations, and providing training in the use of the optical components. The calculation of the kinetics of the process was made possible through the detailed knowledge of pump/probe powers and monitored volumes.

Chapter 4 covers the use of PCF to excite and detect fluorescence induced within the fibre structure. The experimental work was carried out at Edinburgh University using a setup inspired by the work used in the photochemistry work at MPL. Both one and two-photon excitation is explored showing the excellent potential of PCF for performing two-photon excitation experiments utilising long path lengths, a typically challenging task. Further, the use of PCF to measure fluorescence lifetimes from molecules within the fibre is presented, which can provide a method to detect both in-fibre temperature and the fluorophore location with respect to the fibre surface.

Finally chapter 5 outlines the main conclusions from the work performed and the extensive further work that can be envisaged for carrying this project forward.

2. Background and Theory

2.1. *Photonic Crystal Fibres*

2.1.1. Introduction to Optical Fibres

The principles behind first low loss optical fibres were developed in 1966[6] and since that time there has been dramatic growth in their application by the telecoms industry as a means of transmitting vast amounts of information around the globe at the speed of light[7]. The introduction of optical communication allowed extremely low signal–loss over long distances, whilst exhibiting very high bandwidth, removing the need for booster stations and multiple traditional copper cables. Whilst a huge step forward from copper–cable communication, the index-guiding nature of the fibres, discussed in chapter 2.1.3, through the use of a silica core surrounded by a lower refractive index cladding, places restrictions on the fibre properties. The core diameter is limited if single mode operation is desired and such fibres exhibit tight guidance cut-off wavelengths, limiting the bandwidth of their operation. Further, the core and cladding must be made of material with equal thermal properties, to prevent fibre damage under temperature change. The requirement for a higher index for the core than the cladding places tight restrictions on the possible fibre compositions and structures for more specialised applications, such as the present work. Transmission through a standard silica fibre also experiences intrinsic loss due to the silica medium. The main contributing factor to the attenuation of signal through a silica core is Rayleigh scattering[8] where light is scattered from in-homogeneities in the core on a scale smaller than the transmission wavelength.

The constraints of traditional optical fibre design have led to the development of a new type of optical fibre known as photonic crystal fibre (PCF). The basic structure of a PCF is the same as a traditional fibre, with a core and cladding; however, both are now made of the same material. The core region is surrounded by a two dimensional silica micro lattice consisting of a set of air filled capillaries which are uniform along the length of the fibre[9]. With only one material present, the problem of thermal, chemical or other compatibility issues between two types of material is immediately removed. A PCF also displays far greater design possibilities, due to

the ability to manipulate the cladding crystal structure to produce a range of refractive index profiles for creating the desired effect. This could be anything from increased non-linearity to birefringence or chromatic dispersion. Further, the structure allows the core itself to be made of a low refractive index material, or indeed to be hollow. The guidance of light through such a hollow core opens up a large range of possible applications, such as spectroscopic studies, like those in this work, as well as the possibility of reducing losses in comparison to conventional fibres.

2.1.2. Development of PCF

The development of this new class of optical fibre took its inspiration from the mechanisms found in nature, where wavelength-scale periodic structures cause high reflectance in specific frequency regions, known as photonic stop-bands[10]. These stop-bands give rise to colours like those found in animals, such as butterfly wings, and plant life, such as the blue iridescence exhibited in the fern-like tropical plants of the *Genus Selaginella* as shown in Figure 2.1. The small scale repeating structures creates a periodic variation in dielectric constant, which interacts with light of similar wavelength to the structures dimensions. This is analogous to the semiconductor band structure in crystal lattices where electrons interact with the periodic variation in potential.

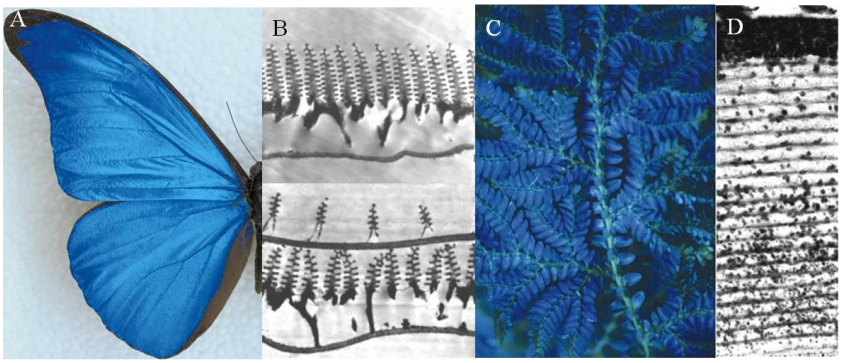

Figure 2.1 Iridescence in the butterfly *Morpho Rhetenor*.(A). Real colour image of the blue iridescence from a *M.rhetenor* wing. (B), Transmission electron micrograph (TEM) images showing wing-scale cross-sections of *M.rhetenor* and the related species *M.didius* reveal its discretely configured multilayers. Structural colour in flora. (C), Blue iridescence from the fern–like tropical plants of the *Genus Selaginella*. (D), TEM section of a juvenile leaf from the plant *Diplazium tomentosum*[10]

One dimensional periodic structures of multiple layers of high and low refractive–index material were fist constructed in the form of Bragg mirrors, planar layers created to reflect specific frequencies through coherent Bragg scattering[11]. The idea of using this structure to confine light in a one-dimensional crystal structure, uniform along the length of a waveguide was first proposed by Melekhin and Manenkov in 1968[12], and Yeh *et al*. in 1978[13], in order to create a Bragg fibre. Such a fibre operates through the resulting radial stop-band which constricts light within the stop-band to the fibre core.

Fibres based on mirrors like these have been produced[14] and utilized for applications such as delivery of high power lasers for endoscopic surgery[15]. The main losses in such a fibre occur through imperfection in the fibre surface reducing the efficiency of the mirrors. A schematic of a Bragg fibre is shown in Figure 2.2

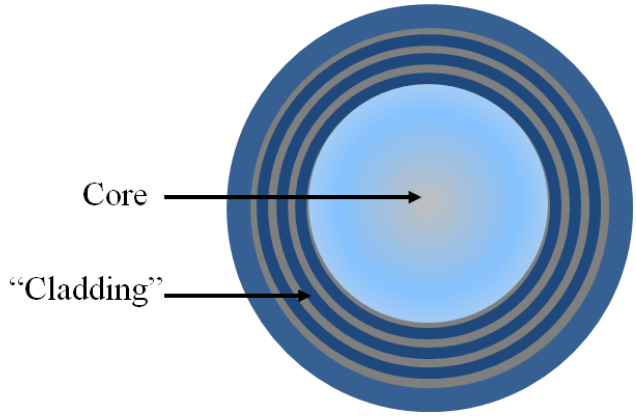

Figure 2.2: Schematic of a brag fibre, the "cladding" is a cylindrical Bragg mirror.

A Bragg fibre cannot be said to guide by the PBG mechanism since photonic states can exist in the cladding of the fibre.

Yablonovitch[16,17] extended this idea to the use of three dimensional photonic crystal structures, where propagation of light in all modes and directions is forbidden for selected frequencies. This blocked wavelength region was termed the photonic band gap (PBG). By having a three-dimensional photonic crystal structure all spontaneous emission is blocked as there are no possible photonic states and light can only propagate through a defect in the crystal structure.

To make use of the photonic band gap as a guidance mechanism a two dimensional structure is required, allowing light to propagate in the third. When a defect is introduced into a photonic crystal slab, featuring periodicity in two dimensions, a waveguide can be formed [18]. In two-dimensional photonic crystal slabs, light propagates via the band–gap effect in the plane of periodicity, and via index guidance perpendicular to this plane. A schematic of such a slab is shown in Figure 2.3.

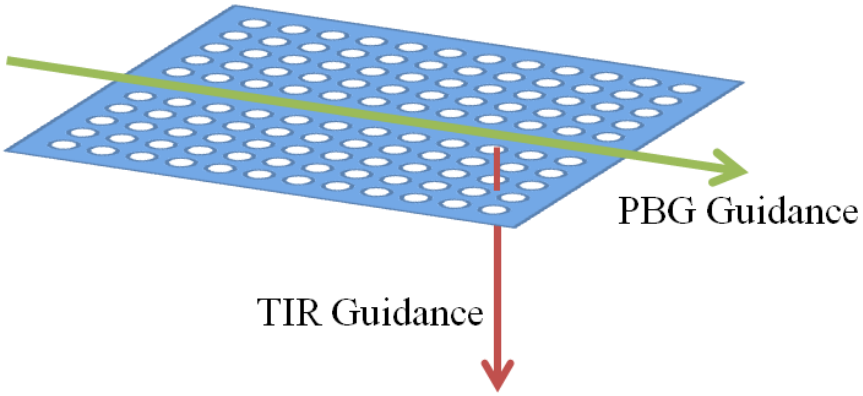

Figure 2.3: Schematic of a two-dimensional, silica, photonic crystal slab, showing guidance via the band gap mechanism through a defect in the plane of the crystal structure, and TIR guidance normal to the slab.

In contrast to this, in a photonic crystal fibre the light propagates via the PBG mechanism at the normal to the plane of periodicity. The effect this has on the guidance properties of the fibre can be explained by considering the Bragg law for constructive interference given in Equation 2-1

$$m\lambda = 2\Lambda cos\theta \qquad \text{Equation 2-1}$$

where m is an integer, λ is the wavelength, Λ is the pitch of the crystal structure and θ is the angle of incidence to the surface. For a photonic crystal slab, where $\theta = 0$, this implies that to act as a waveguide, Λ must be on the order of λ. In contrast, for a PCF, where light enters at a grazing angle to the surface, Λ can be much greater than the wavelength of light. Because of the requirement for such a small and precise pitch of the crystal structure in a slab compared with a PCF, the PCF structure is the better choice for constructing low loss optical waveguides.

Construction of the first PCF was reported by Russell *et al.* in 1996[1]; the fibre was a solid-core, index-guiding PCF, utilizing a two-dimensional photonic crystal where the structure is periodic in the plane perpendicular to the fibre guidance axis but invariant along the fibre length. From this initial development further exotic fibre types were explored, such as endlessly single-mode (ESM) fibres[19], and highly non-linear fibres, capable of effects such as broadband super–continuum generation[21]. A brief overview of the development of PCF and notable applications for this work are shown in Table 1.

PCF Development	**Developed**
First solid-core PCF[1]	1996
Endlessly single-mode PCF[19]	1997
PCF with photonic band-gap guidance through an air core[20]	1999
Super-continuum generation within PCF[21]	2000
Laser-tweezer guidance of particles in HC–PCF core[22]	2002
First suspended core fibre[23]	2002
PCF fabricated from high index tellurite glass[24]	2003
First demonstration of Kagomé structure HC–PCF[25]	2006

Table 1 : Historical development of PCF and its applications.

MPL and others are now able to produce fibres with tailored characteristics for novel applications such as those presented in the current work.

2.1.3. Types of Optical Fibre

2.1.3.1. Conventional Optical Fibres

Conventional optical fibres work on the principle of guidance by total internal reflection at the interface between two materials. To provide similar thermal and chemical resistance properties, fibres are usually constructed from two types of glass, a pure silica core and a doped silica cladding, reducing the refractive index of the latter[26]. At the boundary between two materials of differing refractive index, light will be refracted away from or towards the normal to the interface, depending on whether the index increases or decreases. A decrease in refractive index will cause the light to bend away from the normal to the interface[27]. If the sum of the angle of incidence to the interface and the degree through which the light is perturbed by the interface is greater than 90 degrees the light will effectively be reflected, this is known as total internal reflection (TIR). If this sum is less than 90 degrees the incident beam will bend away from the normal but still pass through the interface. This principle is governed by a simple relationship, Snells Law, given in Equation 2-2

$$\frac{\sin\theta_1}{\sin\theta_2} = \frac{v_1}{v_2} = \frac{n_1}{n_2} \qquad \text{Equation 2-2}$$

where $\theta_{1,2}$ are the angles between the incident light and the reflected/refracted light and the normal to the interface, $v_{1,2}$ are the beam velocities and $n_{1,2}$ are the refractive indices of the materials.

Figure 2.4 shows schematically how light behaves at the interface between two materials with different refractive indices.

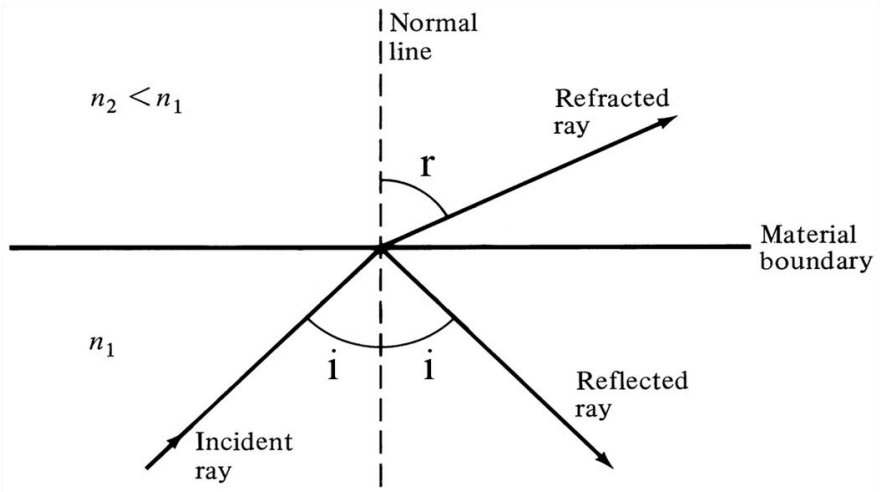

Figure 2.4: Behaviour of a beam of light at an interface between materials of differing refractive index. Where i is θ_1 and r is θ_2.

This imposes the constraint that light entering an index guiding fibre has to enter at an angle below that required for total internal reflection to occur, known as the acceptance angle or numerical aperture. Any light entering the fibre from above this angle will not be guided. This is shown schematically in Figure 2.5

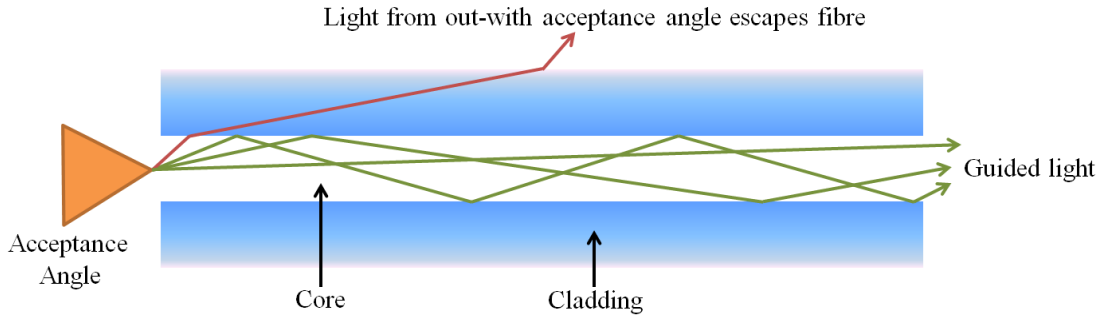

Figure 2.5: Schematic of a light guidance through a traditional optical fibre.

The further and more important limitation of this type of optical fibre, in the context of this thesis, is the requirement for the core region to have a higher refractive index than the surrounding regions. This means that the core generally has to be a solid, limiting its application for spectroscopic study to evanescent wave detection. For construction of fibres with different core types more exotic structures are required.

2.1.3.2. Photonic Crystal Fibres

Due to the nature of a photonic crystal fibre, the mechanism through which it guides and the properties that can be produced through changing the lattice structure are very wide ranging. The main guidance mechanisms of index guidance and photonic band-gap guidance will be discussed along with types of fibre that can be produced that utilize them.

2.1.3.2.1. Index Guiding Photonic Crystal Fibres

With an index guiding PCF, the fibre structure consists of a solid silica core surrounded by a lattice of air holes in silica in a hexagonal pattern that run uniformly along the length of the fibre[28]. An example of an index guiding solid core PCF (SC-PCF) is shown in Figure 2.6. The presence of the cladding holes reduces the effective refractive index of this region and, therefore, light is guided by a modified internal reflection mechanism through the high index core, similar to that of a conventional optical fibre.

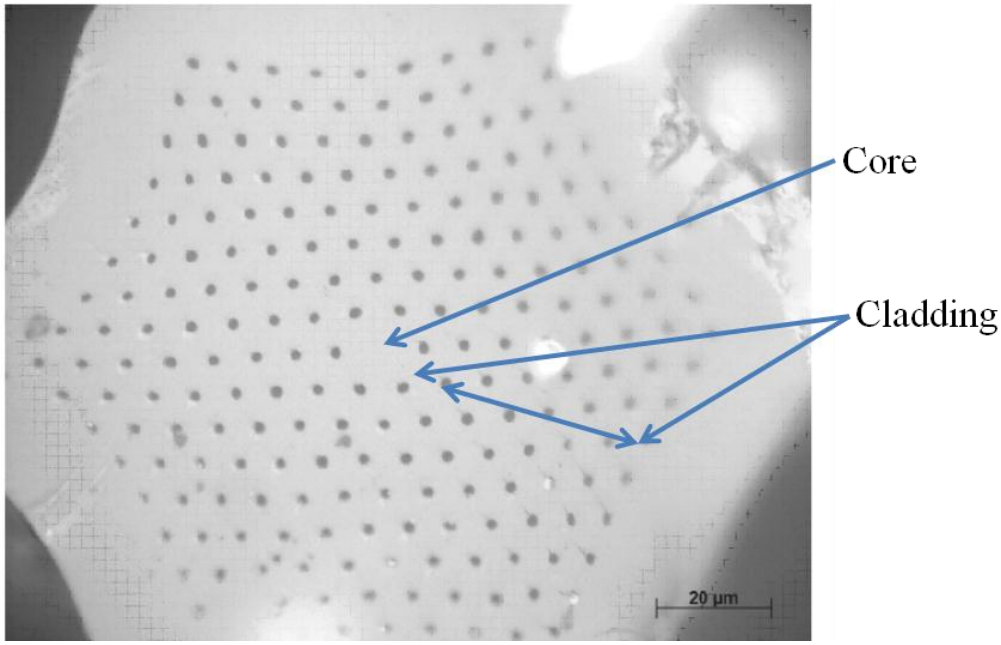

Figure 2.6: Scanning electron micrograph of an example structure of an index guiding PCF, the central silica core is surrounded by a silica–air lattice.

A schematic of such a fibre, showing how the refractive index changes across its cross section, is shown in Figure 2.7.

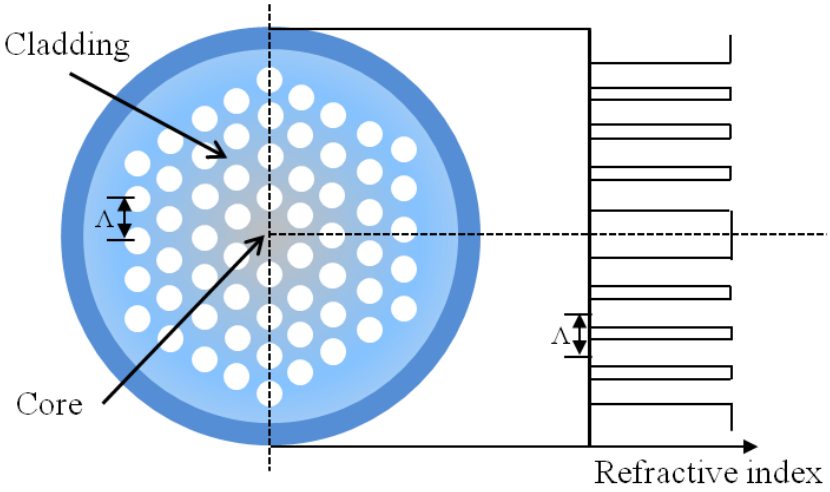

Figure 2.7: Schematic of a silica/air index guiding PCF (right) with the refractive index profile shown on the left for a slice through the fibre (dotted line).

This type of fibre construction can be used to create fibres with many useful properties through varying the size of the cladding holes relative to the silica struts between them. These properties are not possible to achieve in a conventional fibre where the cladding is a uniform material.

The first type of fibre produced with this structure was one that exhibits endlessly single-mode guidance, known as an ESM fibre[19]. The core of such a fibre traps the fundamental mode of the guided light, which has dimension of ~2 Λ. Higher order modes, which have smaller lobes than the fundamental, can escape through the silica struts between the air holes in the cladding. These higher order modes, therefore, exhibit very high losses and are quickly removed over a short length of fibre. The fibre will only operate in this single mode as long as the relative size of the cladding holes to the silica struts between them, d/Λ, where d is the size of the holes, is small enough that the higher order modes can propagate through the silica and escape. Increasing the size of the holes, decreasing the size of the silica struts, will trap increasingly higher order modes. ESM fibres are especially useful as a means for spatially and modally filtering differing light sources and this feature is exploited through the experimental work presented here.

A second, highly utilised type of index guiding SC-PCF takes advantage of the very high core–to–cladding refractive index contrast, which can lead to very tight modal confinement and therefore very low mode areas. This can give rise to non-linear

effects more than two orders of magnitude higher than in conventional fibres allowing them to be used for applications based on nonlinear optics such as ultra-broadband super–continuum generation[29], which can then be used as a spectroscopic light source. The effect can be increased even further by constructing the fibre from a material that has an intrinsic high non-linearity such as bismuth silicate[30] or lead silicate[31,32] glasses.

Through the development and tuning of the cladding hole pitch, size and shape in solid core index guiding PCF, the guidance losses can now be made comparable with conventional fibres, exhibiting losses as low as 0.18 dB km^{-1} at a wavelength of 1.55 μm being reported[33].

2.1.3.2.2. Suspended Core Fibre

A different approach to the index guiding is found in a suspended core fibre[34]. In this case, a small silica core is suspended within a large capillary by thin silica micro-struts. An example of such a fibre is shown in Figure 2.8. These fibres are the most similar in guidance to a conventional optical fibre as the air region around the core is of lower refractive index than the core itself. The supporting micro struts are too thin to support the guidance of light and therefore light is effectively confined to the core.

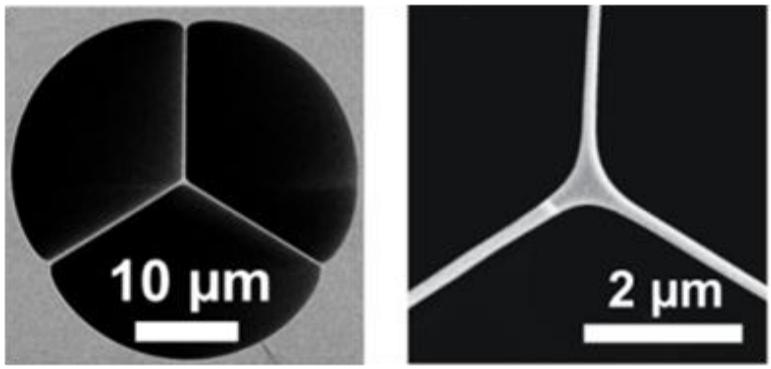

Figure 2.8: Scanning electron micrograph of suspended core fibre produced at MPL with an effective core radius of 0.55 μm.

Due to the distinctive three pronged appearance of this fibre structure it is often referred to as a "Mercedes" fibre.

2.1.3.2.3. Band-Gap Guiding PCF

The fibre structures considered so far cannot accommodate a hollow core, since their guidance mechanism is still one of reflection on index change. For the construction of a hollow core fibre, a guidance mechanism such as band-gap properties of a photonic crystal must be exploited.

Hollow-core waveguides existed since before the invention of the hollow–core PCF (HC–PCF). These waveguides confine light through either attenuated total internal reflection[35] or by using a reflective metallic surface, known as known as leaky guides[36]. Both of these methods inherently lead to fibres that are multimodal and subject to very high losses, particularly bending losses. This means that only short waveguides of these types can be used[37]. HC–PCF[20] can alleviate these problems and allows tailored guidance over long distances. Whilst the guidance in HC–PCF is also inherently multimode, due to the large core diameters supporting multiple guided and surface modes, single mode operation can be often achieved through the careful in-coupling of light to only excite the fundamental core mode. Because higher order modes usually exhibit far higher losses than the fundamental mode[38], single mode operation can be achieved by using a longer length of HC–PCF or by simply bending the fibre, which induces greater losses, again more so for higher order modes.

As mentioned above, for a PCF to have a hollow core, the guidance can no longer be through total internal reflection, as the core cannot be of lower refractive index than the surrounding cladding. Guidance can be achieved through the exploitation of photonic band gaps as discussed in section 2.1.2, which for specific frequency regions are forbidden to propagate in the cladding crystal. Through the cladding structure, a two-dimensional photonic crystal, a photonic band gap is created for each of these frequency regions, and, therefore, low–loss guided modes can be formed in the core, a defect in the crystal structure. Fibres such as these are known as photonic band-gap photonic crystal fibres (PBG–PCF). The structure of the cladding for a hollow-core PBG–PCF (HC-PBG–PCF) is, in general, a honeycomb of thin silica struts and air holes, where there is an approximately 80% air to silica fraction. An example of a HC-PBG–PCF is shown in Figure 2.9[39]. This is the first type of fibre

that allows for the possibility of in–fibre spectroscopy measurements on bulk solutions such as those reported in this thesis, and permits the guidance of light over long distances with very low attenuation. To date losses as low as 1.2 dB km^{-1} have been reported for fibres of this type[40].

The main remaining limitation of HC-PBG–PCF with this structure is the restricted frequency range that can be guided by any given fibre due to the specific band gap created; this is typically in the 100 nm bandwidth range.

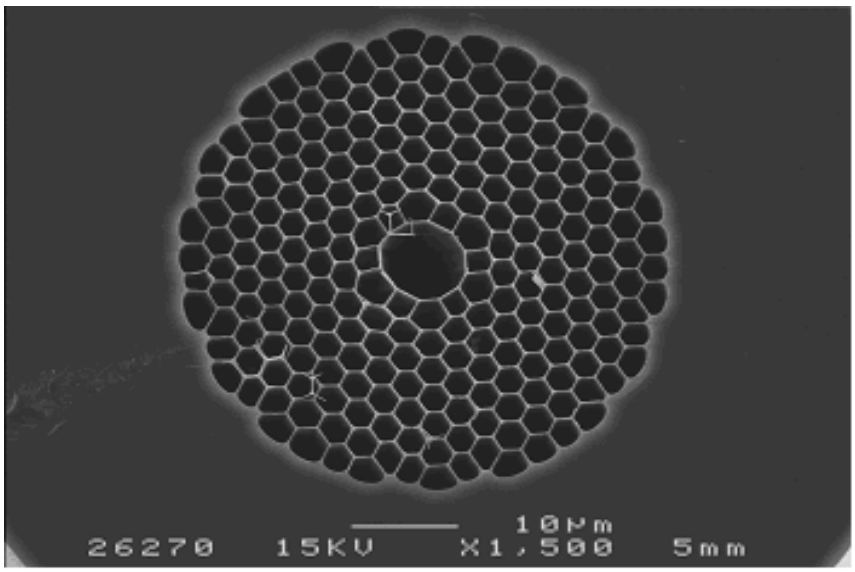

Figure 2.9: Scanning electron micrograph of a typical HC-PBG–PCF[39].

2.1.3.2.4. Kagomé PCF

A final class of two-dimensional PCF has been introduced more recently, known as a kagomé lattice PCF[25]. These fibres consist of a cladding microstructure in the form of a kagomé array constructed from a thin silica lattice. Fibres of this type show good guidance of light, over far larger spectral ranges than with HC-PBG–PCF, although the mechanism displayed is not that of a photonic band gap, such as described above for PBG–PCF. There have been several proposals regarding the guidance properties of these fibres[41,42,43,44], with the latest suggesting guidance is through interaction between core and cladding modes[45]. A complete understanding of

the guidance mechanism is still lacking. With kagomé PCF there are always propagating fields allowed in the cladding, and therefore resonances can appear between core and cladding modes. As a result, the guidance of core modes is dependent on a complex interaction with the cladding and surrounding media making them appear more like Mie-resonances than simple modes[38]. The core diameters of fibres of this type are also, in general, larger than those of PBG-HC–PCF which leads to multiple modes being supported. As a result the losses in kagomé PCF are higher than that of HC-PBG–PCF with the lowest reported loss[46] of 0.18 dB m^{-1}. Whilst higher than a HC-PBG–PCF this is still far better than capillary guidance which will be discussed in section 2.1.5. With the larger guidance band and reasonable guidance losses, this is the best fibre type developed to date for allowing spectroscopic measurements from within the fibre. The microstructure of a kagomé PCF is shown in Figure 2.10.

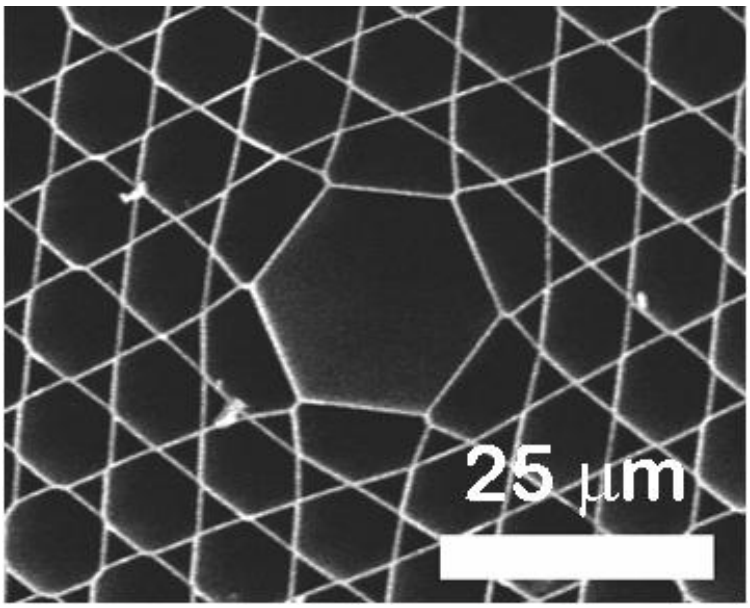

Figure 2.10: Scanning electron micrograph of the microstructure of a kagomé PCF

2.1.4. Fabrication

The most common method for the construction of PCF is the stack-and-draw technique. The initial stack is built up on a macroscopic scale, using capillaries which have a ratio of inner to outer diameters (ID/OD) that will match the air filling

fraction and design required for the final fibre. This stack of capillaries, which are typically around a meter long, having a diameter of a few centimetres, is then inserted into a large outer jacket, which will hold them in place during the drawing process. The stack is then placed on a drawing tower and drawn through a furnace, reducing its diameter to a few millimetres. This produces what are known as preforms. A schematic of the fabrication process is shown in Figure 2.11.

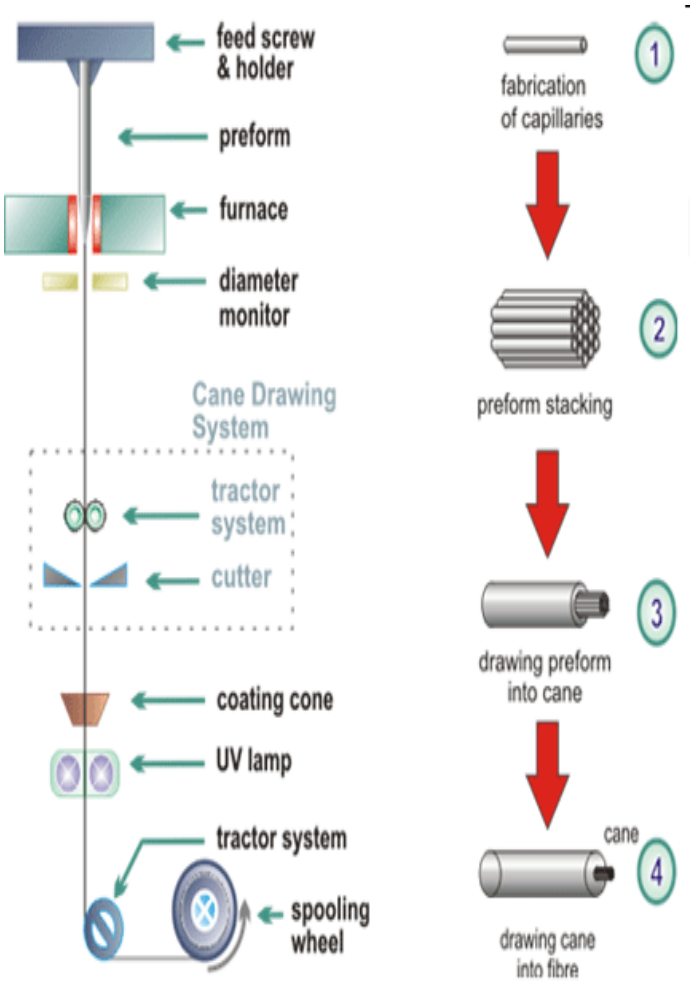

Figure 2.11: Schematic of the stack and draw technique for fabrication of PCF, courtesy of Jocylen Chen at MPL. The left side shows the fibre drawing tower where the preform, or cane, is placed above a furnace through which it is drawn to a precise diameter. Following final drawing a polymer coating is applied and treated with UV light before the fibre is collected on a spool.

The preforms are then drawn again, either into the final fibre dimensions, or, if a large scale reduction is needed, they undergo further drawing stages with the intermediate stage producing "canes". This second drawing process is required for the small-featured fibres such as HC–PCFs. The cane and final fibre structures are

shown in Figure 2.12 for a typical HC–PCF, courtesy of Jocylen Chen at MPL. Once a fibre has been drawn to its final dimensions, it is coated with high quality polymers that are cured with ultraviolet (UV) light to provide mechanical robustness.

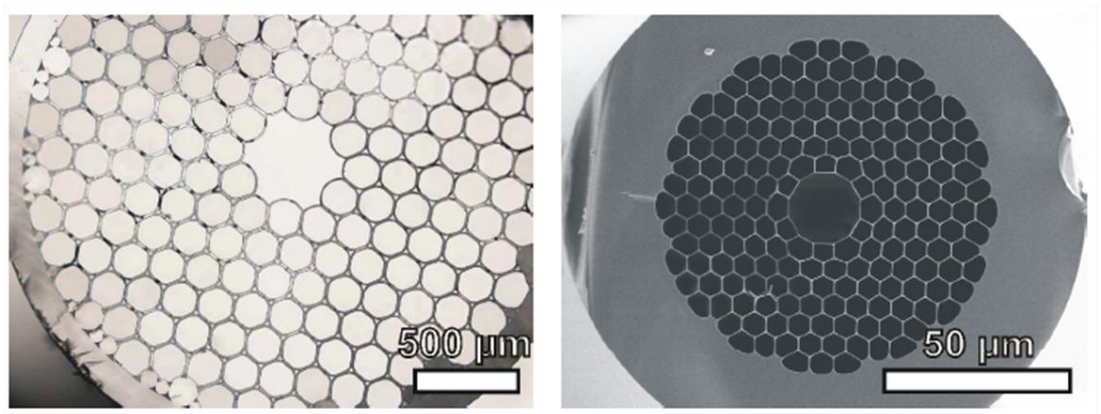

Figure 2.12: (A) Optical micrograph of the cross section of a cane to be drawn into a HC-PBGPCF. (B) SEM showing the cross section of the HC-PBG–PCF drawn from the cane. The large silica ring present is the jacket into which the original capillaries were placed. The dimensions of the cane diameter and final fibre cladding structure are 2.6 mm and 60 µm respectively.

This fibre fabrication technique has been implemented and improved upon and now fibres are produced with highly complex cross sectional structures which are maintained near perfectly over kilometres of fibre, with a typical stack producing several km of usable PCF.

There are several other techniques, including extrusion[31], for fabricating PCF, mainly applied when low melting point glass is being used. As all of the fibres used in this work are made from pure silica, the stack–and–draw method was used throughout. This was performed by the fibre fabrication team at MPL, each fibre being produced to the specification required for guidance over the spectral ranges appropriate for the measurements of absorption and fluorescence.

2.1.4.1. Post Fabrication Fibre Processing

After the fibre has been drawn it is ready to be characterised and used for many applications. There are, however, further modifications that can be made in order to increase the potential of the fibres for specific applications such as improving the

application of PCF to lab–on–a–chip micro–opto–fluidic systems. The main technique used is femtosecond laser ablation[47] which is used to "drill" channels from the side of a PCF permitting selective access to the fibre core. This then allows for the direct injection of a sample into the fibre core from an external microfluidic circuit, which could be used for sample preparation, and then extraction into another device for further, non-optical, analysis. Whilst not applied to the fibres used in this work, its future application could see further reduction in dead volumes and tighter integration with micro–fluidic systems. Though this provides a means for direct injection into the fibre core, pre–filling the whole fibre including the cladding structure with a solvent would be required, to preserve the fibre guidance mechanism. This is due to the increased refractive index of solvents over air, the effect of which will be discussed in section 2.1.6. An example of using laser ablation to produce a thin channel into the side of a PCF, fabricated at the Max Plank Institute is shown in Figure 2.13.

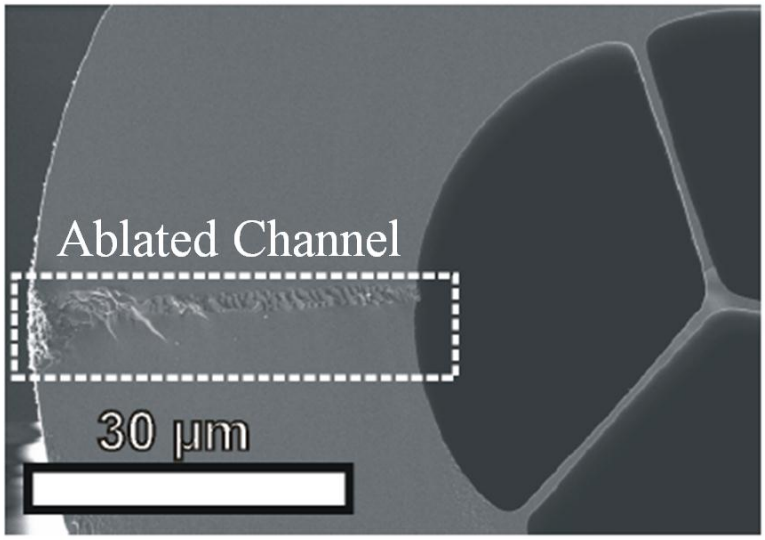

Figure 2.13: SEM of a micro-channel drilled using femto-second laser ablation allowing access to one of the three cladding holes of a suspended core fibre.

2.1.5. Comparison of PCF to Conventional Sample Cells

The most important features of a sample cell for bulk solution spectroscopic measurements are its path length, cross sectional area and volume.

An increase in the cell path length (D (cm)) allows for lower concentrations to be used in absorption measurements such as UV–Vis spectroscopy, where the absorbance of the sample is governed by the Beer-Lambert Law, given in Equation 2-3, which will be discussed in section 2.2.2.

$$A(\lambda) = \epsilon(\lambda)cD \qquad \text{Equation 2-3}$$

where ϵ is the molar absorption coefficient of the sample in L mol^{-1} cm^{-1} and c is the concentration of the sample in mol L^{-1} (M).

An increase in path length of an order of magnitude therefore allows an order of magnitude lower concentration to be measured.

For a conventional cuvette, increasing the path length requires a large increase in the volume of sample required. A 10 cm cuvette, requiring 10 mL of sample, is the longest path length commonly used. To reduce this volume requirement the cell cross section has to be reduced. The smallest cuvettes used in conventional spectrometers are 1 mm × 10 mm × 10 mm, so use of other cell designs is needed to increase the path length. The cross-sectional area (a) of the cell is important as it defines the total power needed to provide the required power density to the sample. Further a reduction in cross–section provides a smaller sample volume, assuming that the whole cell cross–section is irradiated. This is particularly important for processes with very low quantum yields, or absorbance cross section such as two photon processes. As the cross–sectional area is reduced the power density for a given input power is increased, therefore minimising this area is desirable to increase the total power density achievable.

As the path length of the cell is increased and cross sectional area decreased the confinement of the probe light through the sample must be maintained. The mechanism through which this is achieved, along with sample absorption, will reduce the transmitted intensity. As the sample concentration can always be reduced,

the maximum length of a cell is defined by its inherent losses as given by Equation 2-4

$$D_{max} = \frac{1}{\alpha_{cell}(\lambda)}$$ Equation 2-4

where $\alpha_{cell}(\lambda)$ is the propagation loss through length L of a sample cell.

Hollow capillaries can be used to reduce the effective cross section down to 10s of μm and therefore allow the use of low volumes. However, simple capillaries provide poor confinement of light with attenuation of a perfectly straight hollow capillary α_{cap} governed by Equation 2-5for beams propagating in EH_{nm} modes with $n \neq 0$[48] such as the fundamental Gaussian mode.

$$\alpha_{cap} = (\frac{u_{nm}}{2\pi})^2 \frac{\lambda^2}{r^3} \frac{(\nu^2 + 1)}{\sqrt{\nu^2 - 1}}$$ Equation 2-5

where u_{nm} governs the mode of the propagating light, r is the capillary core radius, and $\nu = n_2 / n_1$ the ratio of the cladding to core refractive index of the capillary. Capillaries are also very sensitive to bending reducing the length that can easily be used.

HC–PCF, due to its superior guidance properties over a capillary, allows very small core sizes along with long path lengths to be utilised. The kagomé fibre used throughout the majority of this thesis displays transmission losses 175 times lower than the equivalent capillary and therefore, in principal, a path length 175 times longer can be used. This long path length, along with the low cross-sectional area and therefore sample volume per cm, ~2.8 nL, makes the HC–PCF an ideal sample vessel for low volume optical absorption measurements.

At long path–lengths further losses are also present through the inherent interaction with the guided light and the solvent within the cell. These losses are due to both solvent absorption and scattering, and whilst generally small compared to guidance losses and sample absorption they will affect ultimate sensitivity of the detection system. In other long path–length systems such as cavity ring down spectroscopy where the light path passes through the sample multiple times to increase the eddective path length the same losses are observed.

A summary of the comparison between cuvettes, capillaries and HC–PCF is shown in Table 2.

Sample cell type	a (cm^2)	D_{max}(cm)	Volume (mL)
Cuvette 10 mm × 10 mm × 10 mm	1	1	1
Cuvette 1 mm × 1 mm × 10 mm	10^{-2}	1	10^{-2}
Glass capillary with 19 μm core	2.8×10^{-6}	0.49	1.4×10^{-6}
Glass capillary with 100 μm core	7.9×10^{-5}	71	5.6×10^{-3}
Kagomé HC–PCF with 19 μm	2.8×10^{-6}	86	2.4×10^{-4}

Table 2: Comparison between various types of sample cell and a kagomé HC–PCF using a 488nm laser

For other spectroscopic measurements, for example fluorescence measurements on bulk solutions, the benefits of PCF over the other sample cell designs are even greater. In order to measure fluorescence from a bulk solution both efficient excitation of the fluorophores and collection of the emitted fluorescence are required. The above discussion on absorbance is equivalent to the excitation process in a fluorescence measurement; however, the collection of emitted fluorescence is typically very inefficient in traditional spectrometers. In such a system a cuvette is generally used and a lens system is used to collect emission perpendicular to the excitation beam. Typically less than 10% of the isotropic fluorescence emission is collected. The use of PCF allows very small volumes to be excited within the fibre and then the excellent guidance properties of the fibre can be tailored to efficiently couple the emitted fluorescence, and guide it along the fibre length with low loss, where it can then be detected. This increased collection efficiency along with the very small core area, allowing tight focusing of excitation light, provides very high irradiances. PCF is, therefore, a particularly advantageous sample chamber for the study of two-photon induced fluorescence, compared with the conventional arrangement in which a laser is tightly focused into a bulk sample. In the latter case, only an extremely small fraction of the sample is excited, greatly increasing the

challenge of florescence collection. A further process that has to be taken into consideration when increasing the path length of a sample cell for fluorescence measurements is reabsorption of guided emission though further interaction with the sample, this will be discussed in detail in section 2.3.1.1.

2.1.6. Liquid Filled PCF

In order for a PCF to be used as a reaction system for the spectroscopic study of liquid systems, the effect of the increase in refractive index over that of a gas has to be accounted for in the waveguide design. The main factor that affects whether the waveguide will work when filled with a liquid is the guidance mechanism that is employed.

For liquid-filled index guiding hollow-core waveguides there is the requirement for a higher refractive index core than the cladding. Although possible, this provides very limited material choice for the construction of the fibre, as few solids have a refractive index lower than that of common solvents such as water. As water is the typical basis for most biological systems this limitation makes pure index guiding fibres a far from ideal choice.

One way to produce an index guiding fibre that allows the use of liquids, such as water, is to use a solid core PCF with the solution infiltrating the air holes of the cladding, such as those shown in Figure 2.6 and Figure 2.8. Whilst the index contrast between core and cladding is reduced, the silica core is still of higher index than the solution, with a suitable choice of solvent. With this fibre type the reduced index contrast reduces the optical confinement to the core, and in-coupling conditions are greatly restricted due to a far lower acceptance angle. As the light is still guided by the same core region, however, the spectral transmission is very similar to the unfilled fibre, perturbed only by absorption peaks due to the infiltrated solution. The loss of such a fibre is wavelength-dependent, as longer wavelengths will have a greater interaction with the sample medium and are less confined within the fibre core.

Whilst these solid core fibres are effective, the overlap of the guided light is only through the evanescent field and, therefore, sample light interaction is limited to 10s of nanometres around the core, in the cladding holes immediately surrounding it. Also, due to the very large surface area of the fibre, the effect of the sample interaction with the silica surface may be high. To increase overlap between the sample and guided light, and reduce surface effects, the most desirable solution is a hollow-core fibre.

As discussed in section 2.1.3.2.3, HC–PCF guides by a PBG mechanism, however transmission properties of such a HC–PCF are not independent of the refractive index of the medium filling the fibre structure. As the effective index contrast between the core and cladding changes, the band-gap that is produced will be affected. Filling the fibre with liquid will shift the band-gap of the fibre to lower frequencies[49]. Whilst not trivial, since the refractive index properties are still accurately known, the effect of a change in the index of the medium infiltrating the fibre on the position of the band-gap can be assessed. Work carried out by the Max-Planck Institute showed that the shift in the transmission spectrum for a HC-PBG–PCF could be described by an index scaling law[50]. This law is derived from a scalar approximation of the vector wave equation describing the transverse electromagnetic field distribution in a PBG fibre. The work showed that when the low refractive index material in the construction of a PBG–PCF, the material in the cladding holes/core, with index n_2 is changed to n_2', whilst the high refractive index part, in this case the silica lattice, is unchanged, the central wavelength, λ_0, of the band-gap is shifted to $\acute{\lambda}$ given by Equation 2-6

$$\acute{\lambda} = \lambda_0 \left(\frac{1 - N^{-2}}{1 - {N_0}^{-2}} \right)^{1/2} \qquad \text{Equation 2-6}$$

where $N_0 = n_1/n_2$ is the initial fibre index contrast, in this case an air-filled fibre, and $N=n_1/n_2'$, the index contrast of the desired fibre, in this case a water filled fibre.

Whilst only strictly true for small index contrast this relationship can still provide qualitative results for the large effective index contrasts that can be present in PCF. For kagomé type fibres, which do not technically guide by the photonic band gap

effect, Equation 2-6 does not hold quantitatively, but can still give qualitative prediction of the effect of solution infiltration. This expression can therefore provide an extremely useful guide for the design of PBG or kagomé-type HC–PCF for guidance of light over specific frequencies that coincide with ranges of interest for the study of a solution-phase sample. For example, for a PBG–PCF where the desired measurement region is around 650 nm, in a water solution of refractive index of 1.33, the fibre has to be designed to guide at 1.2 μm when empty. This is important if PCF is going to be used as an optical sensing system for photochemical reactions, UV/Vis and fluorescence spectroscopy, or other optical techniques where liquids are involved.

2.1.6.1. Filling PCF with Liquid

The process of filling a PCF with a liquid solution is non-trivial due to the sub-micron dimensions of the structure of the fibre. Different fibre geometries and the connections between filling apparatus and the fibre result in different liquid flow which can produce vastly different filling behaviour, such as required pressure for infiltration and probability of bubble formation. It is therefore important to have knowledge of the process of liquid infiltration to allow optimisation of the liquid cells used to introduce the sample to the fibre and pump rates and durations required to fill a fibre consisting of varying sizes of features.

The simplest micro-fluidic environment for liquid flow is a single straight capillary[51], study of which allows comparison between the different sized cladding and core holes of a PCF. Liquid within such a capillary experiences four forces, from the capillary itself, gravity and any pressure overhead or pumping involved[52]. A schematic of such a capillary and the related forces is shown in Figure 2.14.

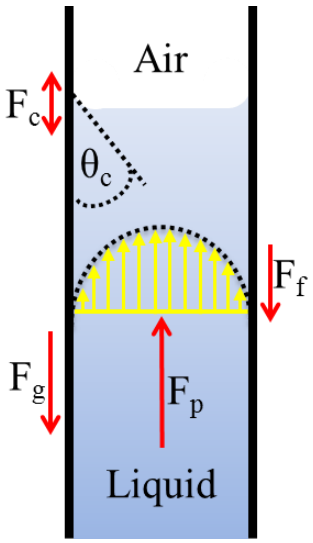

Figure 2.14: Forces acting on a liquid flow within a capillary, F_g force due to gravity, F_p force due to pumping or pressure head, F_f force due to friction and F_c the capillary force. The effect of the friction and capillary forces causes Poiseuille flow within the capillary indicated by the yellow arrows. For $\theta_c < 90^o$, the capillary force will pull the liquid into the capillary; for $\theta_c > 90^o$, the force will push the liquid out of the capillary.

In order to calculate the filling properties of such a capillary the sum of all these forces has to be computed. The capillary force, F_c, for a circular capillary, is given by Equation 2-7

$$F_c = 2\pi a\sigma cos\theta_c \qquad \text{Equation 2-7}$$

where a is the radius of the capillary, σ is the interfacial tension of the liquid and θ_c is the contact angle between the liquid and capillary wall. The Reynolds number (*Re*) determines whether the liquid flow will be turbulent, $Re \gg 2300$, or laminar, $Re \ll 2300$, is given by Equation 2-8

$$Re = \frac{2\rho a v}{\mu} \qquad \text{Equation 2-8}$$

where ρ is the liquid density, ν is the velocity and μ is the dynamic viscosity of the liquid. For capillaries of the dimensions found in PCF a typical Reynold's number is of the order of 10^{-2} which implies that the liquid flow inside such a fibre will be laminar.

The frictional force F_f for such a flow is given by Equation 2-9

$$F_f = -8\pi\mu L v \qquad \text{Equation 2-9}$$

where L is the length of the liquid column within the capillary. The force exerted by a pump or pressure overhead F_p is given by Equation 2-10

$$F_p = \Delta P \pi a^2 \qquad \text{Equation 2-10}$$

where ΔP is the applied pressure difference between the liquid column and the open end of the capillary. Finally the gravitational force, F_g is given by the usual expression shown as Equation 2-11

$$F_g = -\pi\rho g a^2 L \qquad \text{Equation 2-11}$$

where ρ is the liquid density and g is the gravitational constant.

The total force on the liquid column can be calculated by balancing these four forces which yields the differential equation over time of

$$\frac{d}{dt}(\rho\pi a^2 L v) = 2\pi a\sigma cos\theta_c + \Delta P\pi a^2 - 8\pi\mu L v - \pi g\rho a^2 L \qquad \text{Equation 2-12}$$

which can be solved for a horizontal fibre to give Equation 2-13,

$$L(t) = \left(\frac{A}{B^2}\exp(-Bt) + \frac{At}{B} - \frac{A}{B^2}\right)^{1/2} \qquad \text{Equation 2-13}$$

Where the constants A and B are given by,

$$A = \frac{4\sigma cos\theta + 2\Delta P a}{\rho a} \qquad B = \frac{8\mu}{\rho a^2}$$

Simulated infiltration lengths over time for several capillaries of different radii, 1, 5 and 10 μm as a function of time, using water and a pressure of 1 bar are shown in Figure 2.15, clearly showing the dependence of filling rate of a capillary on the radius.

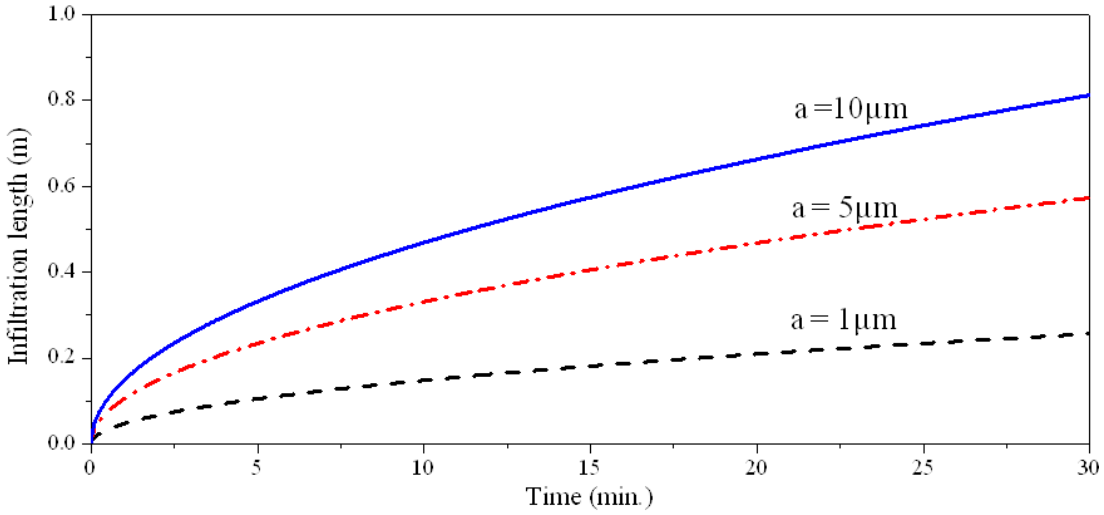

Figure 2.15: Simulation of infiltration of water into all silica capillaries of radii 1μm (dash), 5 μm (dash-dot) and 10 μm (solid) at 1 bar. The physical parameters for water at 20°C used were $\Theta_c = 0^o$, $\sigma = 72.88$ m Nm^{-1}, $\rho = 988$ kg m^{-3} and $\mu = 1$ cP.

In the case of a HC–PCF, the larger core will be filled before the smaller holes of the cladding microstructure. Care therefore has to be taken, when filling a HC–PCF, that sufficient time is allowed for the whole structure to be infiltrated, not just the core region, as unfilled cladding holes affect the guidance mechanism of the fibre. When the core is completely filled, whilst the cladding holes are empty or only partially filled, the fibre becomes effectively index guiding, due to the higher refractive index of the liquid compared to the effective refractive index of the cladding. Under these conditions, the large index contrast and the relatively large size of the core means that the fibre guidance will be highly multimode, making it extremely difficult to in-couple into the fundamental mode of the fibre. This is undesirable as it leads to unpredictable light coverage of a sample within the core, and the higher losses associated with higher order modes.

Whilst there have been attempts to calculate and design a liquid core fibre with single mode guidance, where the cladding remains empty[53], the dependence of the cladding design on the wavelength and index contrast make this approach impractical. Standard HC or kagomé HC–PCF must, therefore, always be filled for long enough to ensure complete infiltration of all the cladding holes, approximately 45 minutes for 30 cm of kagomé fibre. After the initial filling, samples can be added or changed in the time taken to fill only the core, as long as care is taken not to

introduce bubbles to the system. This greatly reduces the time between reference measurements and sample measurements to approximately 10 minutes. Care must be taken to avoid bubble formation in the liquid cells used to pump fluid into the fibres and any other tubing and pumping hardware as the introduction of a bubble into a cladding hole will necessitate infiltration for a further 45 minutes to force the bubble through the length of the fibre.

2.1.7. Transmission Properties of Kagomé HC–PCF

The structure of the kagomé fibre used in the presented work is shown in Figure 2.16.

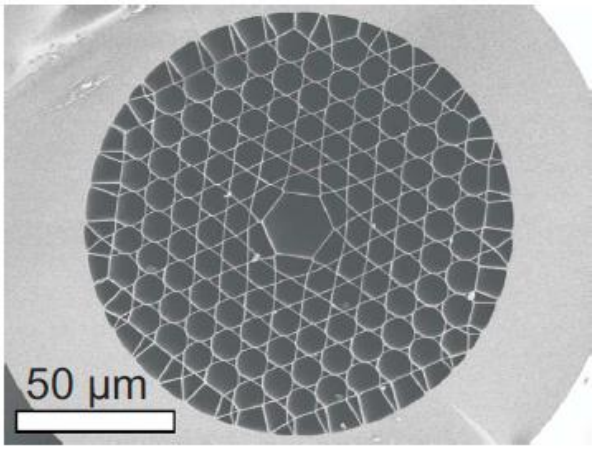

Figure 2.16: Kagomé fibre used throughout the measurements in this work.

The transmission spectrum of this fibre, whilst empty, normalised to the super-continuum source, is shown in Figure 2.17. This was measured by Joceyln Chen at The Max Planck Institute.

These measurements were made using the cut-back method, where the power transmitted through a long piece of fibre, in this case 4 m, is normalised to that of a shorter length, here 1.1 m, of the same fibre whilst not changing the in-coupling conditions. It can be seen that the air filled fibre shows good guidance over the wavelength range of 500 to 960 nm. Due to normalization through the cut–back method and to the original super–continuum a transmission of -10 dB m^{-1} in figure 2.17 equates to an actual loss of 2 dB m^{-1}. DB is defined as $10\log(\frac{P}{P_0})$ and so for the

transmission window there is 63 % transmission per meter. The inserts of Figure 2.17 show the transverse irradiance profiles measured from the output of the fibre, confirming that fundamental mode guidance was achieved throughout this wavelength region. The spectrum shows guidance loss peaks in the between 900 and 1210 nm. These correspond to the coupling between surface states and resonances with the cladding struts which reduces guidance efficiency.

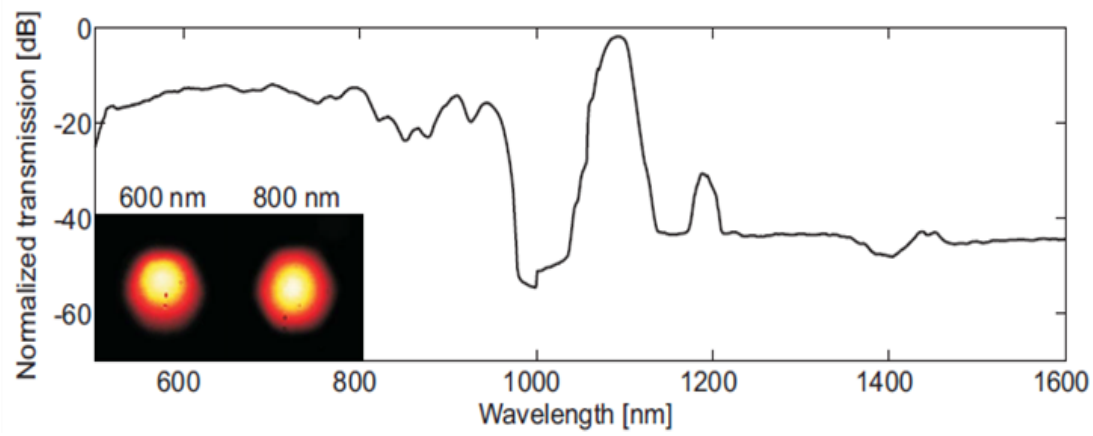

Figure 2.17; Transmission (normalized to the super-continuum source) spectrum of the kagomé HC–PCF. Inset: measured transverse irradiance profiles after 4 m of the fibre at λ = 600 and 800 nm.

The fibre was designed to have a transmission window centred between ~450 nm and 500 nm when filled with water, to allow for the absorption spectra of the analytes of interest, in commonly used solvents such as water, to be observed. As discussed previously the guidance mechanism of a kagomé HC–PCF fibre is not via the PBG mechanism and therefore the scaling law to calculate the effect of solvent infiltration cannot be quantitatively applied. However, it is still expected that the guidance band will shift to lower wavelength upon filling. Therefore, appropriate scaling of structural properties during fabrication of a fibre with a known guidance band in air allows the required guidance wavelength range to be achieved. The transmission profile of the kagomé fibre when infiltrated with water is shown in Figure 2.18.

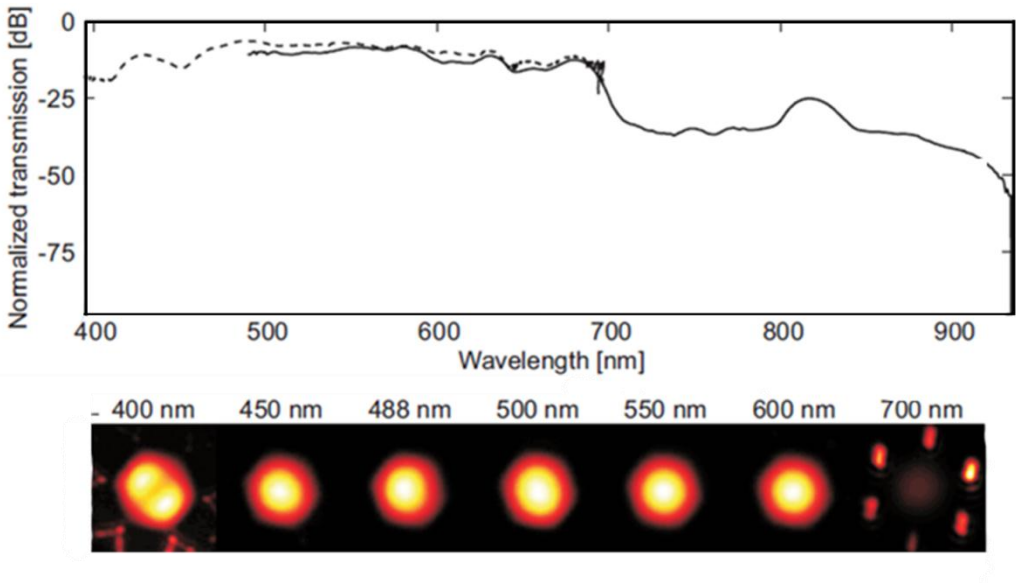

Figure 2.18: Transmission spectrum of the kagomé fibre when fully infiltrated with de-ionised water. Two super-continuum sources were used as the original source (solid line) did not cover the low wavelength end of the transmission band (dotted line). Below are shows transverse irradiance profiles over the guidance band from 400-700 nm.

Since the lower edge of the conventional super-continuum source that was used occurred at approximately 450 nm a second source was needed to measure the lower end of the kagomé transmission band, the dotted curve in Figure 2.18. The kagomé fibre can be seen to have broadband guidance over approximately 400–700 nm with good fundamental mode transmission between 450 and 600 nm. The higher order modes shown at 400 nm can, however, be explained by chromatic aberrations in the coupling objective as this was optimised for 550 nm for experiments before and after this one. Further optimisation of the measurement system for 400 nm showed fundamental guidance at this wavelength. At wavelengths above ~650 nm there is clear indication of coupling of core modes into surface cladding modes of the cladding struts surrounding the core. However, as the absorbance spectra of the dyes measured in this work and the fluorescence emitted from the chosen fluorophores range from 400–600 nm the fibre is ideally suited.

2.2. Photochemistry of Azo-Benzene Based Dyes

The photoisomerisation of azobenzene from the *trans* to *cis* isomer has been studied in great detail for over 70 years[54], making it one of the most studied systems in chemistry. Azobenzene was first used as the basis for a range of photochromic or photoswitchable azo–dyes. These azo–dyes have long been used as dyes and colorants[55], but more recent applications seek to exploit the ability to reversibly photoswitch the geometric, electronic and optical properties of the molecule. Such applications include memories and switches in new electronic and photonic systems[56,57], optical control of various physical properties of materials[58,59] and optically switchable components in molecular machines[60] and biomolecules[61]. Measurement of the kinetics of azo–dye isomerisation is central to the design and optimisation many these applications. The molecule is characterised by the azo group (-N=N-) linking the two benzene rings. Further, constituents attached to the benzene rings affect the ability of electron transfer through the molecule and the relative energy of the *trans* and *cis* states. This allows the strong electronic absorption region to be tuned via the combination of different functional groups. The molecule undergoes readily induced photoisomerisation which is rapid, reversible and of high quantum yield.

The following sections will cover the absorption of light by matter, the physically measured parameters for absorption spectroscopy, the principal mechanisms for molecular isomerisation, the photochromism and photoisomerisation of azobenzene and related dyes and the kinetic analysis of this process.

2.2.1. The Absorption of Light by Molecules

The following discussion is based on previously presented work by Tait[62] along with the texts of P. Atkins[63] and J. R. Lakowicz[64].

The electrons of all molecules exist in a state of discrete, quantised, energy levels known as electronic energy levels. These are the most widely spaced set of energy levels and relate to the molecular orbitals the electrons are occupying. Within these levels exist further bands of discrete energy levels related to the vibrational frequencies of inter-atomic bonds and molecular rotations. Due to this quantisation of the energy of electrons in atoms and molecules, only specific frequencies of light can be absorbed or emitted, matching the energy of a transition between two states. For transitions between electronic states the required energies are usually in the ultra-violet to visible (UV–Vis) regions of the electromagnetic spectrum, and for closer spaced vibrational and rotational transitions in the infrared (IR) and microwave regions. Furthermore, electronic transitions can only occur if the amplitude of the transition moment integral, the integral of the electric dipole moment between the initial and final states, or the square of the overlap integral of the wave-functions, is non-zero. This reduces the number of allowed transitions that can take place.

For an electronic transition, absorption of a photon can excite a range of vibrational states, allowing a small bandwidth of transition energies for each electronic transition. The vibrational states that can be accessed are governed by the Franck–Condon Principle. This principle is outlined as follows. Firstly, the nuclei of atoms are many orders of magnitude heavier than the surrounding electrons and therefore their relative motion is far slower. This is known as the Born-Oppenheimer approximation. The absorption of a photon of light takes place on the time scale on the order of femtoseconds (fs = 10^{-15} s) which is faster than the motion of the nuclei, and so they can be assumed to be stationary during excitation. As the nuclei remain fixed, the electronic transition is, therefore, vertical from the electronic ground state (S_0), to a vibrational state of an electronic excited state, for example S_1. A transition of this type is represented in Figure 2.19 showing the transition from S_0, v=0 to S_1, v'=3 in a diatomic molecule. The intensity of the transition is proportional to the square of the overlap integral between the vibrational wavefunctions. This leads to a

characteristic absorbance spectrum of lines for a molecule. For more complex polyatomic molecules there are a large number of possible transitions which merge together leading to an absorbance curve, described as the Franck–Condon envelope.

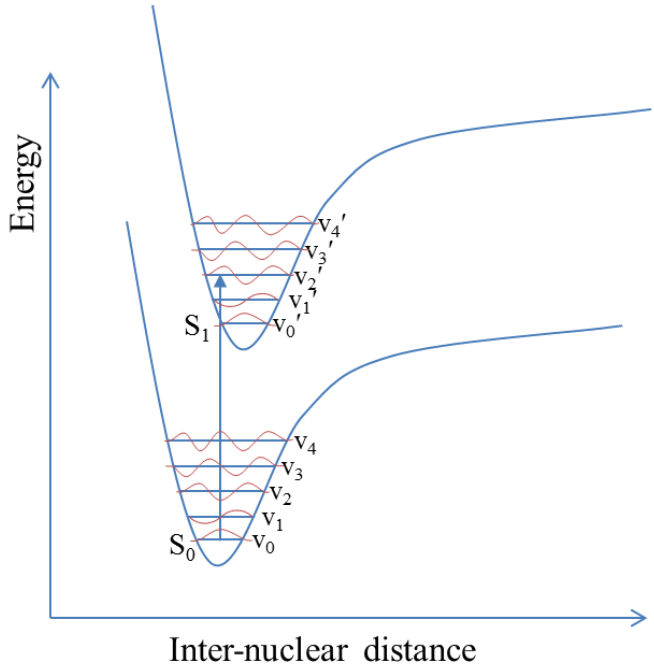

Figure 2.19: Representation of the Franck-Condon principle for a diatomic molecule. Due to the relatively massive nuclei their motion is assumed to be zero during an electronic transition giving a vertical transition between vibrational states with the greatest wavefunction overlap. Vibrational wavefunctions are shown in red.

The frequency of the photon required to produce a transition, equal to the energy difference between the two levels, is given by Equation 2-14

$$\Delta E = h\nu \qquad \text{Equation 2-14}$$

where *h* is the Planck constant and ν is the frequency of the light.

For most organic compounds, including the azobenzene derivatives that have been studied in this work, the absorption bands are due to the excitation of a single electron from an n or π orbital to a π^* orbital. The transitions have absorption peaks in the region of 200-700 nm, the UV–Vis region, which allows for the convenient experimental measurement of the spectrum by conventional UV–Vis spectrometers.

2.2.2. The Beer-Lambert Law

As mentioned in section 2.2.1 the absorption of light by a sample can be defined by measurable experimental parameters. Because a molecule has a statistical probability of absorbing a photon of light depending on its wavelength, known as its absorbance cross section, there is a linear relationship between the number of molecules exposed to an excitation source and the observed absorbance value. This relationship between the absorbance and absorber density is known as the Beer-Lambert law, as previously stated in Equation 2–3,

$$A = \varepsilon c L$$

where ε is the wavelength dependent absorption coefficient of the absorber (also known as the extinction coefficient) in cm^2 $molecule^{-1}$, c is the molar concentration of the absorber molecule and L is the path length over which the measurement is carried out. ε is related to the absorbance cross section σ (cm^2), the likelihood that at a specific wavelength the molecule will absorb a photon of light by

$$\sigma = \frac{1000\varepsilon}{\mathrm{N_A}} \ln(10) = 3.82\mathrm{x}10^{-21}\varepsilon \qquad \text{Equation 2-15}$$

Secondly, the transmission through a sample is defined as

$$T = \frac{I}{I_0} = 10^{-\varepsilon c L} \qquad \text{Equation 2-16}$$

Where I_0 is the incident light intensity and I is the intensity after the sample. Absorbance can therefore be linked to transmittance by

$$A = -log_{10}T = -log_{10}\frac{I}{I_0} \qquad \text{Equation 2-17}$$

After excitation, several processes can occur, some of which are directly observable, such as fluorescence and phosphorescence, and others such as quenching which can only be observed indirectly. When the outcome of an absorbance event is observable the quantum yield, which defines the efficiency of a photo–induced event can be defined as

$$\Phi = \frac{Number\ of\ photo-induced\ events}{Number\ of\ photons\ absorbed} \qquad \text{Equation 2-18}$$

The processes that can occur following absorption that are of interest to this work will be discussed in the following sections; 2.2.3 for photoisomerisation and 2.3.1 for all other decays.

2.2.3. Photoisomerisation Process

Photoisomerisation occurs when the electronic excitation of a molecule, induced by a photon of light, produces a structural change between two isomers of a molecule. The most common examples are of rotation around a C=C or N=N double bond, taking the molecule from the *trans* to the *cis* isomer, or vice-versa.

The simplest system in which to study the energy levels involved is ethene, two sp^2 carbon atoms double bonded with two hydrogen atoms per carbon. In the ground state the molecule exists in a planar form, with rotation around the double bond leading to an increase in potential energy up to a local maximum energy at 90^o due to π orbital overlap. A schematic of these potential energy levels, as a function of torsional angle around the C=C bond, producing the described potential energy curves is shown in Figure 2.20.

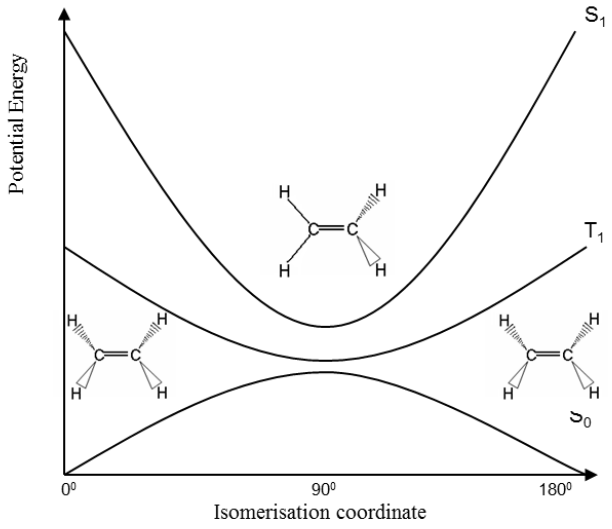

Figure 2.20: Relative energy levels for the ground state (S_0), first singlet (S_1) and first triplet (T_1) exited states.

The absorption of a photon of sufficient energy will cause an electron to be excited from the highest occupied molecular orbital (HOMO), in this case a π orbital, to the lowest unoccupied molecular orbital (LUMO), in this case the π* anti-bonding orbital. The excited state is therefore known as the ππ* state. In this excited state, which can be either the first singlet (S_1) or first triplet (T_1) state, there is now an electron in an anti-bonding orbital, which leads to a reduction in the bond order of the carbon double bond. This change in order causes the minimum energy configuration to now lie at a rotation around the C=C bond of 90°, as this minimises the interaction between bonding and anti-bonding orbitals. Due to the close proximity of the minimum of the excited state potential energy curve and the maximum of the ground state curve, internal conversion (discussed in section 2.3.1.2), or intersystem crossing (discussed in section 2.3.1.3), can occur to the S_0 ground state. The system can then relax in either direction, to its original form, or rotated by 180°.

2.2.3.1. Azobenzene

In the case of azobenzene and it derivatives, such as Disperse Red 1, shown in Figure 2.21[65], where functional groups are attached to the phenyl rings, the centre of rotation is around the -N=N- double bond. This is analogous to the -C=C- bond in ethene.

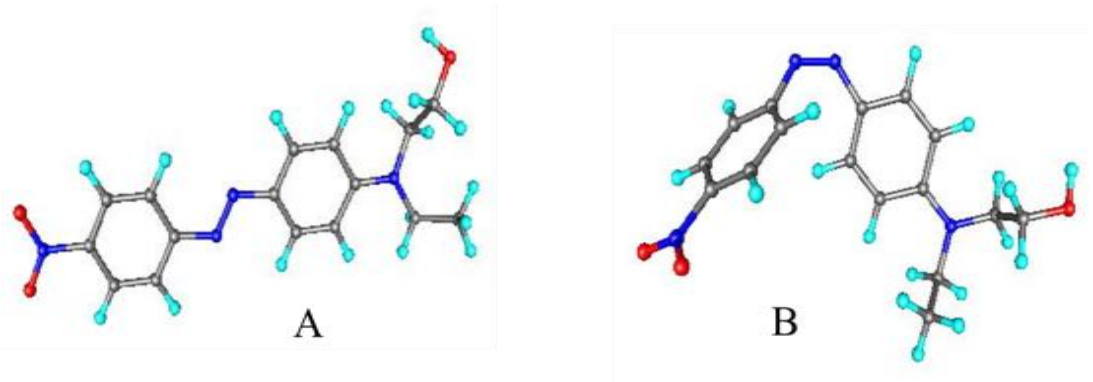

Figure 2.21: Molecular structure of azobenzene derivative Disperse Red 1 in for the *trans* (A) and *cis* (B) isomers[65].

After photo-excitation the molecule can, therefore, theoretically form two stable, or meta-stable, states, the *trans* and *cis* isomers. Due the greater delocalisation of the π-electrons in the planar *trans* isomer, the molecule is in a lower energy state in this form.

A simplified energy level diagram for the photoisomerisation of azobenzene derivatives is shown in Figure 2.22. Once excited into an excited state the molecule passes through a *transition state* (TS), and relaxes to either the to the *trans* or *cis* forms. Molecules in the *cis* form can then be either excited again by further absorption of a photon, or relax thermally to the more stable *trans* form.

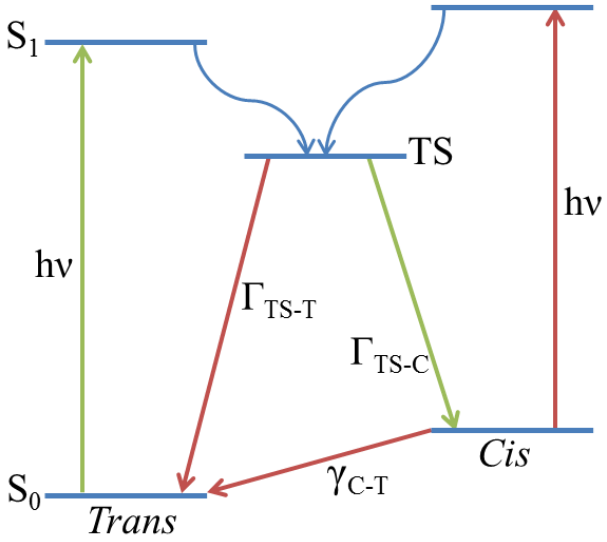

Figure 2.22: Simplified diagram of the isomerisation processes for azobenzene and its derivatives, showing excitation energy (hυ), non-productive relaxation rate (Γ_{TS-T}), isomerisation rate (Γ_{TS-C}) and thermal isomerisation rate (γ)

The mechanism through which the isomerisation occurs for both the photoisomerisation and the thermal isomerisation processes has been greatly debated[66,67,68,69,70,71,72,73,74]. The discussion centres on whether there is a rotation or inversion pathway involved, as depicted in Figure 2.23[67]. The most recent studies point towards the pathway involved being dependent on the state to which the molecule is excited, with isomerisation from the S_1 state being predominately through the rotation mechanism and from the S_2 through inversion.

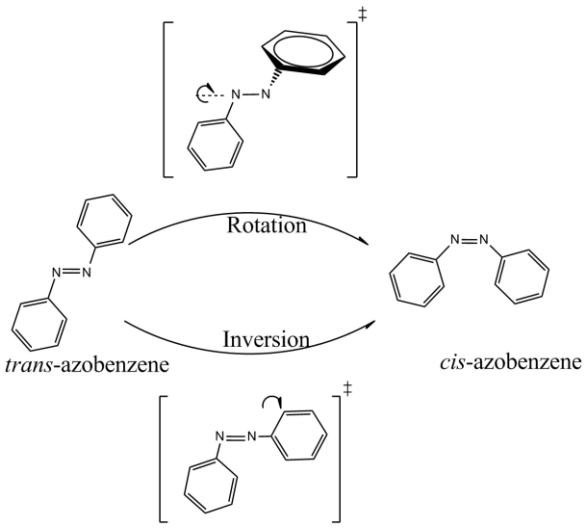

Figure 2.23: Rotation and inversion pathways for the isomerisation of azobenzene.

The combined processes of photoisomerisation from *trans* to *cis* and *cis* to *trans* along with the thermal isomerisation from *cis* to *trans* lead to a dynamic process when under constant irradiation. When starting from dark, all molecules are in the *trans* form, and excitation will cause photoisomerisation to the *cis* form. After time the rate of *trans* to *cis* isomerisation will be matched by that of the *cis* to *trans* and the system has reach what is known as the photostationary state (PSS), where the overall composition of the system is no longer changing.

An energy diagram for the azobenzene based dye, Disperse Red 1, analogous to Figure 2.20 for ethane, is shown in Figure 2.24[66].

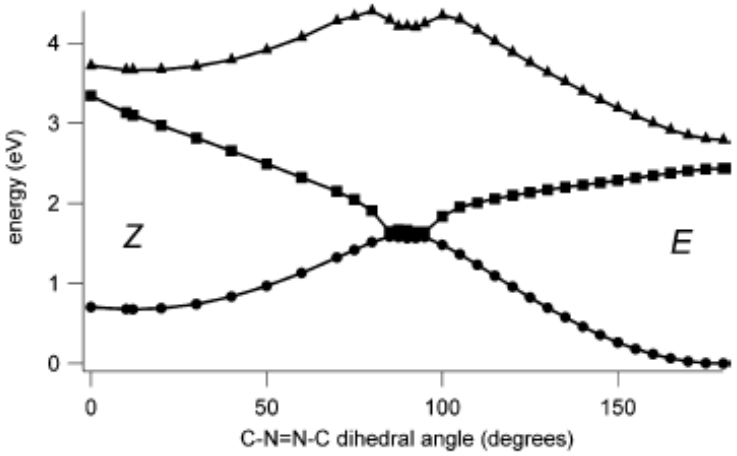

Figure 2.24: Energy level vs rotation about the azo linkage for the ground state S_0 and two exited states S_1 and S_2, Z: *cis* isomer, E: *trans* isomer for Disperse Red 1[66]

The energy barrier for direct, or thermal, isomerisation from the *trans* to the *cis* form is of the order of 150 of kJ mol^{-1} whilst the barrier for conversion of the *cis* to the *trans* isomer is around 80 kJ mol^{-1}. Dokić *et. al.*[127] calculated Arrhenius prefactors of ~$7x10^{12}$ giving a rate 10^{14} times higher for the *cis-trans* thermal process over that of trans-cis. Thus, a sample left in the dark reverts to near 100% *trans* isomer over time.

A further effect of isomerisation on azo compounds is a change in their absorption spectra between the *trans* and *cis* forms. Due to the greater delocalisation of π electrons in the planar *trans* form there is a reduction in energy over that of the more constricted *cis* isomer, leading to a red shifted absorbance spectrum. This effect is known as photochromism. On excitation the absorption spectrum changes from that of the pure *trans* form to that of a mixture of the *trans* and *cis* forms. At most wavelengths both the *trans* and *cis* isomers will absorb. In solution the *cis* isomer will also thermally isomerise to the *trans* isomer. Isolating the pure *cis* spectrum is, therefore, impossible under normal conditions and so any observed absorbance spectrum is a superposition of the absorbance of both isomers.

Both *cis* and *trans* isomers of azobenzene have three available excited singlet states which can be accessed via excitation in the UV/Vis region of the spectrum. The lowest energy transition, to S_1, an n-π*, transition occurs in the visible region, for the *trans* at 440nm (ε = 500 M^{-1} cm^{-1}) and for *cis* 430 nm (ε = 1500 M^{-1} cm^{-1}). Excitation to the S_2 state, a π-π* transition, occurs in the UV, 314 nm (ε = 17000 M^{-1} cm^{-1}) for *trans* and 280 nm (ε = 5100 M^{-1} cm^{-1}) for *cis*. The third and highest energy transition is restricted to the benzene rings and therefore plays little role in the photochemistry of the molecule. The visible absorption is therefore dominated by the *cis* isomer and the UV by the *trans*. Absorbance of UV light by azobenzene induces a decrease in the high intensity π-π* absorption around 317 nm and an increase in the n-π* transition.

The addition of substituents onto the phenyl rings affects the mobility of electrons within the molecule; this leads to a change in relative positions the energy levels and therefore the absorption spectra. This has been used to create a wide array of dye

molecules absorbing across the UV–VIS spectrum. Substituted azobenzenes fall into two classes, aminoazobenzene and pseudostilbenes.

Aminoazobenzenes are azobenzene molecules which are substituted with electron donating groups, in the *ortho* or *para* positions, on the benzene rings. These groups can conjugate with the azobenzene π orbital system. As the additional electrons are effectively non-bonding, the contribution to the π–system greatly reduces the energy of the π-π* transition over that of azobenzene[75]. This transition is therefore shifted to longer wavelength and gives a high intensity visible absorption. The position of the π-π* band is dependent on the substituent used, with more electron donating substituents providing a greater reduction in energy and therefore larger shift to longer wavelength. In extreme cases the π-π* band is shifted to lower energy than the n-π* band, which is insensitive to the effects of substituent additions. In these cases the photochemical properties will differ from that of the parent azobenzene molecule. The effect of π-conjugation is greatest in the planar *trans* isomer as the non-planar *cis* form disrupts the ability of the electron donating groups to conjugate over the whole molecule. The wavelength shift in the absorbance spectrum will therefore be more pronounced for the *trans* isomer.

Pseudostilbenes are azobenzene molecules that have been 4-donor-4′acceptor substituted, with an electron donor group on one end of the molecule and an acceptor at the other. This creates a "push–pull" molecule with the electron donating and accepting groups in resonance with the azobenzene π system. The result is a further reduction of the π-π* transition energy reducing it in most cases to below the n-π* transition and into the visible region.

A further factor affecting the relative energy levels and, therefore, absorption spectra of azobenzene–based molecules is the solvent in which they are dispersed. As more substituent groups are added to azobenzene forming aminoazobenzenes then Pseudostilbenes, the polarity and electron mobility, or polarisability, of the molecules are increased. The effect of increasing the polarity of the solvent further aids the de-localisation of electrons throughout the molecule, leading to a reduction in energy, which increases the red-shift of the absorption spectrum. Again, as the planar *trans* molecule displays the greater delocalisation of π orbitals than the non-planar, and

therefore less polar *cis* form, the energy of the trans absorption will be reduced furthest. As the TS is also more polar than the *cis* isomer its energy relative to the *cis* isomer is reduced. Efficiency of the thermal isomerisation process is increased due to a reduction in the energy barrier, increasing thermal isomerisation rates. The dyes studied in this thesis fall into the category of pseudostilbene "push-pull" azobenzenes category and, therefore, experience the greatest effect of changing solvent polarity.

2.2.4. Kinetic Modelling

Due to the nature of the photoisomerisation and thermal isomerisation processes, with no other processes present, the modelling of the kinetics of the rates for both are relatively straight forward.

The thermal process from the *cis* to the *trans* state is a simple exponential decay and therefore can be described by the first order rate equation (Equation 2-19)

$$-\frac{d[cis](t)}{dt} = \frac{d[trans](t)}{dt} = k[cis](t) \qquad \text{Equation 2-19}$$

Where [*cis*] and [*trans*] are the *cis* and *trans* isomer concentrations at time t and k is the thermal rate constant. Applying the Beer–Lambert law discussed above, the rate of the thermal isomerisation can, therefore, analytically be found by using Equation 2-20.

$$A(t) = [A(0) - A(\infty)]\exp(-kt) + A(\infty) \qquad \text{Equation 2-20}$$

For calculation of the photoisomerisation rate an analytical solution such as Equation 2-20 is unsatisfactory due to the number of variables and the conditions under which the experiments are performed, as described in the experimental section for the photochemical measurements. Therefore, a complete numerical solution was found by solving the rate equations involved in the three processes, photoisomerisation from *trans* to *cis* and *cis* to *trans* and the thermal isomerisation from *cis* to *trans*. Because of the exceptionally long path-length over which the measurements are performed in PCF in comparison to a conventional cuvette there is significant reduction in excitation intensity throughout the length of the fibre, due to the

waveguide losses along with sample absorption. However, the precisely defined excitation conditions make measurement of the irradiation intensity straightforward, without the use of actinometry, which is necessary in cuvette-based experiments. The model takes account of the fall-off in excitation intensity along the length of the fibre by integrating through both time and space. The rate equations solved along with the continuity equation are given below, where n_T, n_C, n_{TS} are the number of molecules in the *trans*, *cis* and *transition* states respectively. The parameters correspond to the processes shown in Figure 2.25.

$$\frac{\partial n_T}{\partial t} = -\frac{I_p}{h\nu_p}\sigma_T n_T(t) + \Gamma_{TS-T} n_{TS}(t) + \gamma_{C-T} n_C(t) \qquad \text{Equation 2-21}$$

$$\frac{\partial n_C}{\partial t} = -\frac{I_p}{h\nu_p}\sigma_C n_C(t) + \Gamma_{TS-C} n_{TS}(t) - \gamma_{C-T} n_C(t) \qquad \text{Equation 2-22}$$

$$\frac{\partial n_E}{\partial t} = \frac{I_p}{h\nu_p}\left(\sigma_T n_T(t) + \sigma_C n_C(t)\right) - n_{TS}(t)(\Gamma_{TS-T} + \Gamma_{TS-C}) \qquad \text{Equation 2-23}$$

$$Continuity, \qquad n_{Total} = n_T + n_C + n_{TS} \qquad \text{Equation 2-24}$$

The rate of irradiation intensity reduction through the fibre is the combination of absorbance, given by the Beer Lambert law, and fibre loss given by

$$I_p(z) = I_0 10^{-\int_0^z \alpha(\xi) d\xi} \qquad \text{Equation 2-25}$$

where I_p is the intensity at point z along the fibre and $\alpha(\xi)$ is the combined position-dependent attenuation due to fibre loss and molecular absorption

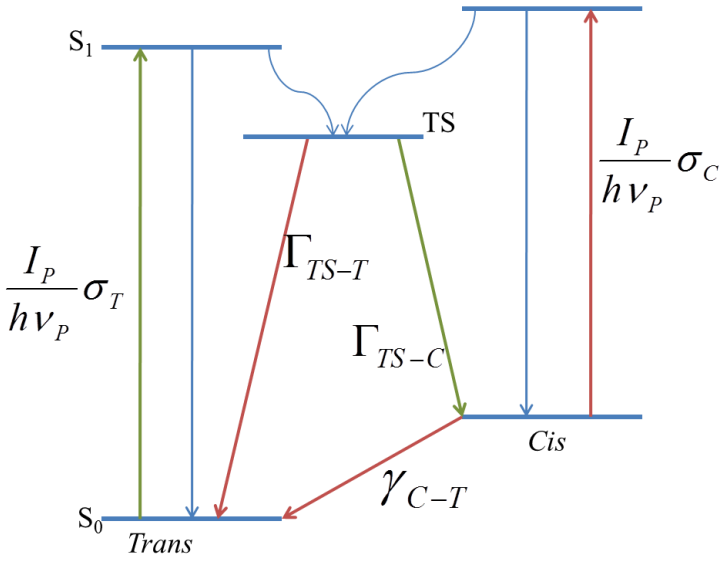

Figure 2.25: Energy level diagram for the photoisomerisation of "push–pull" azobenzene derivatives showing the processes and associated parameters used in the numerical model. Excitation of *trans* and *cis* isomers populates a common transition state (TS).

To apply these equations the extinction coefficients of both *trans* and *cis* isomers need to be known. For the *trans* isomer this is straight forward as a measurement on a sample that has been left in the dark is 100% *trans*, however, to gain knowledge of the *cis*–isomer coefficient, study of the PSS is required. This can be found from the composition of the PSS given by Equation 2-26.

$$\%cis_{PSS} = \frac{[trans]_0 - [trans]_{PSS}}{[trans]_0} \times 100 \qquad \text{Equation 2-26}$$

For most azobenzene derivatives, including those used in this study, there is a wavelength where the absorbance of the *cis* isomer is negligible compared to the *trans* isomer, usually at the peak of the *trans* absorbance, and so measuring the ratio of the peak absorbance between a sample in the dark and at the PSS yields the ratio of [*trans*] for calculation of the %*cis* at the PSS. As the *trans* extinction coefficient, ε_{trans}, can be found for the whole spectrum from a dark sample the *cis* extinction coefficient, ε_{cis}, is therefore

$$\varepsilon_{cis} = \frac{\varepsilon_{PSS} - (1-\chi)\varepsilon_{trans}}{\chi} \qquad \text{Equation 2-27}$$

Where χ is the fraction of *cis* isomer.

From the ratio of photoisomerisation rates and the thermal isomerisation rate, the overall quantum yield of the process can then be calculated. The kinetic modelling is discussed in more detail in chapter 4

2.3. Fluorescence Spectroscopy

Fluorescence spectroscopy is one of the most sensitive analytical techniques available for the study of molecules. One of the earliest observations of fluorescence was made by Nicolás Monardes, who, in 1565 reported the peculiar blue colour of a wood infusion in Mexico. This was then used to detect counter–fitted wood which would not fluorescence[76]. The term fluorescence was properly defined by the physicist Stokes in 1853 after several experiments using invisible ultraviolet light to irradiate a tube of quinine, causing it to emit visible blue light[77].

The principle of fluorescence has been used extensively across all of the physical sciences, for high resolution imaging for microscopy and detection of molecular interactions, reaching the ultimate limit of sensitivity, single molecule detection. In biology fluorophores offered a non-toxic method of tracking and analysing biological samples, and with the use of multiple fluorophores emitting at different wavelengths large structures can be examined with unprecedented detail. The study of fluorescence has led to the development of many analytical techniques such as fluorescence activated cell sorting (FACS) [78], automated DNA sequencing, fluorescence lifetime imaging (FLIM) and Förster resonance energy transfer (FRET)[79], a technique that can be used as a molecular ruler. The principles of fluorescence using single and multi-photon excitation will be discussed here along with the technique of fluorescence lifetime measurements.

2.3.1. Molecular Fluorescence Spectroscopy

The basic processes that a molecule can undergo after excitation by a photon of light are shown in Figure 2.26.

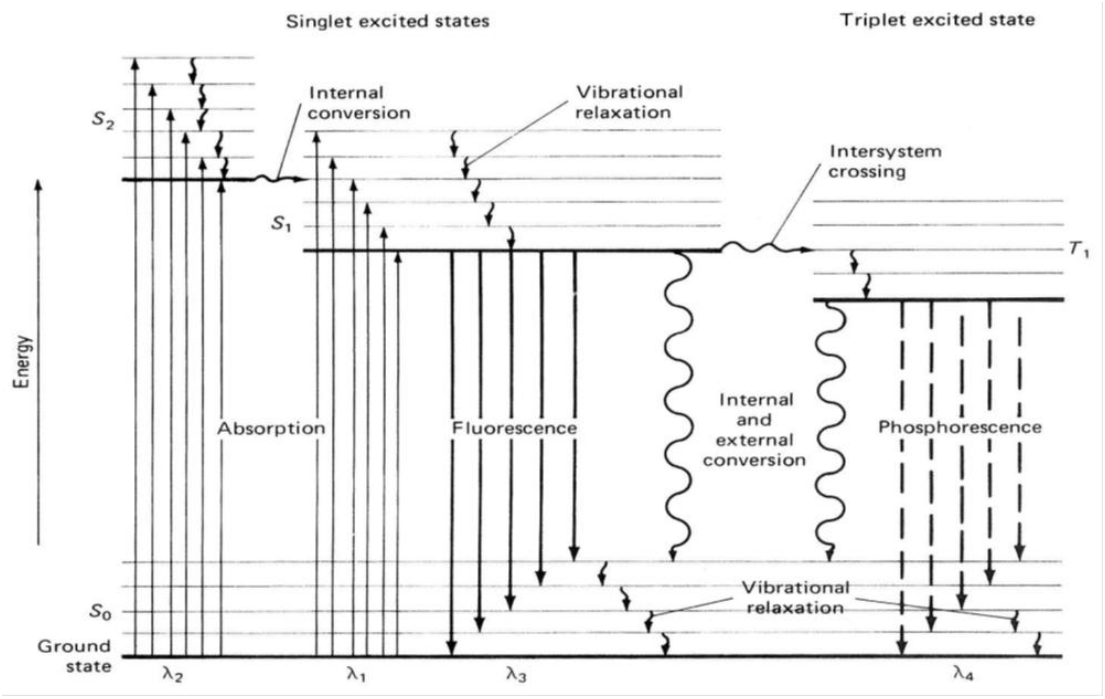

Figure 2.26: Schematic of the radiative and non-radiative processes undergone by a molecule after excitation by a photon of light[80].

Following excitation to an excited electronic state, say S_2, the molecule will usually be vibrationally excited within this state. The first process that occurs after electronic excitation will be vibrational relaxation to the vibrational ground state of the electronic excited state, this process occurs very fast, on the picosecond timescale[66] mainly through collisions with other molecules. This is a significantly shorter time period than the average lifetime of an electronic excited state and therefore all following processes typically occur from vibrationally relaxed electronic states. Following vibrational relaxation the molecule can relax to the first excited state S_1 through internal conversion (IC), an intramolecular non-radiative process in which the spin state stays the same, on the femtosecond timescale[64]. IC involves direct coupling between the two vibronic energy states, or if the energy gap is very small through quantum tunnelling. Following this relaxation to the S_1 state there are several routes back to the ground state S_0, which will now be discussed.

2.3.1.1. Fluorescence

Decay from the S_1 to S_0 states can be observed via fluorescence. In this process the excess energy of the electron in the excited state is lost through the emission of a photon. The energy of this photon will be equivalent to the difference in energy between the excited state and the ground state to which it decays. As this ground state may be a vibrationally excited, photons of more than one energy, or frequency, are released. Because absorption is usually from the ground state vibrational level of S_0 to a vibrationally excited energy level and the decay is from the ground state vibration of the excited state to a vibrationally excited ground state the emission spectrum of a fluorophore is often a mirror image of its absorption spectrum.

With emission of fluorescence, in general, always occurring from the same excited state, with the same competing processes, regardless of excitation wavelength, the emission spectrum of a fluorophore is in general independent of excitation wavelength. The emission intensity of the molecule, therefore, simply depends on the efficiency of absorption at a specific wavelength, given by its absorbance spectrum.

As a portion of an absorbed photon's energy is usually lost non-radiatively through decay to the vibrationally relaxed S_1 state, the energy of the emitted photon is always less than or equal to the excitation energy. This general reduction in photon energy between excitation and emission produces a red shift between the absorption spectrum of a fluorophore and its emission spectrum. This shift in emission to longer wavelength than the initial excitation is known as the Stokes shift. The size of the Stokes shift is fluorophore dependent and a large Stokes shift is often favourable, due to the phenomenon of reabsorption. Reabsorption can occur when a fluorophores emission spectrum overlaps with its absorption spectrum as shown in Figure 2.27.

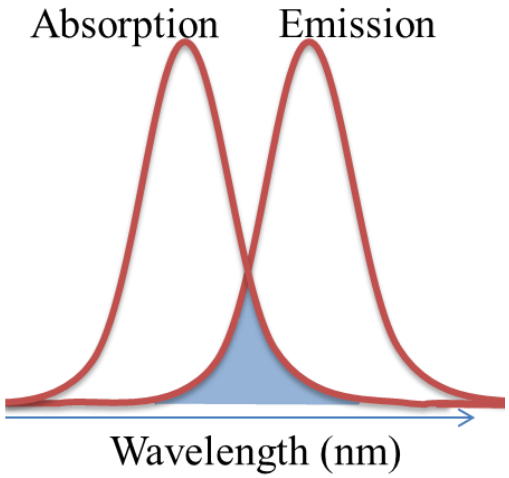

Figure 2.27: Overlap of a fluorophores absorption and emission spectra. Photons emitted in the shaded area, where the two overlap, can be reabsorbed by another molecule.

When an emitted photon has an energy falling within the absorption spectrum of the fluorophore it can be reabsorbed by a second molecule within the sample. Whilst this can lead to a further fluorescence emission, the energy can also be lost via a non-radiative pathway, reducing the overall fluorescence intensity observed. A second effect often observed in concentrated samples, using fluorophores with a small Stokes shift, is a red-shift in the peak of the emission spectrum. This occurs as the lower wavelengths of the emission spectrum are subject to strong reabsorption.

2.3.1.2. Internal Conversion

IC can lead to direct non-radiative transition from the S_1 to S_0 states. The timescale of IC is typically on the scale μs to ps. As the decay does not involve an emission of a photon it is not directly observed and acts to reduce the fluorescence quantum yield.

2.3.1.3. Intersystem Crossing

Intersystem crossing (ISC) is a further, non-radiative, intra-molecular process between electronic states that have differing spin multiplicities, for example from a singlet to a triplet state[81]. For this to occur the total spin of the electronic state must

invert and therefore this is a forbidden transition. ISC can occur through spin-orbit coupling where there is interaction between the electron spin and its molecular orbit which mixes the singlet and triplet states it occupies. The electron can, therefore, change its spin and decay through a change in multiplicity. Following this decay to say the T_1 triplet state further decay to the ground state S_0 can occur through a second ISC process that is non-radiative, or through the loss of energy as emission of a photon known as phosphorescence. Because the electron has already lost energy due to ISC to the triplet state, phosphorescence will occur at longer wavelengths than fluorescence.

2.3.1.4. Molecular Quenching

Molecular quenching is an intermolecular interaction where the energy from an excited molecule is transferred to a second molecule known as the quencher through processes such as molecular collision or electron transfer giving

$$M^* + Q = M + Q^* \qquad \text{Equation 2-28}$$

where M is the initially excited molecule and Q is the quencher molecule. Many molecules can act as quenchers such as oxygen and halogens or even another excited dye molecule through triplet quenching given by

$$T^* + T^* \rightarrow T^* + S \quad / \quad T^* + T^* \rightarrow S^* + S \qquad \text{Equation 2-29}$$

where T^* is the triplet state of the fluorophore and S is the ground state.

The mechanism of the energy transfer can vary from electron transfer to spin-orbit coupling and intersystem coupling to a triplet state. Quenching does not change the structure of the fluorophore in the way that photochemical bleaching does, discussed in section 2.3.1.6, allowing the molecule to undergo further excitation cycles.

2.3.1.5. Resonance Energy Transfer

A further intermolecular process that deactivates excited fluorophores is resonant energy transfer (RET) which occurs when the emission spectrum of the fluorophore, the donor, overlaps with the absorption spectrum of another molecule, the acceptor, such as shown in Figure 2.28.

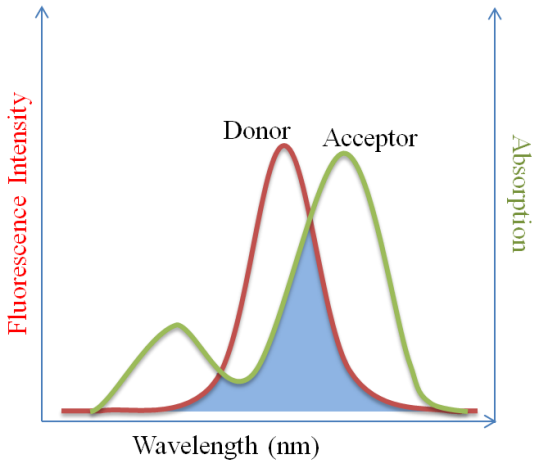

Figure 2.28: Overlap (shaded area) of the emission spectrum of a donor fluorophore and absorption spectra of a RET acceptor.

The process of RET does not involve an intermediate photon, i.e., it is not a re-absorption event, the donor and acceptor molecules exchange energy through a dipole–dipole interaction when in sufficiently close proximity. The efficiency of this energy transfer is determined by the extent of the spectral overlap. By convention the distance over which this process occurs, between donor and acceptor (r), is described using the Förster distance (R_0). The distance dependence of the rate constant for this energy transfer is given by,

$$k_T(r) = \frac{1}{\tau_D}\left(\frac{R_0}{r}\right)^6 \qquad \text{Equation 2-30}$$

where τ_D is the lifetime of the donor excited state in the absence of energy transfer[64].

The distance dependence of the rate constant is therefore given by

$$E = \frac{R_0^6}{R_0^6 + r^6} \qquad \text{Equation 2-31}$$

For most donor–acceptor pairs Förster distances are on the order of 10s of angstroms and so RET can be used as a form of "molecular ruler". When the acceptor is itself a fluorophore it can emit fluorescence after energy transfer from the donor. This will generally be at a longer wavelength than the donor fluorescence as energy is lost during the transfer.

2.3.1.6. Photochemical Bleaching

Photobleaching is the process through which the absorption of excitation light causes irreversible structural change to the fluorophore[82]. The robustness of a fluorophore to photobleaching is determined by the number of absorption-emission cycles it can undergo before permanent damage is induced, this may be through interaction of the excited states and other molecules causing chemical reaction to occur producing a new, non-fluorescent molecule, or through loss of functional groups. For example, at an excitation rate of 10^5 photons s^{-1}, a typical organic dye can withstand 10^4–10^5 excitations before it will bleach, or 0.1–1 s of excitation. Work to improve dye stability led to the development of quantum dots which can exhibit robustness of over 10^8 cycles due to dye confinement preventing interaction with other molecules and radicals, allowing them to last >1000 s under high intensity excitation.

Due to the rate at which intermolecular processes occur photochemical bleaching usually occurs via the longer lived (µs – ms) triplet excited state as the S_1 state is usually too short lived (1–10 ns) for much interaction to occur with other molecules. From the excited triplet state several processes can occur to permanently affect the dye such as electron transfer between dye molecules or chemical quenching where the dye molecule loses an electron to the quencher such as O_2.

2.3.2. Two Photon Excitation of Fluorescence

In two-photon fluorescence spectroscopy the fluorophore is excited by two photons simultaneously, with each photon carrying half the energy required for the equivalent one photon excitation (OPE). The process is presented schematically in Figure 2.29.

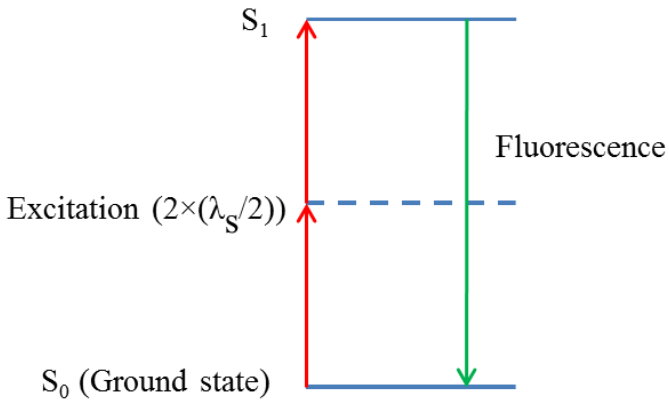

Figure 2.29: Schematic of two photon excitation of a fluorophore.

Because of the requirement of two photons reaching the molecule at exactly the same time, in the right conditions for an absorption event to occur, the efficiency of the process is non-linear and scales as intensity squared. The absorbance cross-section for two-photon excitation (TPE) is usually extremely small, requiring very high power densities to achieve a detectable level of fluorescence events. For example the Fluorescein fluorophore used this work has a single photon absorbance cross section at 450 nm of 5.3×10^{-18} cm^2 $molecule^{-1}$ whereas at 820 nm it has a two photon absorbance cross section of 5.4×10^{-49} cm^4 s $molecule^{-1}$, 31 orders of magnitude smaller[83]. In conventional experiments two–photon excitation of a fluorophore in bulk solution is achieved by focusing a high powered light source, normally an ultrafast pulsed Ti-Sapphire laser, into the sample through a high magnification objective. This produces spot of very high intensity at the focal point of the objective where the power density of each pulse is sufficient to cause excitation. The problem with this approach is the path length over which the intensity is at the required level is very short, exciting only a few pico litres of sample within a larger volume of solution[84]. Using a standard 1 mL micro-cuvette this equates to an excitation volume of $\sim10^{-5}$% of the overall sample. Collection of the excited fluorescence is therefore difficult due to the very low intensity of the emitted

fluorescence. Further, diffusional motion in the bulk sample means that the molecules in the small probed sample volume are constantly changing.

The relaxation processes following TPE excitation are identical to those following OPE. The fluorescence spectrum is therefore the same and there are all of the same competing processes providing non-radiative decay pathways from the excited state, reducing the number of fluorescence events.

Whilst the need for focusing the laser beam is limiting in terms of measuring the effect of TPE in bulk solution in a comparative way to single photon excitation TPE has advantages in other areas. As excitation only occurs at the focal point of the objective, which can be deep within a sample, fluorescence can be detected from specific points allowing three dimensional images of fluorophore location to be produced. This technique is known as fluorescence imaging, and has been used extensively throughout the physical sciences in areas such as imaging the complex structures of biological samples[78]. TPE also finds application in many rapidly developing areas in photochemistry such as the excitation of drugs used in photodynamic therapy (PDT)[85]. In this case the ability to use long wavelength lasers which can penetrate deep into tissue along with the very specific excitation location make TPE far more beneficial than OPE. It is therefore of great interest to develop systems in which TPE is able to be performed in controlled environments to aid further development in areas such as PDT.

2.3.3. Fluorescence Lifetime Spectroscopy

Another very important feature of the fluorescence emitted from a fluorophore, which provides a very useful measurable parameter, is its lifetime. The fluorescence lifetime of a fluorophore is defined as the average lifetime of the excited state from which the fluorescence decay occurs. This lifetime, τ, typically on the timescale of 10's of ns, is dependent on the sum of all of the rate constants of the decay processes, both radiative, Γ, and non-radiative, $k_{nr,}$ given by

$$\tau = \frac{1}{\Gamma + k_{nr}} \qquad \text{Equation 2-32}$$

As all of the decay processes are by definition random, for a single exponential decay 63% of the molecules will decay before time, $t = \tau$, and 37% after.

The fluorescence lifetime of a molecule is usually measured using a system employing time correlated (TC) single photon detection, using a single photon avalanche diode detector (SPAD). A SPAD detector operates through the principle of a highly biased p-n semiconductor junction[86]. The absorbance of a photon causes an electron "avalanche" on the sub nano-second timescale causing a sharp rise in current. The leading edge of this rise marks the arrival of the photon and can be detected on the picosecond timescale. When used in conjunction with a pulsed light source the time between emissions of a pulse from the source to the detection at the SPAD can be accurately correlated leading to a TCSPAD system. In the case of a fluorescence measurement the emission of a pulse from the excitation source is transmitted to the detection system, which counts the time between that signal and the signal from a photon arriving at the SPAD detector. From the distribution of arrival times of the fluorescence, the lifetime of the excited state can be calculated. A schematic of such a setup is shown in Figure 2.30.

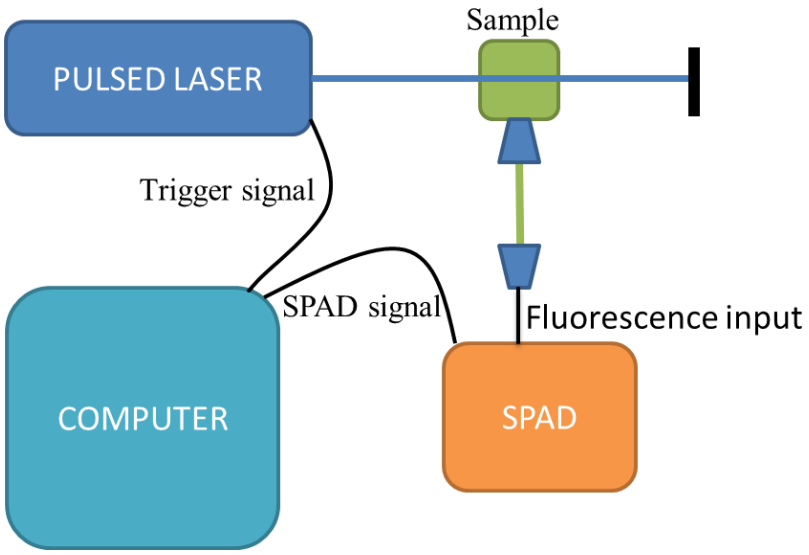

Figure 2.30: Simplified schematic of a typical fluorescence lifetime measurement setup. A pulsed laser sends a repeated trigger signal to the measurement device (controlled by computer) to "start the clock" and the time for the fluorescence from a sample emitted following excitation to reach the SPAD is found by waiting for the SPAD signal.

2.3.4. Photo-physics of Fluorescein

The principal fluorophore used in the present work is the Fluorescein molecule. Fluorescein was chosen due to its high quantum yield, with a single photon absorption cross section of 5.3×10^{-18} cm^2 $molecule^{-1}$ at 470 nm excitation[87], and the fact it is very widely used as the basis for a wide range of molecular labels and fluorophore derivatives. The two–photon absorption of the molecule has also been widely studied as it exhibits a large two–photon cross–section of 5.4×10^{-49} cm^4 s $molecule^{-1}$ [82] making it ideal for these studies and as such will allow semi-direct comparison of OPE and TPE in PCF in this study.

The Fluorescein molecule exists in different forms depending on pH, giving different spectral characteristics as the delocalisation π of electrons and hence the relative energies of the ground and excited states varies. Sjöback *et al.*[88] studied the molecular composition of a solution of Fluorescein as pH was varied from 2 – 8. The molar ratios of the cation, neutral forms, anion and dianion found are shown in Figure 2.31. The aqueous solutions in the present work were used at ~pH 7 and therefore the dominant form will be that of the dianion, with an influence from the presence of ~25% anion form. The different electronic arrangement will affect both the absorption and emission spectra of the dye and, therefore, the emission is excitation wavelength dependent when more than one form is present in solution. The absorption and emission at pH 5.56 and 6.53 for a range of excitation wavelengths, along with the extracted absorption and emission spectra of the anion and dianion forms, are shown in Figure 2.32 . The excitation wavelength used in the present study is 470 m, and therefore there will be excitation of both anion and dianion forms. The structures that Fluorescein takes with increasing pH are shown in Figure 2.33, from the cation form through three neutral, two anion and the dianion forms. Of the three neutral species the quiniod (left most in Figure 2.33) is the most prevalent and is red in colour. For the anion species where the negative charge can reside on the carboxylate group or a ring hydroxyl, the carboxylate form is usually more dominant due to the acidic nature of the group.

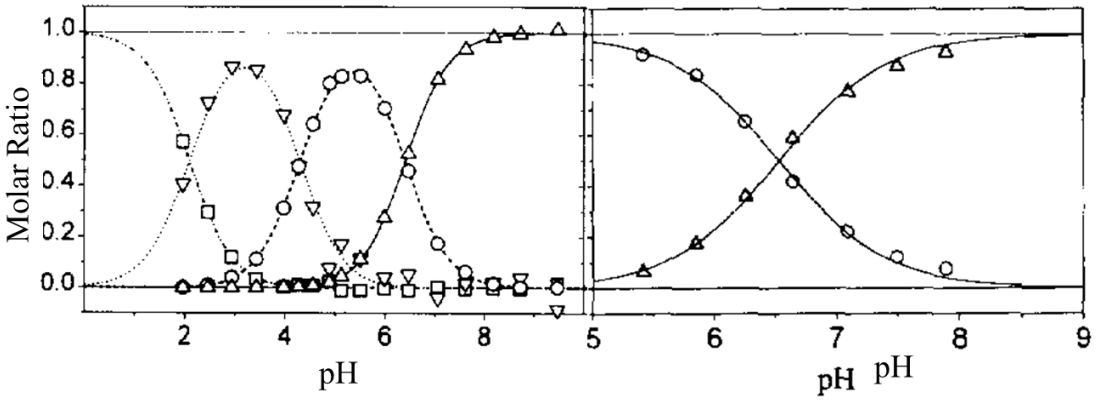

Figure 2.31: (left) Composition of a Fluorescein solution at varying pH showing the relative concentration of cation (□), neutral OPEcies (▽), anion (o) and dianion (△). (right) Composition at pH 5-9[88].

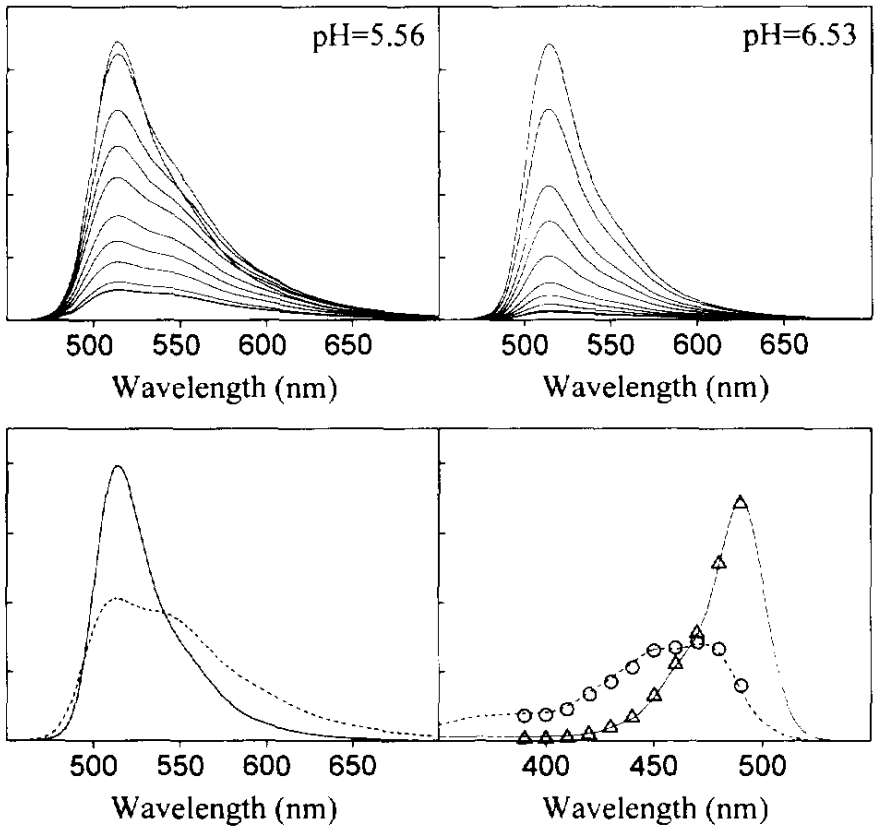

Figure 2.32: Top; Emission spectra of Fluorescein buffered at pH 5.56 (left) and 6.53 (right) excited at 390, 400, 410, 420, 430, 440, 450, 460, 470, 580, and 490 nm, the highest intensity peak corresponding to 490nm excitation. Bottom: Emission (left) and excitation (right) spectra of the anion (---) and dianion (——) forms of Fluorescein. (◦) and (△) represent experimental data for the anion and dianion respectivly[88].

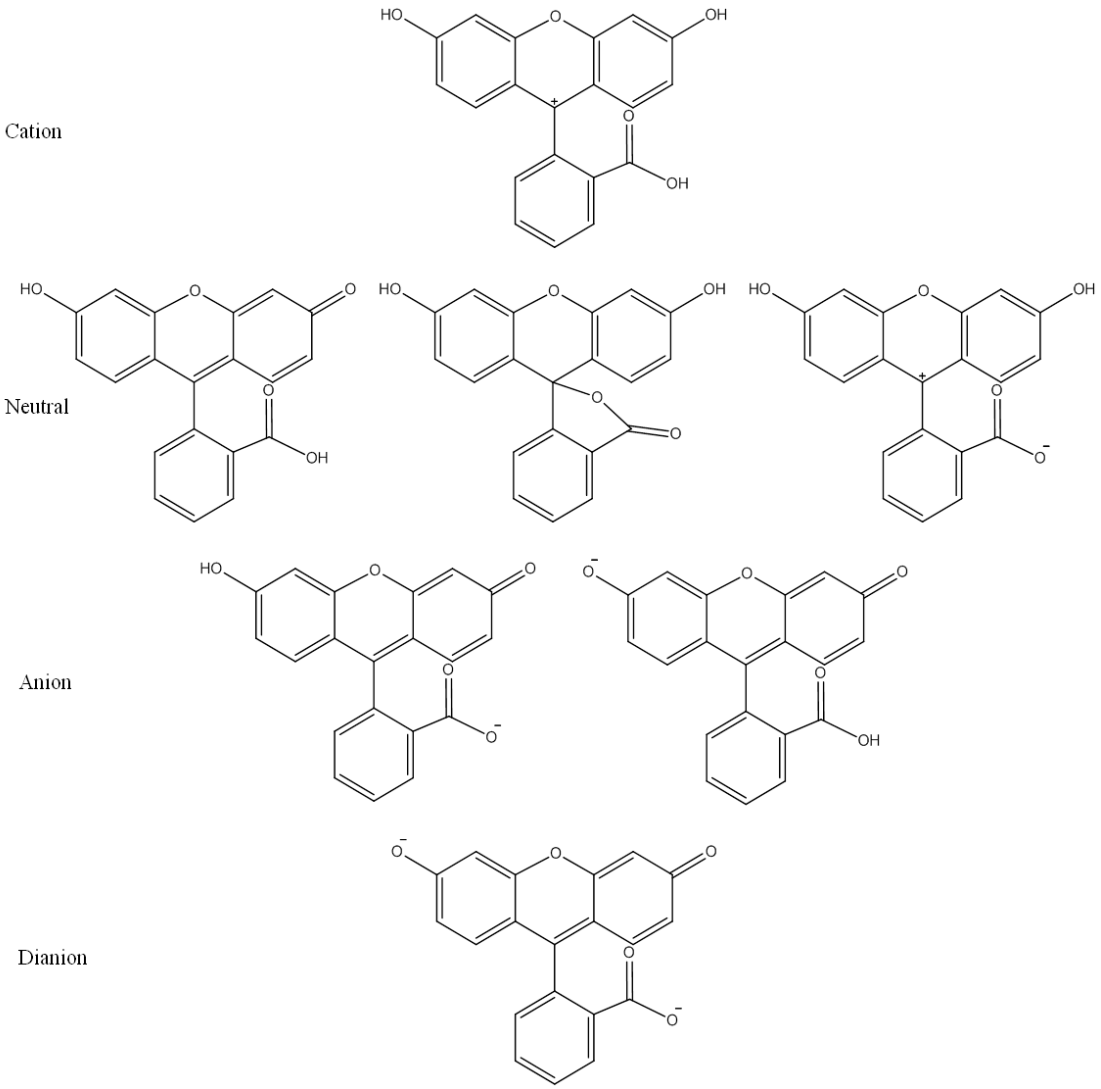

Figure 2.33: Various forms of Fluorescein formed by increasing pH of the solution from ~pH 2 for the cation, 2–4 for neural species, 4–7 for the anion and >7 for the dianion[88].

The dianion form of Fluorescein which is the dominant form in the presented work has the highest fluorescent quantum yield of 0.93 with the anion form having a much lower quantum yield of 0.37. The stokes shift of the fluorophore is around 30 nm for the dianion form which has an absorbance maximum around 485 nm and emission maximum around 515 nm. This small Stokes shift means that reabsorption as discussed in section 2.3.1.1 has a major influence in more concentrated samples, red-shifting the observed emission maximum to around 520 nm.

2.3.5. Photo-physics of Rhodamine B

Like Fluorescein, Rhodamine B exhibits different molecular forms with varying pH, mainly due to the carboxylic functional group. The structure of the molecule in its cation (low pH) and zwitterionic (neutral to high pH) forms are shown in **Figure 2.34**[89]

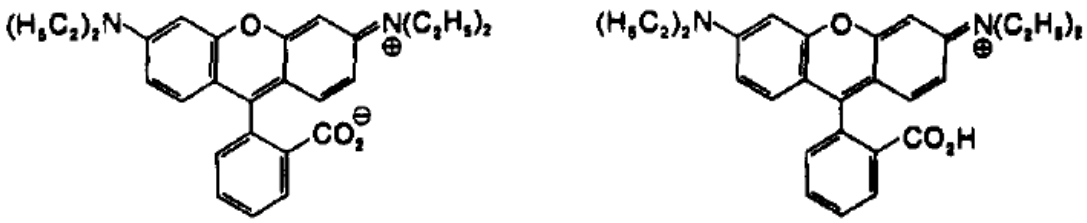

Figure 2.34: Zwitterterionic (left) and cationic (right) forms of Rhodamine B.

The rate of non-radiative decay of Rhodamine B fluorophore is influenced by the ability of the alkylamino groups on the molecule to rotate[88,90]. The effect of rotation of these groups from the planar to the twisted form is a shift in the $S_1 - S_0$ energy separation leading to different relative rates of non-radiative internal conversion and fluorescence. It has been shown by several studies that as the temperature is decreased the quantum yield of the fluorophore is found to approach unity[91,92,92], indicating that the molecule can exist in an emissive planar form or non-emissive twisted form where energy is lost via the IC pathway. Restriction in the internal rotation of the functional alkylamino groups favours the radiative planar form leading to higher quantum yield. This principle is summarised in Figure 2.35 showing the two excited states and related decays. As the fluorescence lifetime of the molecule is a sum of all of the radiative and non-radiative processes, the increase in non-radiative decay will be apparent as a decrease in the observed lifetime for fluorescence. This allows the molecule to be used as a temperature probe based on the measured lifetime after a calibration curve has been produced. Such a curve found by D. Mendels *et al.*[93] is shown in Figure 2.36.

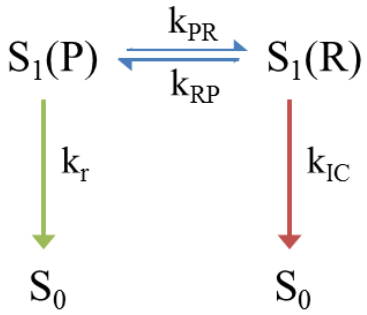

Figure 2.35: Simplified schematic of the singlet energy levels in Rhodamine B representing the excited planar form $S_1(P)$ and twisted/rotated form $S_1(R)$ with k_r the radiative rate constant from the planar form, k_{IC} the IC rate constant from the twisted form and $k_{PR/RP}$ the rates of inter-conversion from the planar to twisted forms.

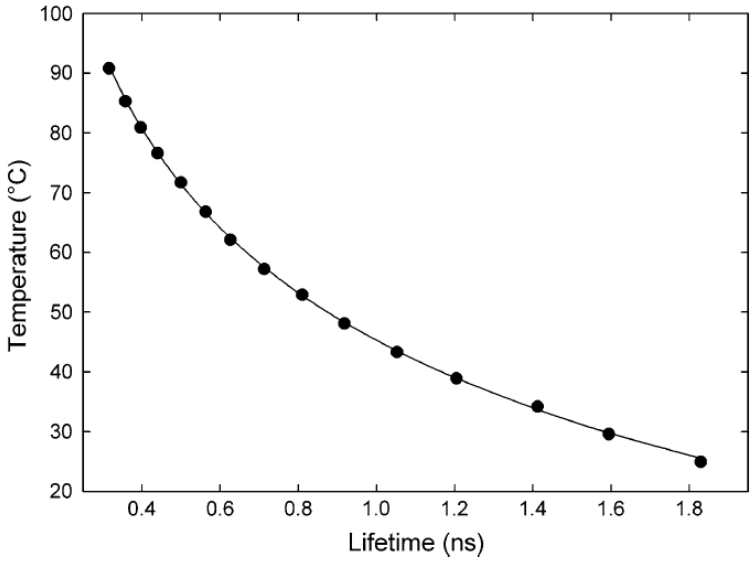

Figure 2.36: Calibration curve for the fluorescence lifetime of the Rhodamine B fluorophore ($\boldsymbol{\tau_f}$) as a function of solution temperature, fitted by the Arrhenius equation to give E_a = 24.19 kJmol^{-1} and τ_0 = 9.283 ns[93].

Another consequence of this torsional influence is that immobilisation of the molecule on a surface restricts the molecules ability to rotate, increasing the observed lifetime. This was studied by T. A. Smith *et al.*[94] by immobilising the fluorophore using colloidal silica, allowing the lifetime of the free and immobilised molecule to be extracted. A value of 3.65 ns was found for the lifetime of Rhodamine B on a silica surface. The difference in the lifetime between the solution-phase and surface-attached fluorophore provides a useful tool for determining the fluorophore environment.

3. Photochemistry in Photonic Crystal Fibres

3.1. Introduction

The application of photochemistry is seeing growth in many areas, including photo-medicine[95], artificial photosynthesis[96,97], optically switchable media for data storage and the control of molecular machines[60], stimulating the synthesis and characterisation of novel photoactive compounds. There is also a drive for the miniaturisation and integration of sample preparation and monitoring systems into lab-on-a-chip devices. Such an approach is applicable to photochemical reactions by utilising optofluidic systems, in which optical excitation and detection systems are integrated with microfluidics[98].

UV–visible (UV–vis) absorption spectroscopy is a convenient and commonly used method for monitoring the progress of photochemical reactions in conventional cuvette-based measurements, but is relatively insensitive because of the short path-lengths that are typically used. As discussed in section 2.2.2, in the case of a UV–Vis absorption measurement the sensitivity is completely governed by the path–length over which the measurement can be made as described by the Beer–Lambert law. Increasing the path-length is often impractical because of the constraints of commercial spectrometers or the limited availability of sample. The use of glass capillaries reduces the sample volume required but such simple capillaries have very high optical losses and are highly sensitive to bending, greatly limiting the possible length that can be used[48].

A further desirable feature of a spectroscopy system for the study of photochemical reactions is uniform exposure of the sample to both the pump and probe light source. Also, as some reactions require high pump intensities it is advantageous to make the cross sectional area of the incident beam as small as possible to reduce the power requirements, whilst providing the greatest possible sample overlap. Therefore, the ideal sample cell for the spectroscopic study of photochemical reactions is an optofluidic device that combines a long path–length with a small cross-sectional area, in which the entire (small) sample volume is exposed to both the photochemical excitation (pump) beam and the spectroscopic probe beam. These requirements are

hard to achieve in conventional lab on a chip designs[99,100,101].

Integration of lasers and micro-cuvette on a chip has been achieved[102] and allows for small volumes; however, as the sample is not contained within a waveguide the distance over which it could be excited is very limited to ~1 mm. Other systems have used liquid–core waveguides with guidance through metal jackets[103]. These designs experience high loss due to surface imperfections as discussed in section 2.3, reducing guidance and limiting the path length that can be used.

Progress in implementing long path-length absorption spectroscopy in an optofluidic system has been made through the use of PCF. As discussed in section 2, in a PCF, light is trapped inside the fibre core by a periodic lattice of microscopic holes in the cladding glass, a "photonic crystal", which create the guidance mechanism. Initial studies were performed using solid-core PCF (SC-PCF). In such a fibre the sample is infiltrated into the cladding crystal structure and probed by the evanescent field of the guided light[104,105]. For example Cordeiro *et al.*[106] show enhanced absorbance sensitivity for the Methylene Blue dye using a micro-structured fibre core, whilst Euser *et al.*[107] demonstrated the use of a suspended core fibre for absorption sensing of aqueous $NiCl_2$ with a sensitivity two orders of magnitude greater than in conventional UV–Vis systems. Whilst SC-PCFs are effective in achieving detection over long path-lengths, there is limited overlap between the guided light and the sample, providing a less-than-ideal probe regime. Furthermore, the probed sample is in very close proximity to the silica fibre surface, where its properties may differ from those in the bulk solution. These disadvantages are overcome by the use of hollow-core PCF (HC–PCF), in which light is guided through the sample solution in the hollow core of the fibre.

The structure of a HC–PCF such as the kagomé fibre used in this study (Figure 3.1(C and D)) allows for the guidance of light, in a single well-defined mode, over long path lengths. When the fibre microstructure is filled with a sample solution there is near perfect light-–sample overlap within the fibre core[108]. The relative dimensions of the core of the kagomé HC–PCF compared to a standard 1cm cuvette are shown in Figure 3.1 (A and B). Irradiation across the full width of the cuvette, over a path length of 1 cm, requires a minimum sample volume of 1 mL, whereas the 19 μm core

of the HC–PCF holds only 2.8 nL cm^{-1}. This means that the relatively long path length of 30 cm used in this study only requires ~90 nL of sample. Both excitation and broadband measurement sources are co-coupled into the fibre core, giving perfect overlap of both with the sample (Figure 3.1 (D)). This greatly reduces influences such as convection, a further hindrance in traditional cuvette measurements. Furthermore, precise knowledge of the excitation intensity and probed volume facilitates quantitative modelling of the kinetics of a photochemical reaction taking place within the fibre.

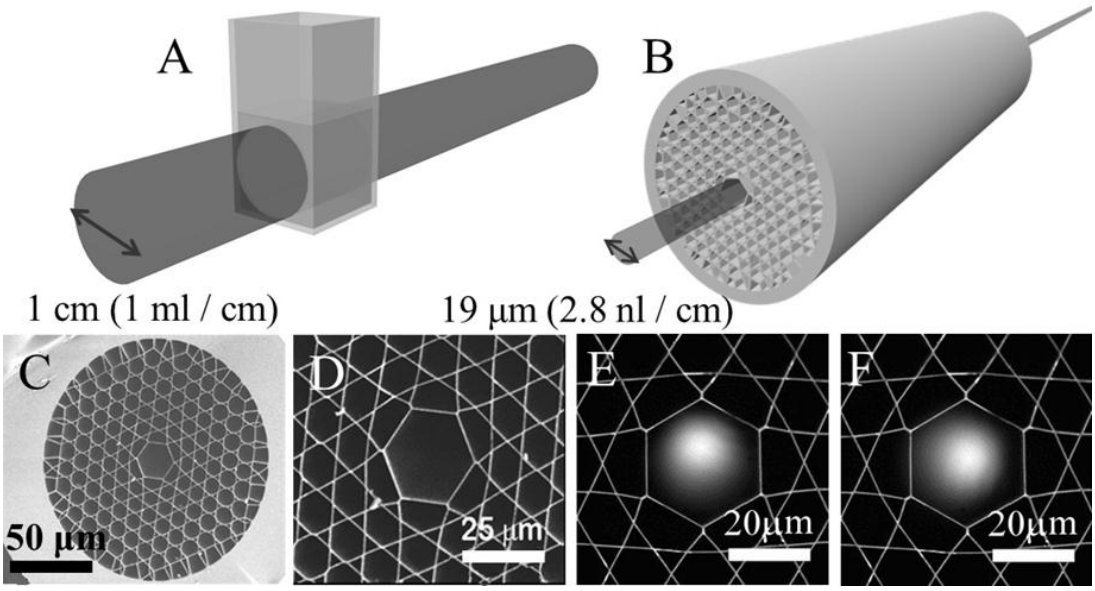

Figure 3.1: Schematic comparison the geometries and sample volumes in a conventional cuvette (A) and a HC–PCF (B). High-resolution scanning electron micrographs of a kagomé HC–PCF with a core diameter of 19 µm (C-D). Transverse irradiance profile measured using the 488 nm laser (E) and the broadband xenon lamp (F).

Previous work by MPL as part of the Kroeber project has been carried out, demonstrating the use of HC–PCF as a photochemical reactor to monitor the photolysis of vitamin B12, cyanocobalamin[109]. This is an irreversible reaction with very low quantum yield (~10^{-4}). The measurement was conducted under similar experimental conditions to those presented here. The work highlighted the strong confinement of both sample and light in the hollow core resulting in a 1000-fold increase in reaction rate over that in a conventional cuvette whilst using a low excitation power of 10 µW.

This thesis presents an extension of this approach to the measurement of the kinetics of thermally reversible photochemical reactions with relatively high quantum yield, namely the photoisomerisation of azo dyes. The spectroscopic monitoring of such reactions poses challenges that were not encountered in the previous study. The thermal reversibility demands that the spectroscopic measurement made as soon as possible after photoisomerisation is induced. For any period where the excitation light is off, the reverse thermal process counter–acts the increase in *cis* isomer produced, leading to a reduction in the measured photo-product. Also the high quantum yield requires the use of a low probe intensity to avoid probe-induced photochemistry in the fibre core.

The measurement of a reversible photoisomerisation process in PCF has been shown by A. Khetani *et al.*[110] who demonstrated the photo-generation and detection of a transient species within a HC–PCF, using laser flash photolysis. However, they used a perpendicular arrangement of pump and probe beams, such that the sample solution was excited perpendicular to the fibre core, through the cladding, and monitored by probe light guided through the core. Thus, the path-length for the pump beam was extremely short, only a few microns (the diameter of the fibre core), requiring the use of a concentrated (mM) sample solution, and the effective probe path length was only ~1 cm. This study, therefore, failed to exploit the large gain in sensitivity offered by coaxial guiding of both pump and probe beams through the hollow core. Also, the cladding holes of the fibre used were collapsed, affecting the guidance mechanism of the fibre. As discussed in chapter 2.1.3.2, when the cladding holes are collapsed, the core of the fibre has a higher effective refractive index than the cladding and guides by the mechanism of total internal reflection. The relatively large diameter of the core means that a high number of modes are supported and single-mode guidance is very hard to achieve.

The present work demonstrates the use of HC–PCF as a reaction chamber for monitoring a reversible photochemical process through the quasi-real time tracking of the photo-isomerisation of two azobenzene based dyes, Disperse Red 1 (*N*-ethyl-*N*-(2-hydroxyethyl)-4-(4-nitrophenylazo)aniline)[66,111,112,113,114]and Disperse Orange 1 (4-Anilino-4'-nitroazobenzene)[115,116,117]. The structures of the dyes along with the isomerisation process are depicted in Figure 3.2. The feature of interest in this study

is the ability of these molecules to undergo isomerisation between two isomeric forms under UV–Vis irradiation. This readily induced photo-isomerisation is rapid, reversible and of high quantum yield.

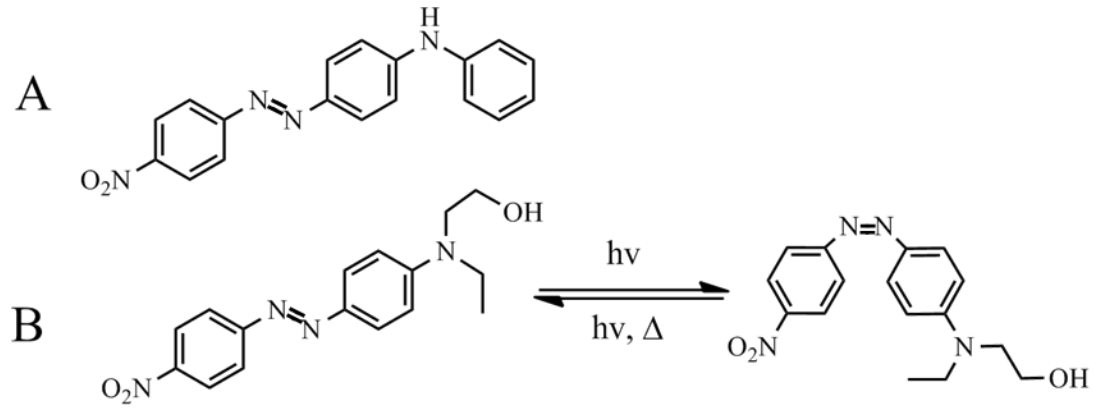

Figure 3.2: Structures of trans Disperse Orange 1 (A) and Disperse Red 1 (B), and the reversible photo-isomerisation of Disperse Red 1 from *trans* (left) to *cis* (right).

As discussed in section 2.2 absorption of light by the molecule induces an electronic excitation from which the molecule can relax to either the *trans* or *cis* isomer. As the thermal barrier for *cis* to *trans* conversion approximate to k_BT whereas the barrier is very large for *trans* to *cis*, the molecules relax thermally and when left in the dark the solution becomes 100% *trans* isomer. Under constant excitation there is, therefore, competition between the productive photo-isomerisation to the *cis* isomer and the unproductive decay to *trans* isomer via both photochemical and thermal processes leading to a photostationary state (PSS).

The change in absorption spectrum as a result of isomerisation from *trans* to *cis* isomer allows the kinetics of the process to be easily observed through absorption spectroscopy. The system is robust with no side–reactions, allowing clean measurements and relatively straight forward kinetics calculations to be performed. Whilst the molecules are well studied there are several challenges for performing measurements in conventional systems.

Both of the dyes fall into the "push–pull" class of azobenzene derivative. This increased electron delocalisation accelerates the rate of thermal *cis* to *trans* isomerisation and provides a strong dependence on solvent polarity [118, 119, 120]. Measuring the photoisomerisation quantum yields of push–pull azobenzenes in polar

solvents is challenging because of the fast thermal isomerisation and there are, to our knowledge, no previous measurements in solution at room temperature. A very recent review[121] cites only one study[122], carried out at low temperature to prevent the thermal process. Further, in non-polar solvents the solubility of the dyes is greatly reduced, for example, in pentane Disperse Orange 1 has a solubility of ~$1x10^{-6}$ M. This is too low for a measurement to be made in a standard UV–Vis spectrometer using a 1 cm cuvette where, for such a dye these, the detection limit lies at ~$5x10^{-5}$ M. The increase in path-length possible through the use of HC–PCF allows the UV–Vis spectrum and reaction kinetics of the dyes to be studied, even at these very low concentrations, whilst maintaining extremely small sample volumes of around 90 nL.

3.2. Development of the Experimental Design

The experimental setup for the measurement of the reversible photoisomerisation of azobenzene-based dyes underwent a significant period of development, through which incremental improvements were made. For example, modifications were made to allow a greater spectral range to be recorded or faster measurements to be made. This section outlines the development of the apparatus used through its various forms, highlighting the improvements that were achieved at each stage.

3.2.1. Initial Experimental Design

The initial experimental design aimed for the simplest setup to allow the measurements to be made. The setup is shown in Figure 3.3. A diode laser (Newport, Cyan 488 nm) was used for excitation of the dye molecules at 488nm, with a halogen lamp as a broadband light source for the UV–Vis measurements. The halogen lamp was collimated through a series of lenses and both sources were then co-aligned through the use of simple beam splitters and coupled into the sample fibre. The light from the sample fibre was then collimated and coupled into a multi-mode fibre which was coupled to grating spectrometer (Ocean Optics USB2000+). The spectrometer is connected to a computer through which the recording of spectra is automatically completed using the Ocean Optics software package. A small portion, ~8%, of the light is directed via beam splitter to a CCD camera to allow the guided beam profile of the light sources to be monitored.

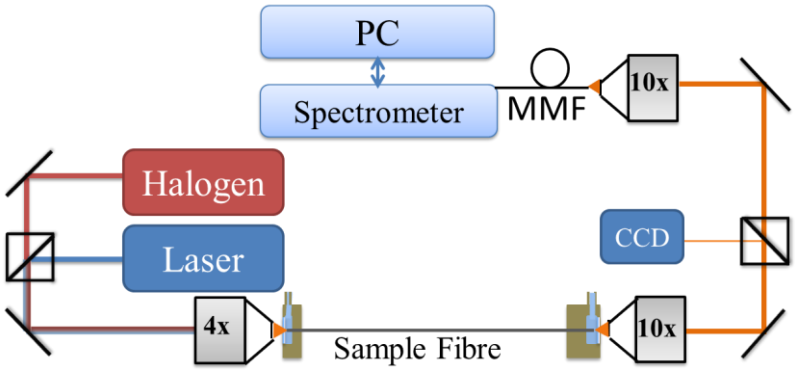

Figure 3.3: Schematic of the initial experimental setup. The broadband halogen lamp and 488nm laser sources are co-coupled into the sample fibre. The output of the fibre is then coupled into a multimode fibre (MMF) connected to a grating spectrometer. Mode profiles are monitored using a camera (CCD).

The fibre was held in place by two liquid cells, each with a glass window to allow for the in and out coupling of the light sources to the fibre. For the photochemistry measurements the window was 0.5 mm thick. Optimal coupling of light into the fibre was achieved by matching the numerical aperture of the (NA) of the coupling objective to that of the fibre. For an index–guiding fibre the NA can be approximated by

$$NA = \sqrt{n_1^2 - n_2^2} \qquad \text{Equation 3-1}$$

where n_1 and n_2 are the refractive indices of the core and cladding materials, respectively. For a HC–PCF the N.A can be roughly approximated by

$$NA = \frac{\lambda}{2D} \qquad \text{Equation 3-2}$$

where λ is the wavelength of light to be coupled and D is the core diameter of the fibre.

For a fibre that is filled with a solution the NA will be changed further as the air to glass and glass to liquid interfaces will act as a different powered lenses as shown in Figure 3.4. Therefore, the chosen objective must match the NA_{eff} for the fibre–liquid–glass combination used to allow for the most efficient coupling of light into the fibre.

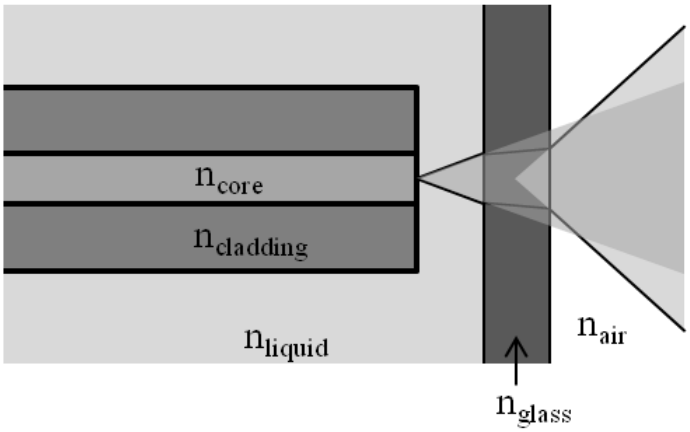

Figure 3.4: Schematic of the effect of the glass window and liquid filling of the PCF on NA for in and out-coupling of light. For a hollow core PCF $n_{core} = n_{liquid}$. The increase in NA can be calculated using Snell's law as discussed in chapter 2.1.3.

The first generation of the liquid cells that were used on the initial setup are shown in Figure 3.5. The sample cells hold the fibre in place and have ports to allow the entry and exit of sample liquids; this was achieved via a syringe pump. Due to the microscopic fibre structure, fine 0.22 μm filters (Millipore Millex (PES), Fischer Scientific) have to be used on the syringes to prevent any particulate contamination from clogging the fibre, hindering filling. The fibre is held in place and liquid flow directed using a PTFE insert, this caused the undesirable effects of dead volume and nucleation points for bubble formation, hindering the experiments. Whilst a bubble appearing in the central fibre core is instantly spotted by a large reduction in fibre guidance, if bubbles propagate through the fibre cladding holes, the quality of the guided mode is affected but more subtly, this can be hard to notice during an experiment and therefore precautions, such as degassing syringes, must be taken. The Teflon insert was later replaced by a more robust completely metal design.

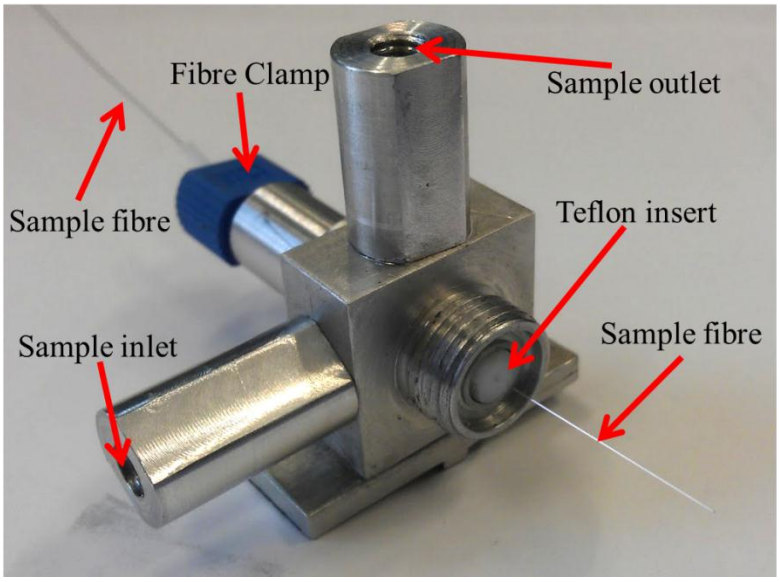

Figure 3.5: First generation liquid cell, the sample fibre is cleaved ~0.5mm from the Teflon insert. The windowed cap screws into place, sealed with a PTFE O- ring, to allow for coupling into and out of the fibre. The sample fibre shown exiting the front face is subsequently cleaved to within 0.5 mm of the Teflon surface. Solutions are introduced through the inlet port. The outlet port allows for initial filling of the cell dead volume at the in-coupling fibre end and sample removal at the output.

The first problem encountered with this design was due to the relative intensities required for the excitation laser and probing broadband source. With the spectrometer integration time set at a sufficiently long value to measure the

broadband spectrum the high intensity 488 nm laser saturated the signal. The use of a notch filter to remove this laser line, as would be done in a fluorescence measurement, was not possible since the wavelength lies in the most desired part of the absorbance spectrum for measurements. To counter the saturation problem shutters had to be added to the setup, between each of the light sources and the sample fibre, and between the sample fibre and the spectrometer, as shown in Figure 3.6.

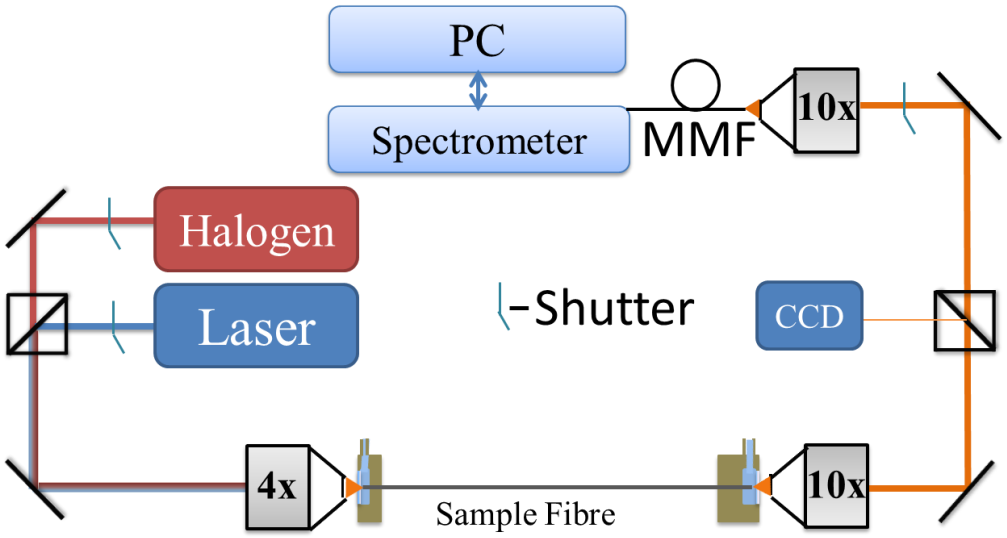

Figure 3.6: Schematic of experimental setup. Additional shutters added between the light sources and the fibre and between the fibre and the spectrometer.

The use of shutters introduced the complication of automation, which was achieved by controlling the shutter operation and spectral acquisition via a MATLAB computer program. This insured that the spectrometer was isolated from the laser during excitation. During one iteration of the program, the excitation source is switched on to irradiate the sample for a predetermined exposure time whilst the broadband light is off. The excitation source is then switched off and the broadband light source switched on to enable the spectrometer to acquire a spectrum. The whole cycle repeats until the photoreaction is complete or the photo-stationary state is reached.

Whilst absorption spectra could now be measured, the need to move to such a pump – probe style measurement scheme reduced the rate at which spectra could be measured, and for reversible processes, such as the photoisomerisation of azo–dyes,

reduced the amount of product formation that could be observed, due to the continual competition between productive photoisomerisation and thermal relaxation.

A further problem with the initial setup arose from the divergent, multi-mode, output of the halogen lamp, which was partially coupled into a MMF before being collimated and co-aligned with the laser beam. With different input beam profiles, the fibre mode into which the two sources can be coupled varied. The perfectly collimated laser beam couples into the fundamental mode of the fibre core whereas the more divergent broadband source couples into multiple modes in the sample fibre. This creates the situation where the excitation light and probe light penetrate different portions of the sample within the fibre.

Examples of the beam profile measured from the fibre output for each light source are shown in Figure 3.7. It can be seen that the modes are very different, with the halogen lamp featuring a TEM 01* "donut" mode whereas the laser is in a uniform fundamental mode.

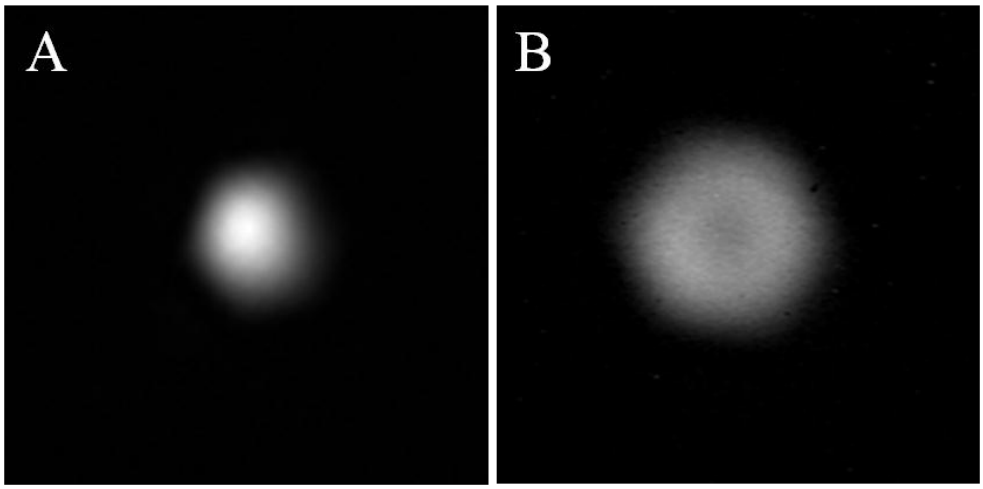

Figure 3.7: Guided mode of (A) the laser and (B) the broadband halogen lamp, through a kagomé hollow core fibre.

The output intensity of the halogen lamp falls off greatly below a wavelength of 450 nm, as shown in Figure 3.8. When this combined with increased fibre losses at these wavelengths, the guided light intensity is reduced to a point where there is insufficient light to record spectrum in this region. An example of the first "successful" measurement using this setup is shown in Figure 3.9 where the failure

to satisfactorily measure the complete spectrum of the Disperse Red 1 dye in cyclohexane is clearly evident.

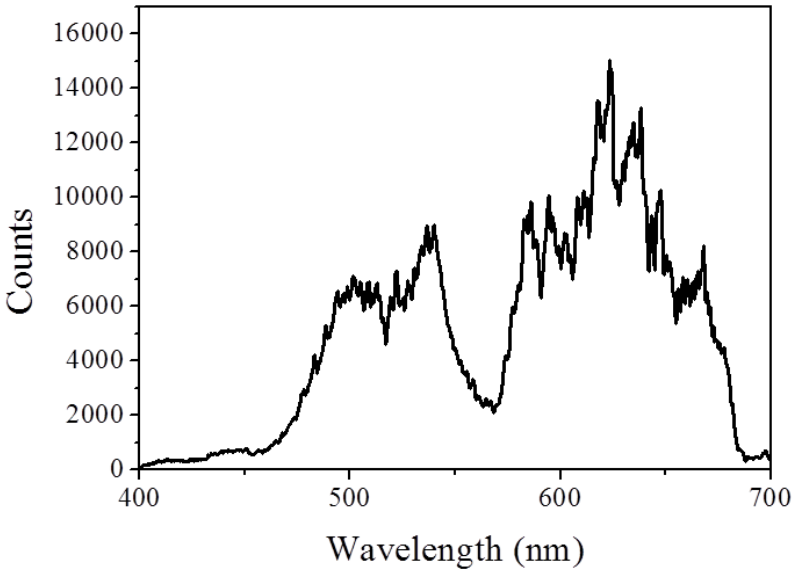

Figure 3.8: Measured spectral output from the halogen lamp after guidance through 30 cm of kagomé HC–PCF filled with cyclohexane.

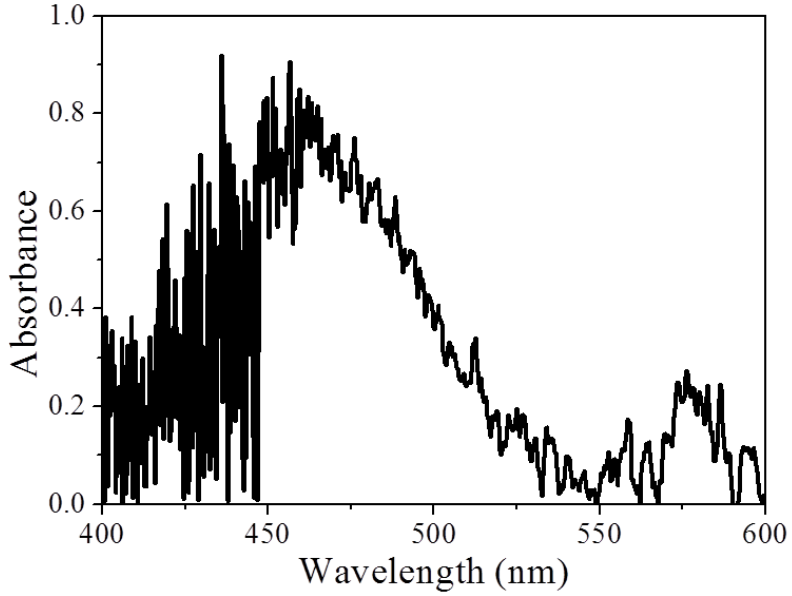

Figure 3.9: Measured spectrum of Disperse Red 1 in cyclohexane in 30 cm of kagomé HC–PCF.

3.2.2. Improving the Experimental Design

After the shortcomings of the initial design had been realised, several improvements were made. The halogen broadband source was replaced by a xenon lamp, providing a broader spectral output. The main loss of light in the low–wavelength region was now due to fibre losses and not the light source, and the spectral output after a 30 cm length of toluene filled HC–PCF is shown in Figure 3.10. Whilst there is still significant reduction in guided light below 450–500 nm, there is measurable output down to close to 400 nm, near the short-wavelength edge of the absorption spectra of the dyes of interest in this study. Further development is underway at MPL to increase the guidance efficiency of filled HC–PCF to shorter wavelengths.

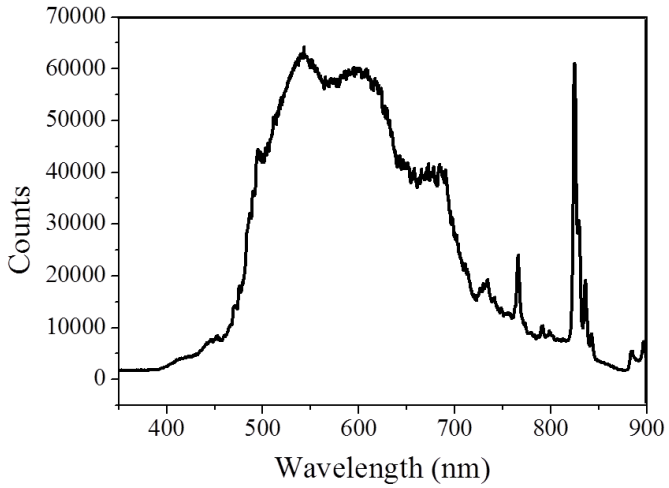

Figure 3.10: Output spectrum of the Xenon lamp source used in the improved experimental setup after guidance through 30 cm of toluene filled kagomé PCF.

In addition to the change of broadband probe light source, a reference arm was added to the setup to allow for correction of any fluctuation in the lamp output when plotting the measured spectra. This setup is shown in Figure 3.11. The reference arm of the setup does not pass through a second piece PCF. This is because any variation in the coupling of the reference fibre would have no correlation with variation of the sample fibre coupling. Therefore only gross fluctuation in the lamp is measured as a reference, and stability of the in-coupling to the sample fibre is assumed. To accommodate the two measurement signals the spectrometer was changed to an Ocean Optics Jazz^{TM} Spectrometer which has two fibre–coupled inputs.

The mode of construction of the liquid cells was also improved, such that they were of solid metal construction, with all of the input and output channels built in, as shown in Figure 3.12.

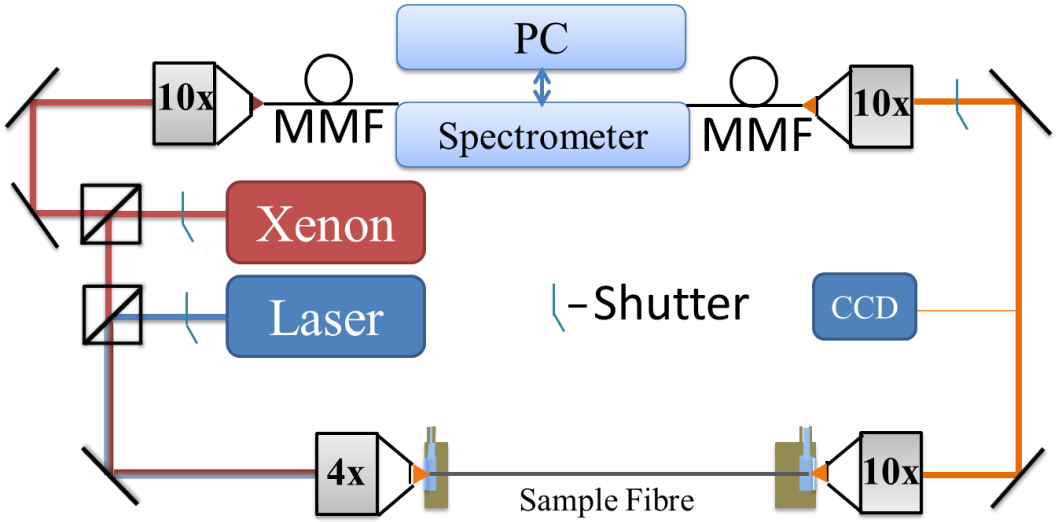

Figure 3.11: Schematic of third revision of the experimental design. A reference arm (top left) monitors fluctuation in the new xenon lamp light source.

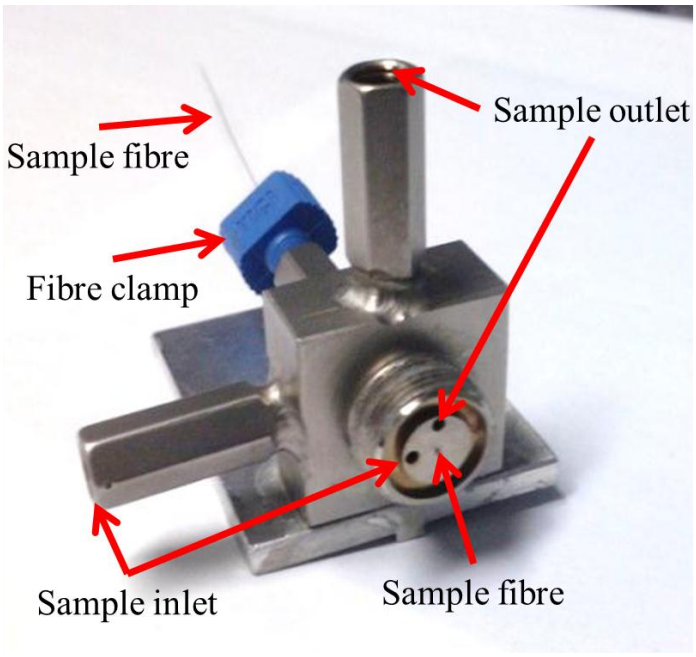

Figure 3.12: Final liquid cell design showing input and output ports and sample fibre. A glass–windowed cap screws over the face plate sealed with a PTFE O–ring,

An example of a spectrum recorded on this setup is shown in Figure 3.13 There is clearly an improved spectral measurement range. The use of the spectra recorded

from the lamp reference arm allowed noise introduced by fluctuations in the lamp output to be subtracted. When this subtraction was performed on the solvent reference, measured before dye was introduced, and subsequent measurements of the dye spectrum this led to a considerable reduction in noise compared to the previous designs

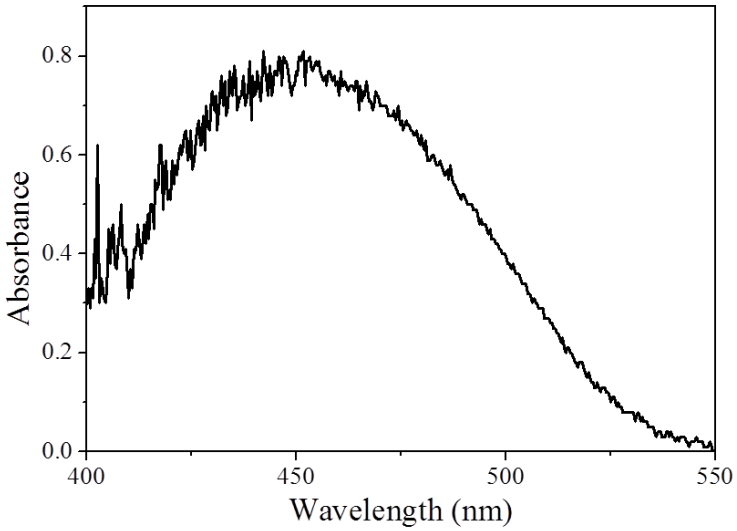

Figure 3.13: Disperse Red 1 in toluene measured in 30 cm of kagomé PCF using xenon lamp source.

3.2.3. Final Experimental Design

Whilst the use of a xenon lamp as the broadband light source provided sufficient guided bandwidth to measure the required spectra, the problem remained of having two very different beam properties between pump and probe. To reach the goal of having perfect coincidence of the excited sample volume and measured sample volume, the sources required spatial filtering to bring them into the same mode. This was achieved by first coupling both sources into an endlessly single mode (ESM) fibre placed before the sample fibre. As the ESM only guides a limited number of spatial modes, as described in section 2.1.3.2.1, and the divergence of the output depends only on the NA of the ESM, both light sources are perfectly co-aligned and modally filtered. On in-coupling to the sample fibre both sources could now be coupled into the fundamental mode, giving maximum overlap with the sample

solution in the core, whilst reducing any measured surface effects such as dye adhesion. The final experimental design is shown in Figure 3.14.

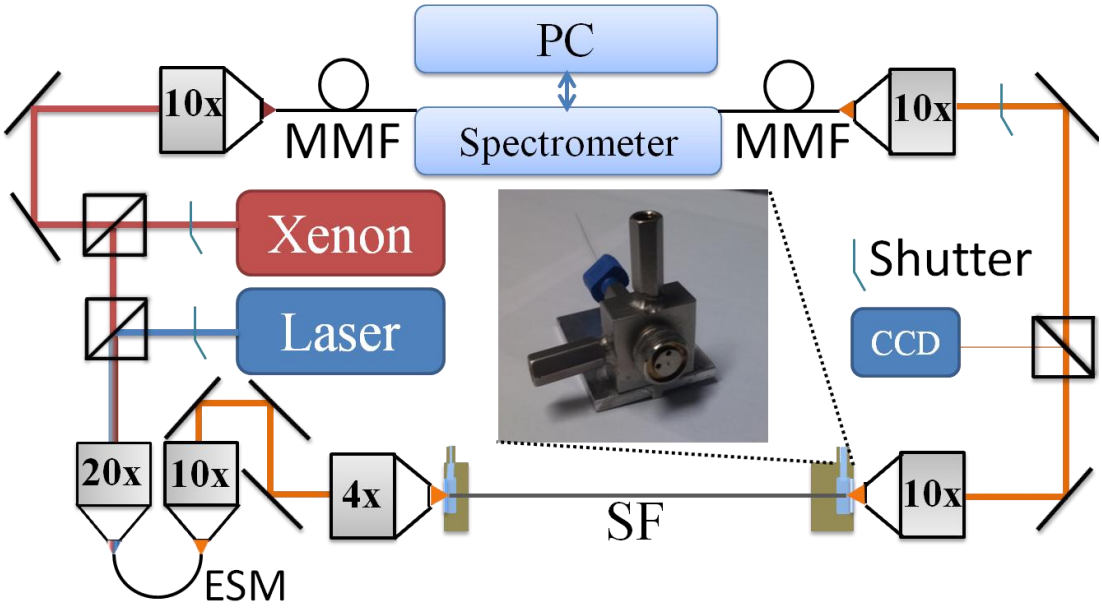

Figure 3.14: Schematic of the final experimental setup for photoisomerisation experiments. The 488 nm laser source and the broadband xenon lamp source are co-aligned through and coupled into a short piece of endlessly single mode fibre (ESM) for spatial filtering before being coupled into the HC–PCF containing the sample (SF). The transmitted light, as well as a reference beam are collected by the dual-channel spectrometer via multimode fibres (MMF). The laser, lamp and input to the spectrometer are passed through shutters, controlled automatically via computer (PC). Inset: sample cell for introduction of liquid to the sample fibre.

3.3. Experimental Methods

3.3.1. Materials

The Disperse Red 1 and Disperse Orange 1 dyes used in the presented work were purchased from Sigma Aldrich at 99% purity. All solvents were HPLC grade and were purchased from Fisher Scientific. All the fibres were custom made by the fabrication team at MPL. The objectives used in the experimental setups for all of the work were of the Olympus Plan Achromat series with visible transmission, obtained from ThorLabs.

3.3.2. Conventional Cuvette Measurements

For comparison with the novel measurements of photoisomerisation made in HC–PCF, initial, conventional measurements were performed in using a Cary 3LO UV–Vis spectrometer. Samples of 10^{-4} M solutions of both disperse red 1 and disperse orange 1 were irradiated for *ca* one hour at the wavelength of their peak absorption as shown in Table 3. The irradiation source used was the excitation output from a Jobin-Yvon Fluoromax P fluorometer. After irradiation, samples were transferred to the UV–Vis spectrometer as quickly as possible, (*ca* 19 seconds), and absorption measurements commenced immediately. The temperature through was that of the lab at ca. 22 degrees centigrade.

Measurements were run on the samples approximately every minute until no change in the spectrum was observed.

Solvent	Disperse Red 1	Disperse Orange 1
Cyclohexane	450 nm	437 nm
Toluene	471 nm	448 nm

Table 3: Absorption maxima for the azo-benzene based dyes Disperse Red 1 and Disperse Orange 1

Due to the time involved in moving the sample from excitation to the spectrometer and the length of time for the acquisition of the spectrum, ~30 s, the photo-isomerisation from the *trans* to *cis* isomer could not be followed, only the thermal process from the *cis* to *trans*.

Further measurements were recorded using the experimental system for the fibre measurements, by placing a 1 cm cuvette in the beam path of the co-aligned pump and probe sources. This allowed faster measurements to be made, but the excitation area in the cuvette was ~0.2 cm^2 compared to the previous measurements where ~0.8cm^2 was excited. As a smaller proportion of the sample was irradiated the total quantity of *cis* isomer produced, with respect to the total sample volume, was less.

3.3.3. HC–PCF Measurements

For measuring the photoisomerisation process in HC–PCF a kagomé fibre with a 10 μm pitch and a 19 μm core diameter was used. A high-resolution scanning electron micrograph (SEM) of the fibre is shown in Figure 3.15. As discussed in section 2.1, for PBG-HC–PCF, a core mode coincides with a photonic band-gap in the micro-structured cladding, resulting in the formation of ultra-low loss (~1 dB km^{-1} in the best cases) guided modes over restricted bandwidths of typically around a hundred nanometres. In contrast, the guidance mechanism of kagomé HC–PCF is based on the reduced coupling between the core mode and the cladding modes, resulting in higher losses in the order of 1 dB m^{-1}. Whilst this is a large reduction in guidance capability it is still far better than in a capillary, and the kagomé HC–PCF has the advantage of giving a much broader spectral guidance band than the PBG-HC–PCF. Therefore, the kagomé HC–PCF is the fibre of choice for broadband spectral measurements.

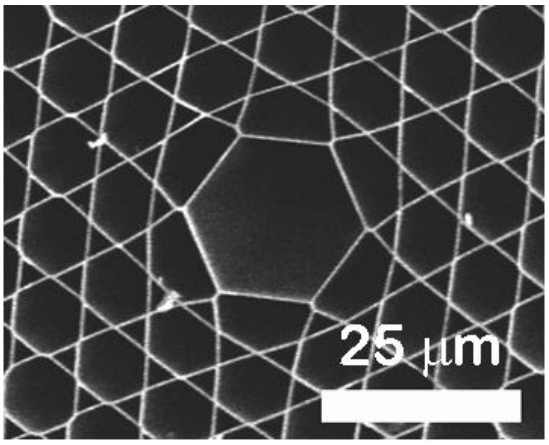

Figure 3.15: High-resolution scanning electron micrographs of a kagomé HC–PCF with a core diameter of 19 μm.

Measurements were performed using the final experimental setup shown in Figure 3.14, using ~30 cm of the kagomé HC–PCF. The fibre core contains a sample volume of 2.8 nL cm^{-1} giving a total volume measured of ~90 nL, which was 6 orders of magnitude lower than the cuvette measurements. The increased path length allowed measurements to be performed on solutions of 10^{-5}–10^{-6} M concentration. Initially measurements were carried out on each dye in two solvents, cyclohexane and toluene due to the high solubility in toluene and ability to compare to previous studies in the non–polar cyclohexane.

When measurements were attempted in these solvents the coupling of light into the sample fibre was found to be problematic. The transmission properties of the kagomé HC–PCF when filled with the solvent toluene were investigated by the cut-back method previously discussed in Chapter 2.1.7 and the measured, normalised, transmission spectrum is shown in Figure 3.16.

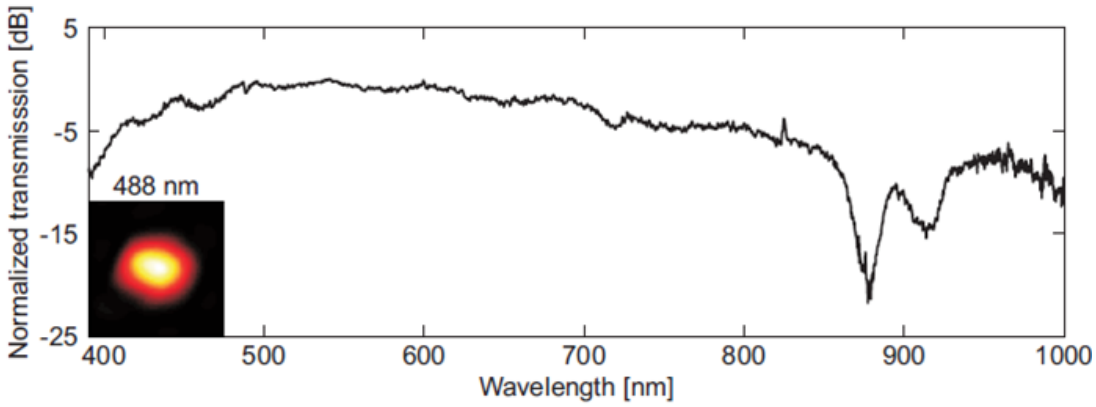

Figure 3.16: Transmission spectrum of the kagomé fibre normalised to the super-continuum source when filled with Toluene. The high refractive index of toluene makes the fibre–index guiding and the transverse irradiance profile at 488nm is shown in the inset.

The fibre is seen to exhibit broadband guidance in the visible up to 860 nm. However the transverse irradiance profile measured using the CW excitation source at 488 nm displayed an asymmetric mode profile (inset Figure 3.16), indicating coupling into multiple higher–order modes. Consequently the loss of the fundamental mode could not be measured. The reason for the multimode behaviour of the fibre when filled with toluene can be understood as the refractive index of toluene is higher than that of fused silica. The fibre therefore becomes index-guided

with a V parameter, determining the number of guided modes, given by Equation 3-3,

$$V_{PCF}(\lambda) = 2\pi\Lambda/\lambda\sqrt{n_{core}^2 - n_{eff}^2} \qquad \text{Equation 3-3}$$

where λ is the wavelength of operation, Λ is the pitch of the cladding structure and n_{core} and n_{eff} are the effective refractive indices of the core and the cladding[123,124]. The number of guided modes can be approximated by $V^2/2$ giving guidance of approximately 90 modes. It was, however, possible to minimize the number of guided modes and maximize the irradiance concentrated in the core region by careful optical alignment, keeping the bend radius of the fibre large (> 15 cm) and avoiding twisting of the fibre. Whilst this did not prevent measurements from being performed it increased the fibre losses to ~2.5 dB m^{-1}, also as the in-coupling was so unstable there was more noise between measurements due to fluctuation in the guided modes.

A solution to this problem is underway through the construction of kagomé HC–PCF utilising higher refractive index glasses such as SF6 which has a refractive index of 1.82 in the visible region[125]. This will allow the use of any solvent for sensing within PCF.

To provide results with the fibre guiding in a clean single mode with low loss, further measurements of Disperse Red 1 in pentane, which has a refractive index of ~1.35, were performed. Using pentane, a solvent in which the dye is highly insoluble, only low concentrations can be achieved. Ability to measure the dye in this solvent therefore highlights the detection sensitivity of PCF and there are no previously reported equivalent results for these dyes in pentane.

Kinetic Modelling

The results from the photoisomerisation measurements were fitted numerically by integrating the three coupled rate equations governing the populations of the states of the two isomers, *trans* and *cis*, and the transition state, achieved through irradiation. The equations being solved along with the continuity condition are given in Equation 3-4–3.7

$$\frac{\partial n_T}{\partial t} = -\frac{I_p}{h\nu_p}\sigma_T n_T(t) + \Gamma_{TS-T} n_{TS}(t) + \gamma_{C-T} n_C(t) \qquad \text{Equation 3-4}$$

$$\frac{\partial n_C}{\partial t} = -\frac{I_p}{h\nu_p}\sigma_C n_C(t) + \Gamma_{TS-C} n_{TS}(t) - \gamma_{C-T} n_C(t) \qquad \text{Equation 3-5}$$

$$\frac{\partial n_E}{\partial t} = \frac{I_p}{h\nu_p}\left(\sigma_T n_T(t) + \sigma_C n_C(t)\right) - n_{TS}(t)(\Gamma_{TS-T} + \Gamma_{TS-C}) \qquad \text{Equation 3-6}$$

$$Continuity, \qquad n_{Total} = n_T + n_C + n_{TS} \qquad \text{Equation 3-7}$$

Where $n_{T,C,TS}(t)$ are the normalised number densities in the *trans*, *cis* and *transition* states, I_p and $h\upsilon_p$ are the power density and photon energy of the pump light, σ_T and σ_C are the absorption cross-sections at the pump wavelength of the *trans* and *cis* isomers, Γ_{TS-T} and Γ_{TS-C} are the rate constants of decay from the transition state to the *trans* and *cis* isomers and γ_{C-T} is the thermal rate from *cis* to *trans* isomer. These correspond to the absorption and decay processes shown in Figure 3.17. As molecules are not created or destroyed the rate equations are linked by a continuity equation ensuring molecule number is preserved.

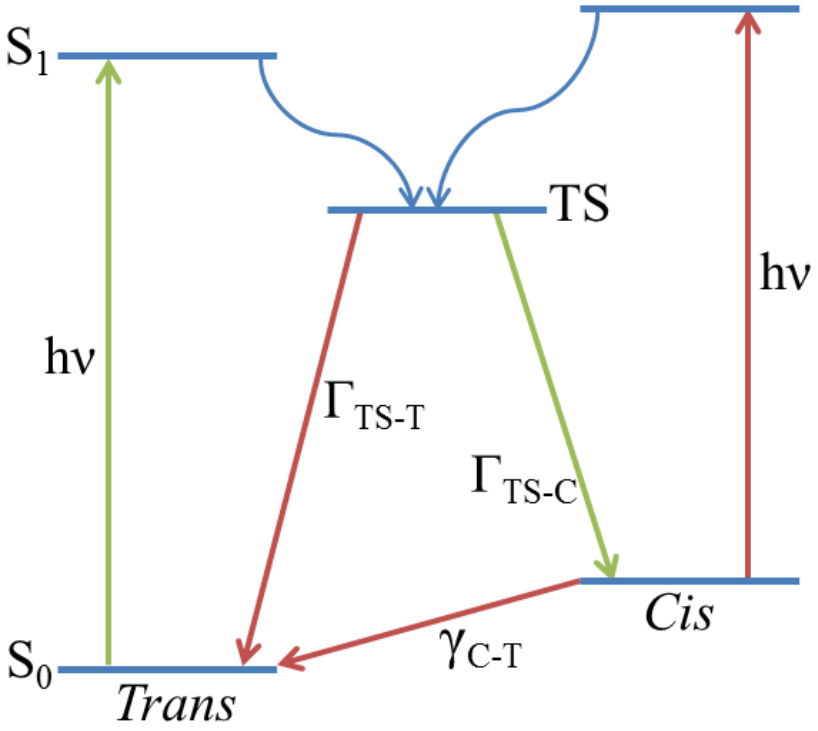

Figure 3.17: Energy level diagram for the *cis-trans* isomerisation of azobenzenes, showing the processes and associated parameters used in the numerical model. Excitation of *trans* and *cis* isomers populate a common transition state (TS).

The incident intensity, I_0, is known (its measurement is straightforward since the whole of the irradiated sample is monitored). The absorption cross-sections of both the *trans* and *cis* isomers, along with the fibre loss per unit length, are also known parameters. The value for the *trans* isomer can be determined easily by measuring the absorption spectrum of a sample that has been left in the dark and is 100% *trans*. However, determination of the value for the *cis* isomer requires knowledge of the composition of the PSS. The composition of the PSS is obtained by monitoring the decrease in absorbance on formation of the PSS, at a wavelength where only the *trans* isomer absorbs; in the present case, this corresponds to the maximum of the measured *trans* absorption spectrum[118]. The value of the thermal isomerisation rate constant, Γ_{C-T}, can be measured independently as it is a simple exponential decay and can therefore be used as a fixed parameter in the photoisomerisation model. Applying the model to the temporal evolution of the absorbance spectrum, measured experimentally during the photo-induced conversion of the all-*trans* sample to the

PSS, yields the ratio of $\Gamma_{TS\text{-}T}$ and $\Gamma_{TS\text{-}C}$. The quantum yield for *trans* to *cis* photoisomerisation can then be determined, details are given in appendix B.

Due to the long path lengths involved in the PCF measurements the model also has to take into account the decrease in intensity of the pump–probe light throughout the length of the fibre. The decrease in intensity along fibre is due to both the absorption of light by the sample and the intrinsic loss of the fibre itself. Integration is therefore carried out through both time and space. However, due to the very high computational load of a complete integration through space a discrete integration is performed by selecting a desired length over which there is an insignificant change in intensity, say 0.5 cm.

In the model, the fibre is split up into a number (x) of length segments and the molecular constitution, i.e. the number of molecules in each state, *trans*, *cis*, or transition state, are calculated for the first segment. The light leaving the segment, reduced by fibre loss and absorption, is then used as the input intensity for the next segment, until the composition of the whole fibre is known. The time integration is then moved on by one timestep and the space integration performed again. The intensity incident on each segment is calculated using Equation 3-8.

$$I_p(z) = I_n 10^{-\int_0^z \alpha(\xi) d\xi} \qquad \text{Equation 3-8}$$

where I_p is the intensity at point z along the fibre and $\alpha(\xi)$ is the combined position-dependent attenuation due to fibre loss and molecular absorption and I_n is the irradiation intensity entering the previous segment of the fibre.

The integration over the fibre length is a non-divergent process; the length of each segment only affects the accuracy of the final result. The fibre was split into segments equivalent to 0.5 cm as a balance between accuracy and computational load. This is due the large computational time consideration for integration over time and space with very small segment lengths.

Time integration is processed using a standard fourth–order Runge–Kutta method (RK4) for which the expressions are given in equations 3-9 to 3-13.

$$k_1 = hf(y_n, t_n) \qquad \text{Equation 3-9}$$

$$k_2 = hf(y_n + \frac{k_1}{2}, t_n + \frac{h}{2}) \qquad \text{Equation 3-10}$$

$$k_3 = hf(y_n + \frac{k_2}{2}, t_n + \frac{h}{2}) \qquad \text{Equation 3-11}$$

$$k_4 = hf(y_n + k, t_n + h) \qquad \text{Equation 3-12}$$

$$y_{n+1} = y_n + \frac{(k_1 + 2k_2 + 2k_3 + k_4)}{6} \qquad \text{Equation 3-13}$$

where h is the time-step, f is the function being solved and y_n is the current value of function.

Within the model the timestep (t_n) is only moved on once each the discrete integration throughout the length segments has been completed. The current time-step is therefore progressed outside of the RK4 method which is modified as shown in the code section in Figure 3.18.

```
public SegmentMolecularState nextState(double time, double intensity) {
        double k1 = time * g(getTrans(), getCis(), getExcited(), intensity);
        double l1 = time * f(getTrans(), getCis(), getExcited(), intensity);
        double m1= time * e(getTrans(), getCis(), getExcited(), intensity);
        double k2 = time * g(getTrans() + k1 / 2,  getCis() + l1 / 2, getExcited() + m1 / 2, intensity);
        double l2 = time * f(getTrans() + k1 / 2,  getCis() + l1 / 2, getExcited() + m1 / 2, intensity);
        double m2= time * e(getTrans() + k1 / 2,  getCis() + l1 / 2, getExcited() + m1 / 2, intensity);
        double k3 = time * g(getTrans() + k2 / 2,  getCis() + l2 / 2, getExcited() + m2 / 2, intensity);
        double l3 = time * f(getTrans() + k2 / 2,  getCis() + l2 / 2, getExcited() + m2 / 2, intensity);
        double m3= time * e(getTrans() + k2 / 2,  getCis() + l2 / 2, getExcited() + m2 / 2, intensity);
        double k4 = time * g(getTrans() + k3, getCis() + l3, getExcited() + m3, intensity);
        double l4 = time * f(getTrans() + k3, getCis() + l3, getExcited() + m3, intensity);
        double m4= time * e(getTrans() + k3, getCis() + l3, getExcited() + m3, intensity);
        double znew = getCis() + (l1 + 2 * (l2 + l3) + l4) / 6;
        double ynew = getTrans() + (k1 + 2 * (k2 + k3) + k4) / 6;
        double wnew = getExcited() + (m1 + 2 * (m2 + m3) + m4) / 6;
        return new SegmentMolecularState(ynew, znew, wnew, _paramiters);
```

Figure 3.18: Implementation of the RK4 method in the model code. Where getTrans()… refers to the number of molecules in the *trans*, *cis* and *transition* states in the current segment at the current time. These values get updated through one iteration of the RK4 method and stored for the next time step for this segment. g, f and e refer to the *trans*, *cis* and *transition* states respectively. The program is split into two sections, one for calculating the thermal rate constant for the relaxation of *cis* to *trans* isomers, this value is then passed onto the second section for the calculation on the ratio of *trans-cis* and *cis-trans* photoisomerisation rates.

A further complication is added to the model by the limitations imposed by the experimental setup. The need to use shutters to block the excitation light from the spectrometer means that irradiation is not constant, and a pump–probe regime is used. There are therefore periods during the measurement of the photoisomerisation when the excitation light is on interspersed with periods when it is off. During the periods when the excitation light is off, molecules in the *cis* form will continue to revert to the *trans* via the thermal pathway so this has to be taken into account by the model.

More details of the model program is given in Appendix B.

3.4. Results and Discussion

3.4.1. Cuvette Measurements

The results of the comparative cuvette measurements, of the thermal isomerisation for Disperse Red 1 and Disperse Orange 1 after excitation, are shown for 100 µM toluene solutions in Figure 3.19 and cyclohexane solutions in Figure 3.20. The measurements were made in a standard UV–Vis spectrometer as detailed in chapter 3.2.1. The direction of thermal isomerisation after excitation is indicated by the arrow in each case.

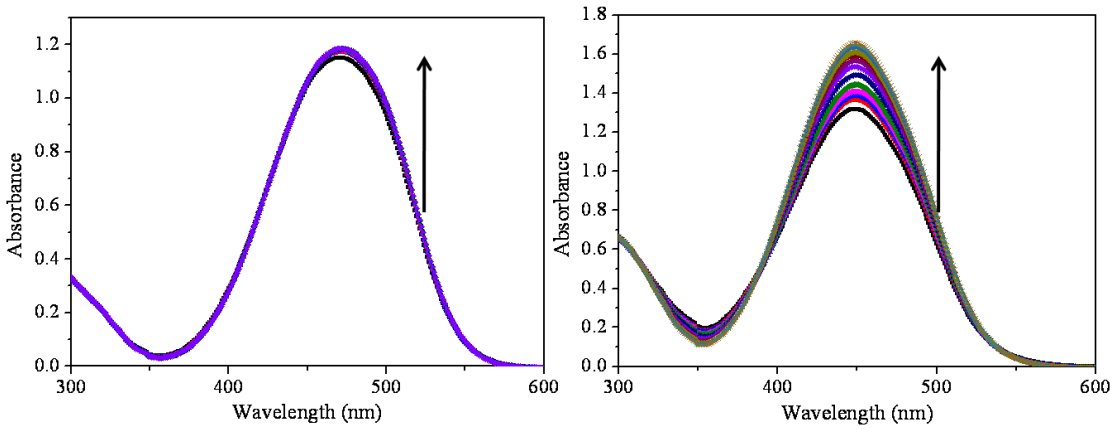

Figure 3.19: Absorbance spectra of 10^{-4} M Disperse Red 1 (left) and Disperse Orange 1 (right) in toluene measured in a standard spectrometer after irradiation, the arrow indicates the temporal evolution of the spectra as the sample thermally reverts from the *cis* to the *trans* isomer.

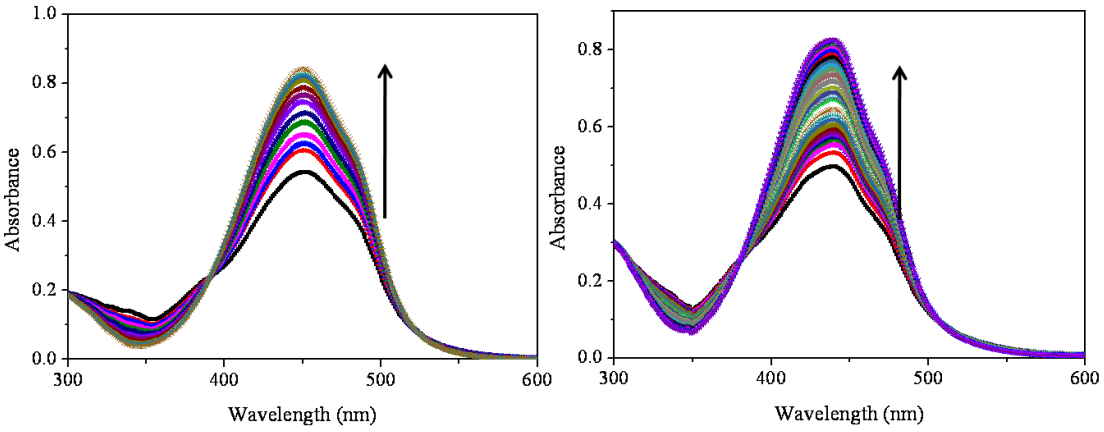

Figure 3.20: 10^{-4}M Absorbance spectra of 10^{-4} M Disperse Red 1 (left) and Disperse Orange 1 (right) in cyclohexane measured in a standard spectrometer after irradiation, the arrow indicates the temporal evolution of the spectra as the sample thermally reverts from the *cis* to the *trans* isomer.

For the case of Disperse Red 1 in toluene the thermal rate is significantly faster, reducing the fraction of *cis* isomer that can be formed and subsequently measured in the spectrometer, this highlights the limitation of this method for measuring fast processes.

Whilst these measurements were taken only as a reference for spectra and thermal rates, the method could be improved greatly, as has been done in the literature, by using faster grating spectrometers and in-situ irradiation sources. Due to the delay between excitation and the first spectrum being recorded the initial measured sample composition is significantly different from the PSS composition, especially in the case of faster thermal relaxation rates, making modelling the data difficult.

3.4.2. HC–PCF Measurements

As shown in Figure 3.21, photoisomerisation of *trans* Disperse Red 1 results in a decrease in intensity of the visible absorption band between 400 and 550 nm. Similar behaviour is seen for Disperse Orange 1. Figure 3.21 compares spectra recorded for a 100 μM solution in a 1-cm cuvette (in a conventional UV–Vis spectrometer as shown above) with those measured for a 5 μM solution in a 30-cm HC–PCF.

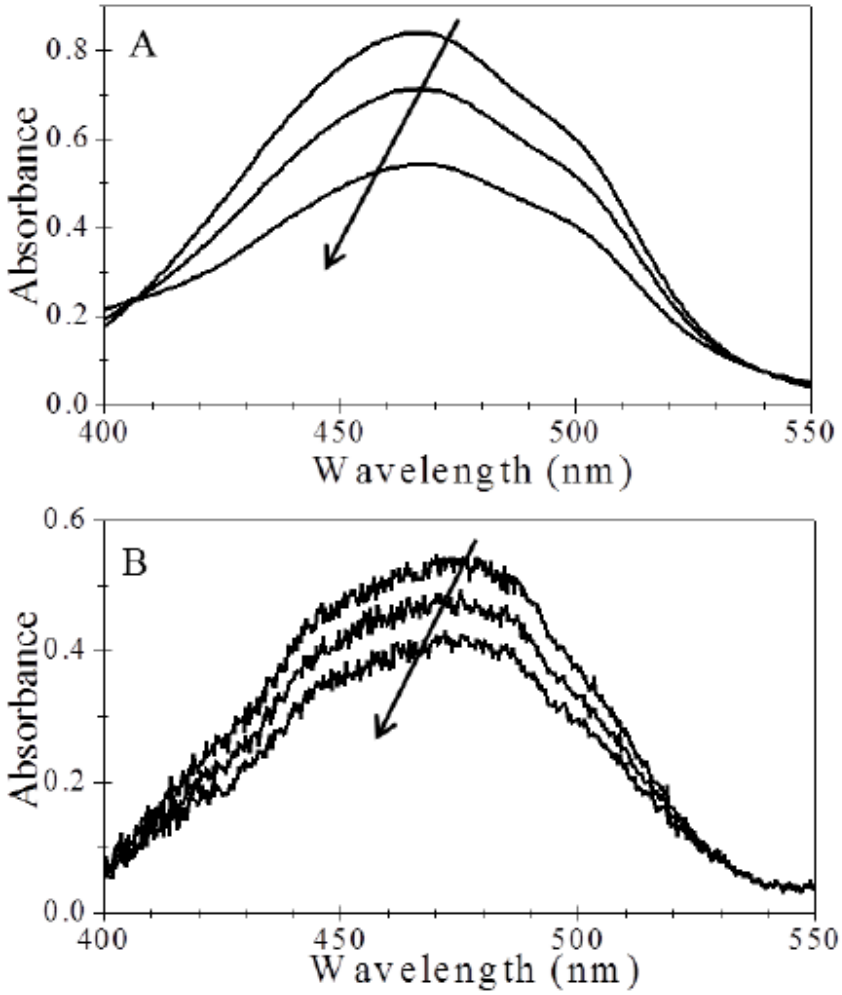

Figure 3.21: Absorption spectra of Disperse Red 1 in toluene measured during photoisomerisation in (A) a 1-cm cuvette, at 100 μM (in a UV/vis spectrometer, scan time 45 s) and (B) in a 30-cm a kagomé PCF at 5 μM (acquisition time 500 ms). The arrow indicates the direction of photoisomerisation from the *trans* to the *cis* isomer.

The spectral profiles are in good agreement; however, the absorbance measured in the PCF is somewhat lower than that predicted on the basis of the Beer–Lambert law. This can be attributed to adsorption of dye molecules to the fibre walls, where they

are not exposed to guided light, which reduces the effective sample concentration. Allowing the sample to flow through the fibre saturates the surface and the recorded absorbance approaches that predicted (Figure 3.22). The issue is greatest when attempting to measure the dyes in poor solvents, such as cyclohexane and pentane, in the extreme case of pentane where the solubility of the dye is ~$5x10^{-6}$ M the dye was completely removed from the solution by the filter (Millipore Millex, Fisher Scientific) being used on the syringe, which consequently had to be removed. Further confirmation of the effect of surface absorption is given in chapter 4 where fluorescence spectroscopy is used to distinguish between molecules in the bulk solution and those attached to the fibre surface.

As a result of the tight confinement of the guided light in the core of the sample fibre, very low source powers are needed to produce sufficient power density to induce the photochemical process. Consequently, the low-power broadband xenon lamp, intended for use as the spectroscopic probe source, can produce photoisomerisation. The initial measurement of the photo-isomerisation of 10^{-5}M Disperse Orange 1 using the 488 nm diode laser at 5 μW as a pump source, is shown in Figure 3.22. Laser pulses of 100 ms were used to promote photoisomerisation, between which measurements were taken within 30 ms by the spectrometer and recorded by the computer. It can be seen that the photoisomerisation was successful through the reduction in the absorption peak, which corresponds to the *trans* isomer. There is, however, very little data resolution between the initial spectrum, the solution measured from the dark, to the measured photo-stationary state, which is reached within 3 pulses. Reduction in the pump laser power had little effect and so the photoisomerisation was being induced by the broadband xenon lamp, which was providing ~1 μW of power to the sample.

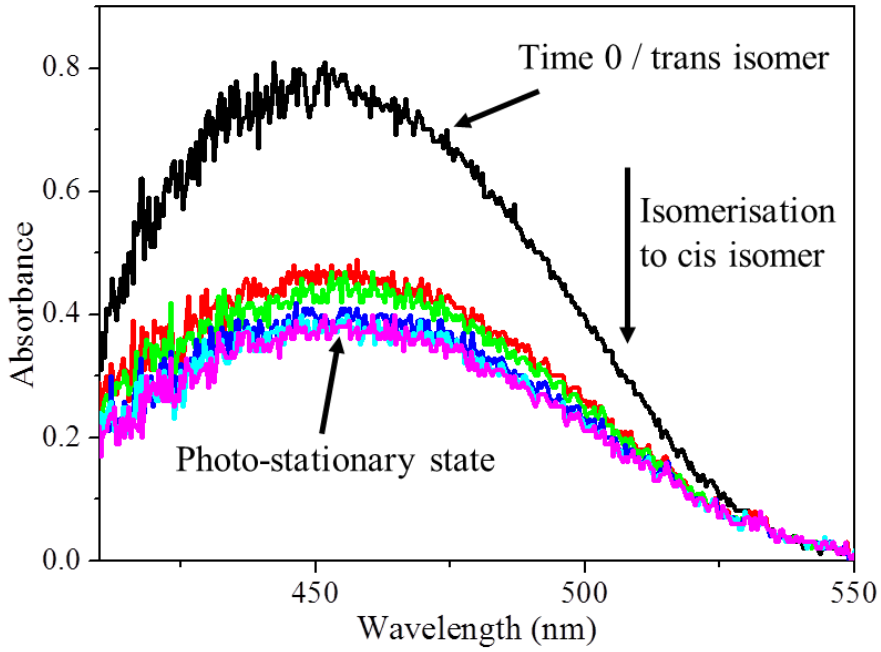

Figure 3.22: Photo-isomerisation of 10^{-5} M Disperse Orange 1 in pentane using a 488 nm laser at 5 µW, each curve represents the absorbance after 100 ms exposure intervals in the HC–PCF.

To investigate the effect the xenon lamp on the isomerisation process further a set of experiments were performed without the pump laser present. Also, to try to reduce the effect of the lamp a 550 nm short-pass filter was placed between the lamp and the sample fibre, this ensured that only the light covering the desired spectrum was incident upon the sample. The raw spectral output of the xenon lamp and the output after the filter was applied are shown in Figure 3.23. The same measurement sample as shown in Figure 3.22 is shown in Figure 3.24 using just the xenon lamp, at the same power, with the filter in place, taking measurements every 50 ms. It can be seen that the xenon lamp itself is causing a large amount of photoisomerisation to occur over a short timescale.

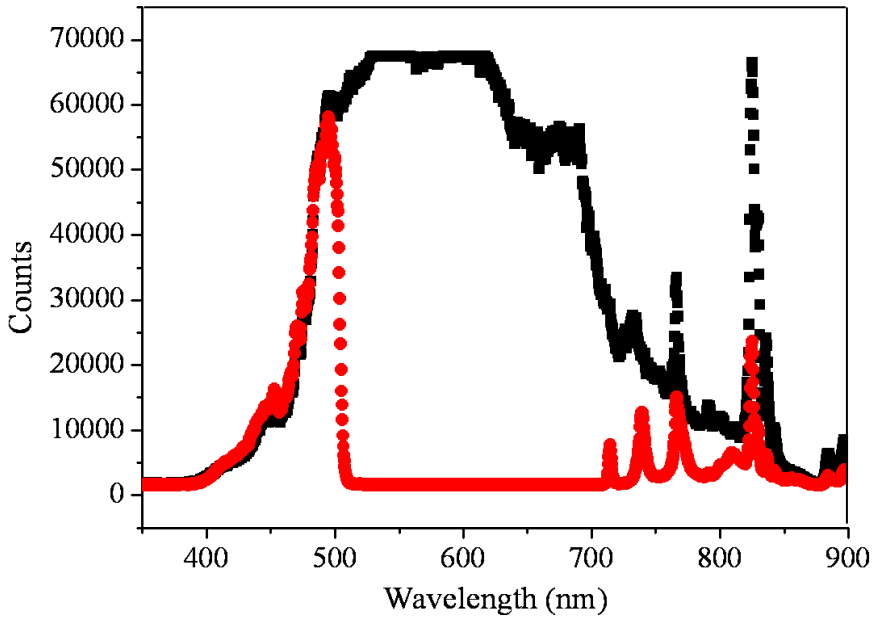

Figure 3.23: Spectral output of the xenon lamp source before (black) and after (red) a 550 nm short-pass filter

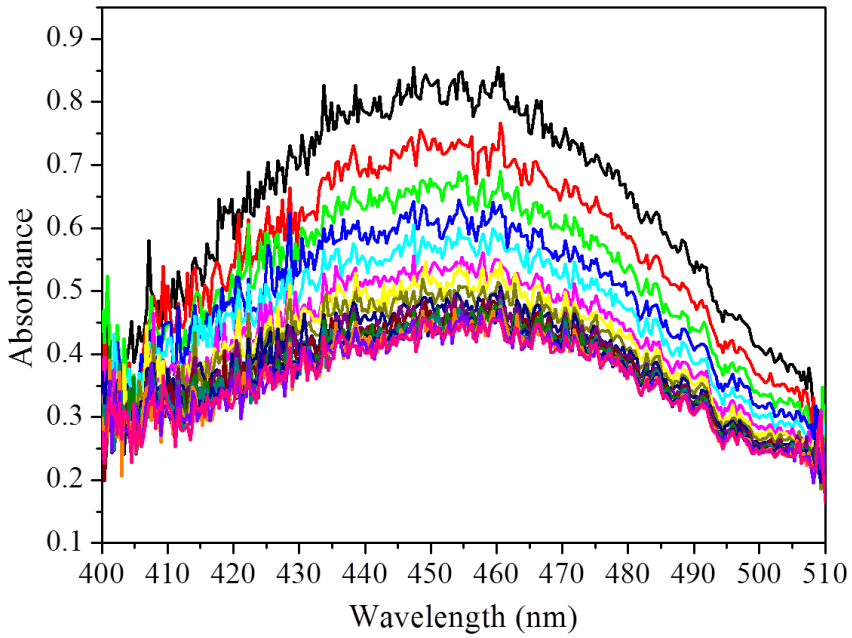

Figure 3.24: Change in absorption spectrum of Disperse Orange 1 under irradiation from 1 μW from the xenon lamp, measured every 50 ms.

The effect of the xenon lamp on the photoisomerisation of Disperse Orange 1 is shown in Figure 3.25 for several power levels along with a measurement at the lowest power without the 550 nm filter in place. As the power is increased the rate at

which the system reaches the PSS is also increased as expected. A saturation level is reached at approximately 1 µW of lamp power where no further reduction in the time to PSS is observed. From the measurement without the 550 nm filter it can be seen that the initial assumption that the excess bandwidth of the lamp would increase the photo-isomerisation was incorrect. This can be explained by the presence of a relatively small *cis* isomer absorption band at longer wavelengths. Absorption by the *cis* isomer in this region aids the reverse photoisomerisation process and depletes the number of *cis* molecules. The observed aggregate effect of the lamp is therefore reduced.

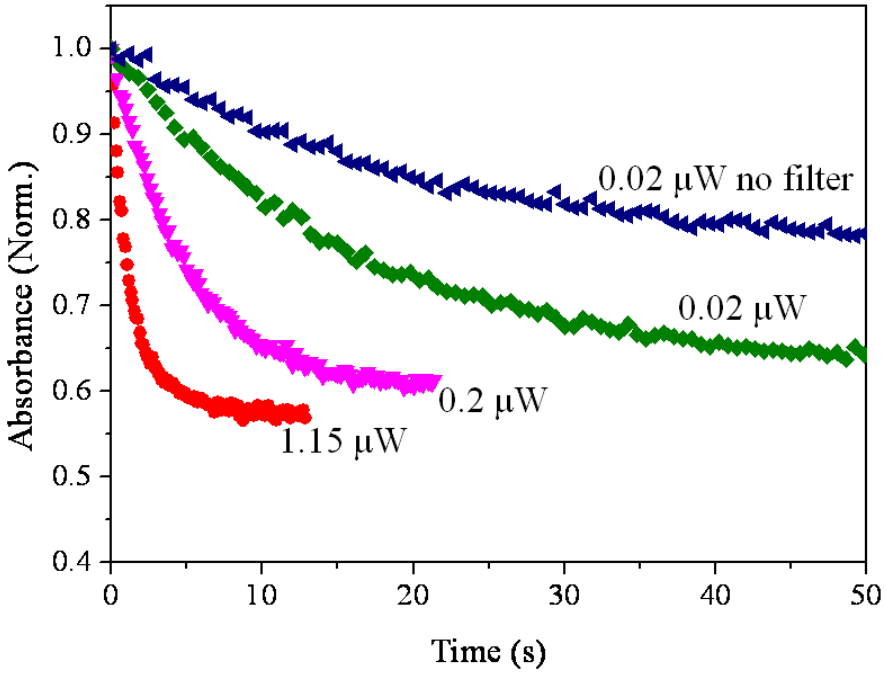

Figure 3.25: The effect of excitation power on the time taken to reach the photo-stationary state for Disperse Orange 1 in cyclohexane at 10^{-6} M, in a 30-cm kagomé fibre. Absorbance at 470 nm as a function of time for excitation powers of 1.15 µW, 0.2 µW and 0.02 µW with a 550nm short pass filter in place and 0.02 µW with no filter on the broadband source.

The time taken to reach the PSS is plotted as a function of incident power in Figure 3.26, also shown for comparison is the result of a conventional cuvette measurement on the same solution. Almost three orders of magnitude more power was needed to reach the PSS in a comparable time in the cuvette: irradiation with 100 µW produced the PSS in 20 s, compared with < 0.1 µW in the PCF. Although the total power entering the fibre is three orders of magnitude lower, the irradiance in the 19 µm

fibre core is approximately three orders of magnitude higher, 60 mW cm^{-2}, compared to ~50 μW cm^{-2} for the cuvette measurement.

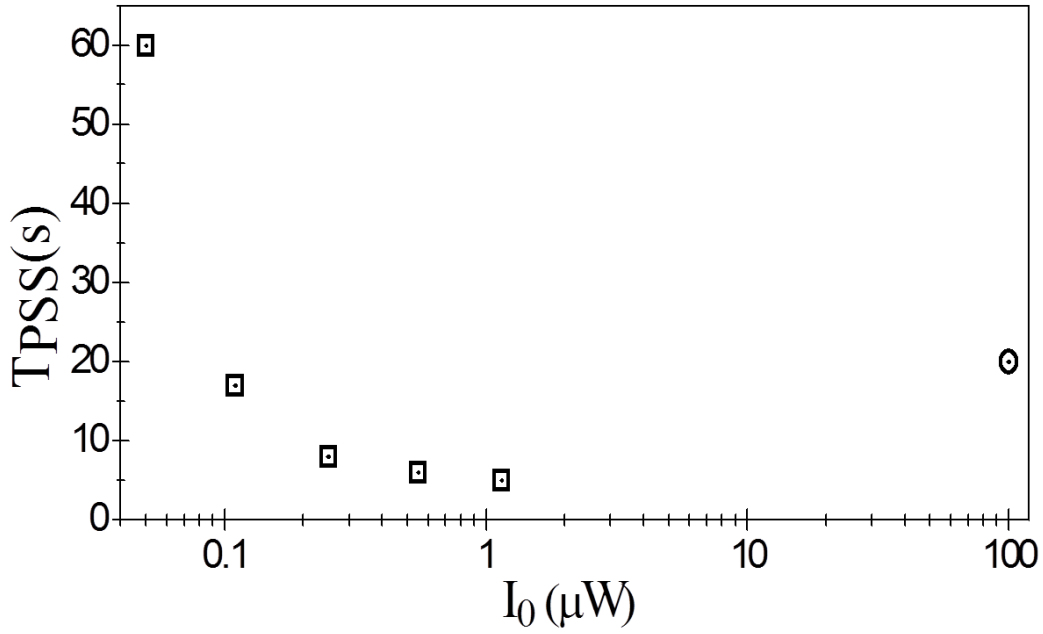

.

Figure 3.26: Time to photo-stationary state versus excitation power (solid line is a guide only). The isolated point is the value for an equivalent cuvette measurement. Peak power in the fibre using 0.02 μW input power is ~0.06 W cm^{-2} versus ~50 μ W cm^{-2} in a 1cm cuvette.

Using the xenon lamp as both pump and probe, the photoisomerisation of Disperse Orange 1 was monitored on the millisecond timescale by recording the complete absorption spectrum, with an integration time of 10 ms, at 100 ms intervals. The measured temporal evolution of the absorbance at 470 nm is shown in Figure 3.27, together with the fitted kinetic function. Whilst this offers an attractively simple method of simultaneously exciting and probing the photoswitching process, the use of polychromatic excitation hinders modelling of the kinetics because of the need to take account of the wavelength-dependence of the irradiation intensity and the absorption cross-sections of the two isomers. In the present case, an approximate model was used in which the total incident intensity and spectrally averaged cross-sections were used. This gave an estimate of 0.23 for the *trans*-to-*cis* photoisomerisation quantum yield of Disperse Orange 1. To our knowledge this is the first reported measurement of this parameter.

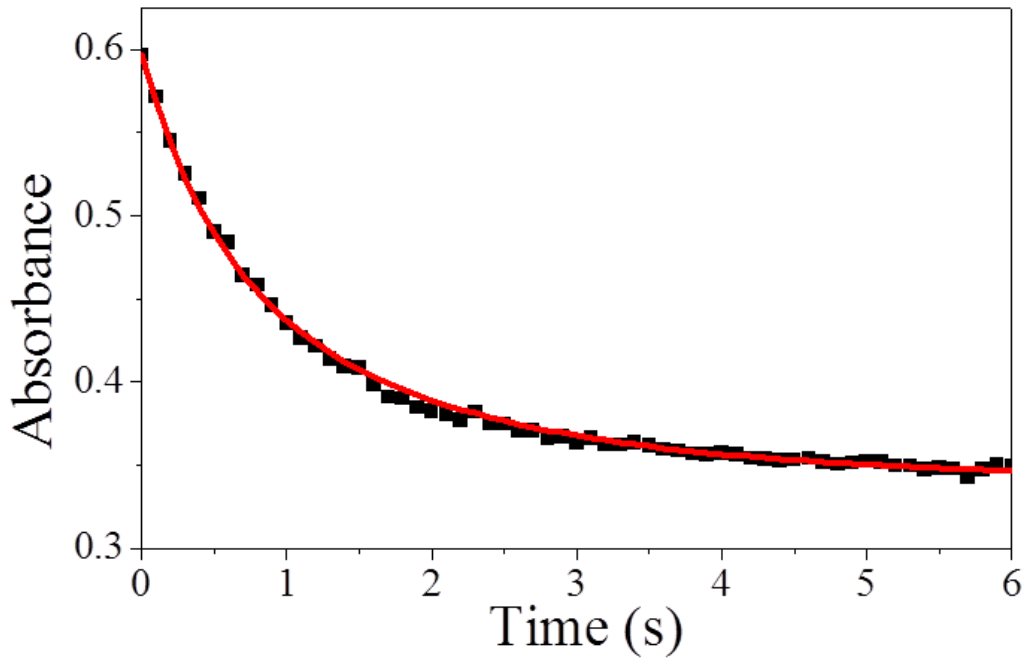

Figure 3.27: The photoisomerisation kinetics of Disperse Orange 1 in toluene at a concentration of 2 μM. The experimentally measured temporal evolution of the absorbance at 470nm (■), using the broadband output of the xenon lamp as both pump and probe, and the fitted model function (—).

All further measurements were performed using 0.02 μW of xenon lamp power, with no filter, removing its influence on the results and facilitating quantitative kinetic modelling using a monochromatic pump source. The negative side effect of this is the minimum integration time for the spectrometer at these power levels was 500 ms, reducing the number of spectra that could be recorded in a set time. This limitation could be lifted with a more sensitive spectrometer, or by monitoring only a small frequency range once the validity of the chemical process has been determined. This would allow for higher power to be used whilst maintaining low overall exposure to the sample from the probe.

The results of measurement of the photoisomerisation kinetics of Disperse Red 1 in toluene using the 488 nm diode laser as pump are shown in Figure 3.28, with the fitted temporal evolution at 488 nm in Figure 3.29. Exposure of the sample to the 4 μW, 488 nm, beam for 300 ms was followed by acquisition of the absorption spectrum over a 500 ms interval, with the pump beam blocked, giving a total of 800 ms for each pump–probe measurement. Excitation at a single wavelength makes

determination of the photoisomerisation quantum yield straightforward and a value of 0.19 was obtained for the *trans* to *cis* isomerisation of Disperse Red 1. This is in good agreement with the value of 0.2 which was reported recently for Disperse Red1 deposited as a solid film (in which thermal isomerisation was inhibited)[126].

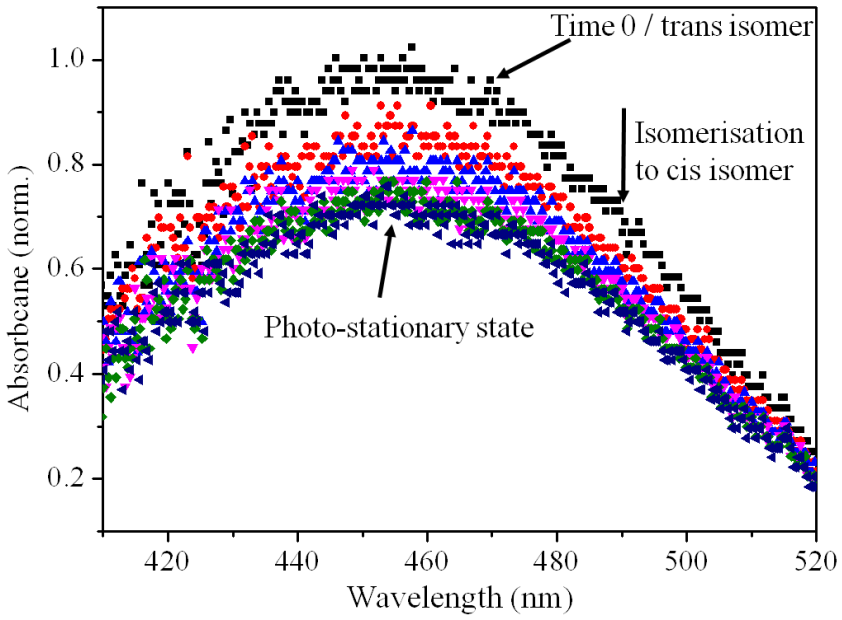

Figure 3.28: Photoisomerisation of Disperse Red 1 in toluene at $5x10^{-6}$ M using a 488nm pump laser at 4 μW for 300 ms intervals. Integration time 500 ms..

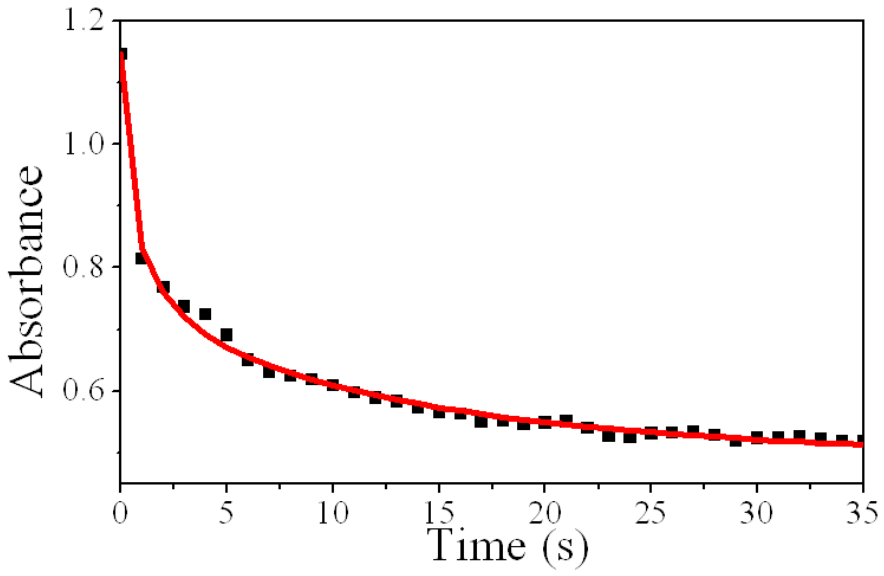

Figure 3.29: The photoisomerisation kinetics of Disperse Red 1 in toluene at 5 μM. The experimentally measured temporal evolution of the absorbance at 488nm (■), using the diode laser as pump and the xenon lamp as probe, and the fitted model function (—).

Final measurements were made on Disperse Red 1 at $5x10^{-6}$ M in pentane to allow for a measurement where the kagomé fibre was guiding through its designed mechanism as discussed in chapter 2.2. Due to the very low solubility of the dye problems were encountered with the dye adhering to the fibre wall and syringe filter as described previously, the sample therefore had to be flushed through the fibre for 1 hr at 1.5 mL h^{-1} or $1x10^{4}$ times the fibre volume before a stable maximum absorbance value of was reached.

The temporal evolution of the absorbance, for Disperse Orange 1 in three solvents, toluene, cyclohexane and pentane, during the thermal isomerisation process is shown in Figure 3.30. The lower final absorbance value for pentane is due to the limited sample concentration that could be produced. The rate constants obtained, together with those measured for Disperse Red 1, are given in Table 4. Values reported from previous conventional measurements (where available) are also presented in Table 4, for comparison.

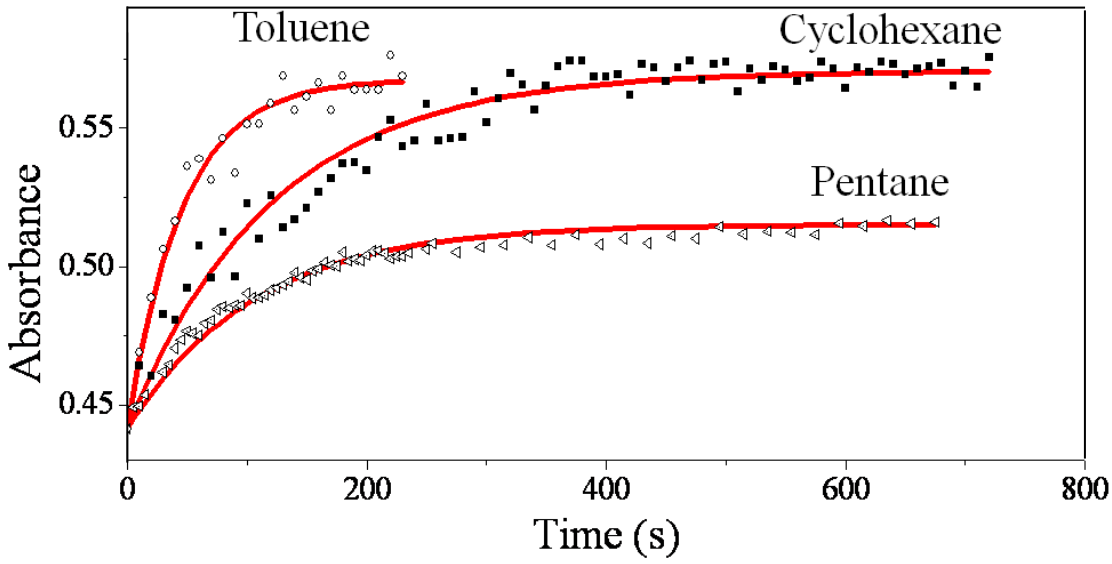

Figure 3.30: Kinetics of the thermal isomerisation of *cis*-Disperse Orange 1 in toluene, cyclohexane and pentane at room temperature. The temporal evolution of the absorbance at 470 nm, measured in the absence of pump irradiation, following attainment of the PSS. Experimental data are shown as points and the fitted theoretical functions as solid lines.

The rate of thermal relaxation from the *trans* to *cis* isomer is seen to reduce in line with reducing solvent polarity. This agrees with studies that have been carried out on this and similar push–pull azo–benzene based systems where the relaxation

mechanism is aided by more polar solvents as discussed in chapter 2.2.

Dye	Solvent	k_Δ / $10^{-3}s^{-1}$	
		This Study	**Literature**
Disperse Red 1	Toluene	30	35[66], 28[114]
	Cyclohexane	1	N/A
	Pentane	0.6	N/A
Disperse Orange 1	Toluene	20	N/A
	Cyclohexane	0.8	0.9[119], 0.6[118], 0.8[117]

Table 4: The thermal isomerisation rate constant, k_Δ, for DR1 and DO1 in various solvents. Values obtained in the present study are compared with those from previous, conventional measurements.

The values obtained in the present experiments are in very good agreement with those from previous, conventional measurements. This demonstrates that the isomerisation process is not perturbed by containment of the solution in the PCF and confirms that the sample volume that is probed is the bulk solution, not surface-bound molecules. The low solubility of push–pull azobenzenes in non-polar solvents is problematic for cuvette-based measurements and we are not aware of any previous studies in very low polarity solvents, such as pentane; the solubility of DR1 in pentane is only 1.3 μM. This is achieved whilst only requiring 90 nL of sample or ~$4.5x10^{-12}$ mol of dye for the measurement. Whilst in practice greatly more than this is required, even when the dye is in a good solvent, due to dead volume involved in piping solution to the liquid cell from the syringe, and in flushing through the fibre to negate surface effects, both of these issues should be solvable. Direct injection into the sample cell would reduce dead volume down to the ~5 μL of the cell itself or alternate methods such as injection through a hole drilled in the side of the fibre would reduce the dead volume to zero using techniques such as those discussed in section 2.1.

3.5. Conclusions

Hollow-core PCF is a highly effective optofluidic system for the measurement of photochemical kinetics by absorption spectroscopy. The extrusion of sub-microlitre sample volumes over path-lengths of tens of centimetres enables highly sensitive measurements on sub-picomole samples. The power of this methodology has been illustrated by its application to the reversible photoisomerisation of two push–pull azobenzenes. Rapid thermal isomerisation in polar solvents and low solubility in non–polar solvents inhibit conventional cuvette–based measurements of the isomerisation kinetics of this technologically important class of azobenzenes.

The work exploited the near–perfect overlap of the pump and probe light with the sample, contained within the hollow core of PCF, to measure the *trans–cis* photoisomerisation quantum yield in solution, at room temperature. The very few previous conventional measurements have used low temperature or solid samples to inhibit thermal isomerisation.

Rate constants measured for the thermal *cis–trans* isomerisation of Disperse Red 1 in toluene and Disperse Orange 1 in cyclohexane are in excellent agreement with previous cuvette-based measurements. The 30 cm path-length of the PCF enabled the first measurement of the thermal rate constant of a push–pull azobenzene in a highly nonpolar solvent, pentane, in which the solubility is very low. A concentration of 1 μM was used, equivalent to less than 100 femtomoles of sample. Experimental values of thermal isomerisation rate constants in non-interacting solvents are particularly valuable for validating quantum chemical calculations, which typically consider isolated molecules in the gas phase. Recent calculations[127] predict rate constants in the region of 5–10 s^{-1} for push–pull azobenzenes more than an order of magnitude greater than the value measured here for Disperse Red 1 in pentane.

The incorporation of PCFs as photochemical reactors in lab-on-a-chip devices could revolutionise high-throughput screening of photoactive targets and the application of photochemistry based assays in micro-total-analysis systems. The development of an all-fibre optofluidic photoreactor can be envisaged, in which fibre lasers and/or PCF-based super-continuum sources, as pump and probe, are integrated with the sample-containing PCF.

4. Fluorescence Spectroscopy in PCF

4.1. Introduction

Fluorescence spectroscopy has become widely used across many fields in the physical and biological sciences, with applications ranging from molecular labelling and energy–transfer techniques[78] to allow angstrom–level distance measurements along with sensitivity down to the ultimate level of single molecules[128]. However, the measurement of fluorescence emitted by fluorophores at low concentrations, free in bulk solution, or on surfaces remains a challenge.

The use of PCF, for both excitation of fluorophores and collection of the emitted fluorescence, provides an ideal approach for monitoring fluorescence properties of molecules in free solution. Also, measurements at very low concentrations can be achieved due to the long path lengths for excitation. The benefit of this type of measurement over particle trapping measurements, which are by definition far more sensitive, is that the molecules can be studied in more natural or diverse environments – environments which can be very well controlled through solution injection, temperature and optical confinement. Furthermore, the tight confinement of light within a PCF should make it an ideal environment in which to carry out two-photon excitation (TPE) experiments, as high powers density can be maintained over long distances through a sample, something which is very hard to achieve in conventional experimental systems.

4.1.1. Using PCF to Collect Fluorescence

Early reports of work using PCF for fluorescence measurements described using the PCF simply as a light delivery and collection device to a sample contained in a more conventional cell, such as a cuvette[127,128,129]. A schematic of how an optical fibre is used in this manner is shown in Figure 4.1

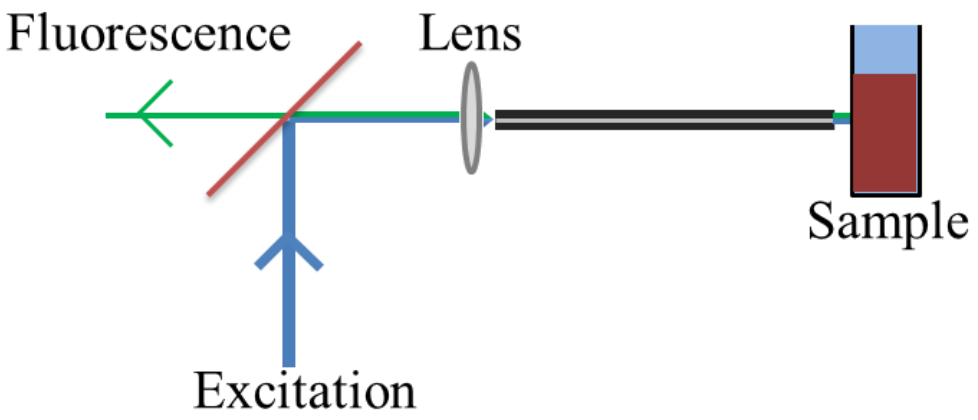

Figure 4.1: Schematic of an optical fibre being used as a method for delivering excitation light and simultaneously collecting emitted fluorescence from a sample.

The light transport properties of the fibre allows light to be guided easily to the sample and utilizing the higher NA of PCF over conventional fibres allows for relatively efficient collection of fluorescence into the fibre and to a detector. If the spatial–mode properties of the excitation light are not of concern, large–core multi–mode PCF can be used, further increasing collection efficiency [129]. Several improvements over such a single fibre system have been made leading to applications in several areas. Ma et al[130] show the use of two or more fibres in a bundle, one conventional fibre to excite fluorescence and one or more PCF to collect the emission, greatly enhanced efficiency. Furthermore, the group showed an additional benefit from the addition of a small glass tip to the fibres which allowed a large reduction in the distance the probe could be placed from the sample (the dead zone).

The use of a PCF in this regime for measuring fluorescence lifetimes was shown by Fujii *et al.* who used a PCF spliced to a conventional fibre to excite temperature–

dependent fluorescence from quantum dots (QD) and collect the emission through the same fibre construct. The fluorescence lifetimes were not perturbed, allowing for accurate temperature measurements from within the sample[131].

The use of this method utilising more exotic types of PCF was shown by Vengalathunadakal *et al.*[132], who studied the collection efficiency of a HC–PCF and a double clad PCF. With the HC–PCF, the majority of fluorescence is collected by the fibre core. The small size and pitch of the cladding holes, however, gives them a higher NA than the core. This allows for further collection of light within the cladding, increasing the total collection efficiency of the fibre. With a double clad fibre, the single-mode central core allows for excitation light to be transmitted to the sample and collection of emission is made by both the inner core and its cladding which is surrounded by a further cladding region, producing a high NA second core region. Due to the very high NA that can be achieved in the index guiding inner core of the double clad fibre, typically twice that of a conventional fibre, the collection efficiency is highest for this fibre design. A schematic of the collection mechanism for both types of fibre is shown in Figure 4.2 highlighting the coupling into the HC–PCF cladding. The use of the two fibre types was proposed as a means for a highly sensitive dual mode probe for in-vivo studies when combined with a micro camera.

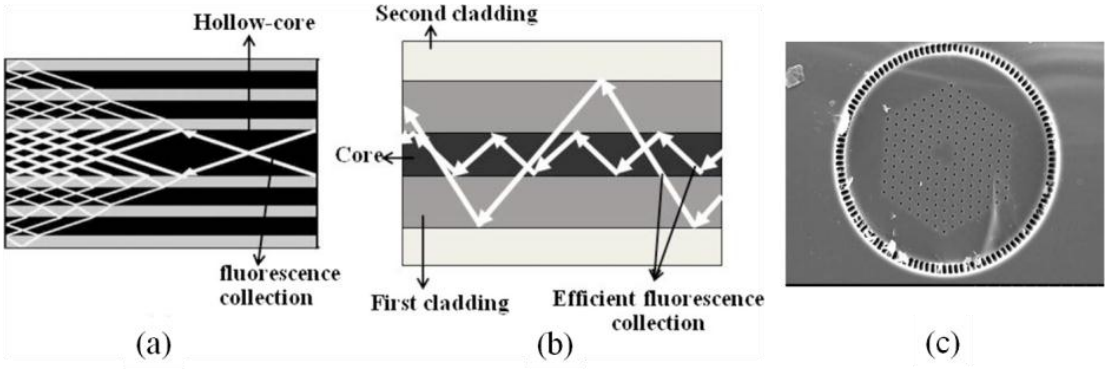

Figure 4.2: (a) Florescence collection in a HC–PCF, (b) fluorescence collection in a double–clad PCF, (c) SEM of a double–clad PCF[130].

A similar double–clad PCF has been used for 2–photon excitation measurements by utilising the tightly confined inner core to provide high power single mode excitation light to excite two–photon induced fluorescence from biomolecules in a sample[133].

The fluorescence was collected using the high NA multimode inner cladding region. A setup like this has been used as means for providing excitation and collection of fluorescence for highly sensitive two photon fluorescence correlation spectroscopy[134]. Finally, the use of double−clad PCF has been shown to maintain the fluorescence decay profile and lifetime following TPE, allowing these parameters to be measured from deeper within a tissue sample than is possible using OPE[135]. Whilst these types of measurements do not take advantage of the small volumes and long path lengths offered by PCF for taking measurements within the fibres, they do offer insight into the ideal fibre design for fluorescence detection.

4.1.2. Exciting Fluorescence within PCF

To take full advantage of the properties made available through the use of PCF, such as small internal volume and long path lengths, a much more efficient way to excite and detect fluorescence is from within the fibre itself. There are two regimes in which this can be accomplished, firstly by using a solid core fibre surrounded by air holes, which can be filled with sample, in which case excitation of the sample is through the evanescent field of the pump light and emitted fluorescence is coupled back into the core. Secondly, a hollow core fibre can be used, as in the photochemical measurements reported in this thesis, where both the excitation light and the collected fluorescence pass through the solution phase sample within the fibre core. Both regimes were demonstrated by Konorov *et al.*[136] using a HC−PCF, where the refractive index of the fluid was varied relative to the silica fibre construct, changing the guidance properties of the fibre. When using a low refractive −index sample, light was guided in the silica construct allowing evanescent excitation of fluorescence. Using a higher refractive index sample, light is guided in the solution allowing for bulk excitation. This showed the potential of PCF as a vessel for the excitation and collection of fluorescence from within PCF. However, as the index of the sample was used to change guidance properties of the fibre this meant guidance was always by TIR, not by a band gap (BG) mechanism, and, due to the relatively small index contrast, high losses would be incurred. A similar measurement was made by Jensen *et al.*[137] using a PCF in the evanescent sensing regime, illuminating the whole fibre face, this technique gave a detection sensitivity of ~10 nM. The

non-uniform sample illumination used is shown in Figure 4.3 making knowledge of the sample exposure to pump light difficult.

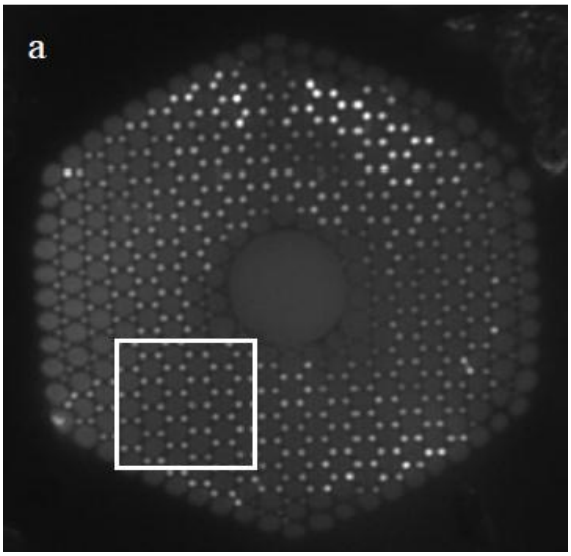

Figure 4.3: Light propagated through a PCF illuminated over the entire end face[135].

Smolka *et al.*[138] have shown the use of a HC–PCF for efficient bulk solution fluorescence excitation and collection from within the fibre core. In this measurement, the cladding holes of the 10 cm fibre were sealed by laser splicing so that only the fibre core was filled by capillary action. This, as in the Konorov experiments, produced a higher refractive index core than the cladding and therefore the fibre guided by TIR not by BG, reducing efficiency. The same study used a SC-PCF to examine evanescent wave excitation and detection and found limits of detection for the Rhodamine 6G fluorophore of 10^{-6} M in the SC-PCF and 10^{-10} M in the HC–PCF. The greatly increased sensitivity in the HC–PCF is attributed to the near 100% light to sample overlap compared to ~1% in the SC-PCF. This is the closest approach to a true in-fibre bulk fluorescence experiment that has been reported to our knowledge.

Extensive work has been also been undertaken using short lengths of PCF, where the inner core surface is selectively coated with a sample through capillary action and drying[139,140,141,142]. For example Larrion *et al.*[143] coated the cladding holes of a SC-PCF with layers of quantum dots (QDs) allowing the construction of a robust miniature temperature sensor through the temperature-dependent optical absorbance of the QDs. Rutowska *et al.*[144] used a HC–PCF where the core was coated with a

hydrogel to immobilize and detect labelled–DNA through efficient fluorescence detection.

One of the features of performing fluorescence measurements over long path lengths such as those available by using PCF is the greatly increased probability for re-absorption to occur, distorting the observed fluorescence spectrum. This was demonstrated by Smolka *et al.*[145] where, at 10^{-5} M, the peak of the Rhodamine 6G emission spectrum was red-shifted shifted by 10 nm through increasing the path length from 6 cm to 12 cm. This phenomenon is, generally, not of concern in PCF measurements due to the greatly reduced sample concentration that can be used in these systems.

The work presented here explores the use of a kagomé type HC–PCF such as used for the photochemistry measurements (chapter 3), and a suspended core "Mercedes" fibre. The index guiding silica core of the Mercedes fibre enables good guidance over the entire visible region, with a wavelength–dependent evanescent field interacting with the sample.. SEM images of the fibres used are shown in Figure 4.4.

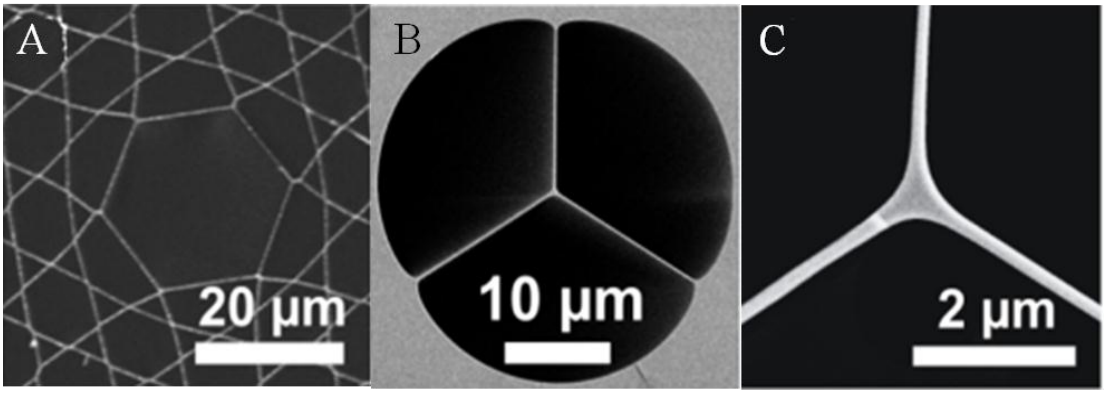

Figure 4.4: (A) SEM of the kagomé HC–PCF with a 19 µm core. (B + C) SEM images of the suspended core PCF showing the whole fibre and a close up of the 500nm core region.

The hollow–core fibre has a core volume of 2.8 nL cm^{-1} and gives a measurement of the bulk solution with very low intensity near the fibre surface as the guided mode is Gaussian with maximum intensity at the centre of the core. There is very good overlap with the sample with ~98% of the molecules in the core being excited[136]. In contrast the solid core suspended fibre contains ~9 nL cm^{-1} in the cladding region. However, the sample penetration of the excitation light is only through the

evanescent field around the core. The penetration depth of this field is wavelength-dependent but typically extends 10's of nm into the sample and therefore the probed volume is only ~0.5 nL cm^{-1} and is confined to fluorophores in very close proximity to, or on, the surface of the fibre core.

Using the Fluorescein fluorophore, shown in Figure 4.5, this work examines the limits of detection using both fibre types, utilising long path lengths of ~30 cm. The fluorophore was chosen due to its relatively high fluorescence quantum yield and because it is the basis for a wide range of fluorophores used extensively as fluorescent labels[146]. As discussed in chapter 2.3.4, due to acid functional groups the emission spectrum and quantum yield of the fluorophore is pH dependent with the emission spectrum shifting to longer wavelength with reduced pH. The pH of the solutions were kept constant (~pH 7) throughout the experiments allowing comparisons to be made.

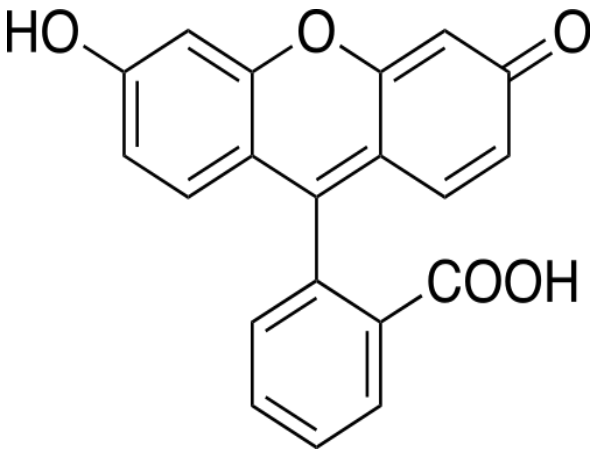

Figure 4.5:The structure of the Fluorescein fluorophore.

In contrast to previous studies discussed above the HC–PCF is completely filled with sample and is designed to maintain its guidance mechanism when filled, as discussed in chapter 2.1.7, permitting low loss, uniform excitation over the whole path length. The fibres were mounted and filled using the same sample cells as for the photochemistry work, therefore the same procedure for filling of the fibres was performed.

The measurement of the fluorescence lifetime of the Rhodamine B fluorophore in both types of fibre is reported. The fluorophore structure is shown in Figure 4.6.

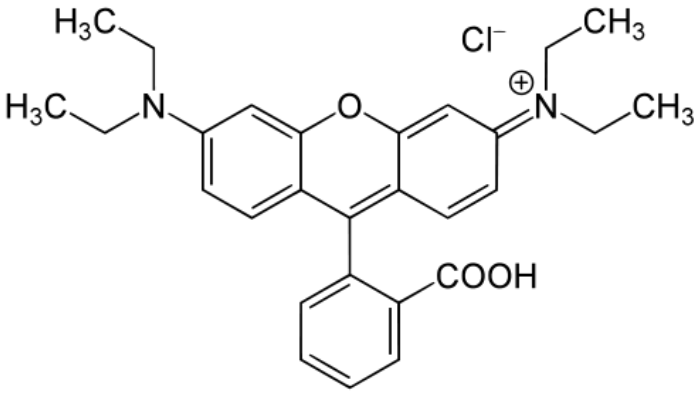

Figure 4.6: The structure of the Rhodamine B fluorophore.

As discussed in section 2.3.5, Rhodamine B has a temperature–dependent lifetime due to non-radiative decay facilitated by rotation of the diethyamino functional groups. A decrease in temperature reduces rotation of these groups, reducing the rate of non-radiative decay and therefore increasing the observed fluorescence lifetime. Rhodamine B can therefore be used as an in-fibre temperature sensor, allowing effects such as heating, caused by pump lasers, to be assessed.

When the fluorophore is immobilised on a silica surface the rotation of the diethyamino groups is completely restricted, removing this non-radiative decay pathway, resulting in a longer, fixed, fluorescence lifetime. This property can be used as an indicator for the fluorophore location in relation to a fibres silica cladding structure. With a HC–PCF measurement, excited fluorophores are in bulk solution giving a measure of the free molecule lifetime, whilst in a suspended core fibre excitation occurs on fluorophores immobilised on or in very close proximity to the silica surface.

TPE measurements in conventional systems are usually limited to very small sample volumes and path lengths due to the need for very high photon flux, requiring the focusing of a pulsed Ti-Sapphire laser into a small region, typically a few femtolitres of sample, within a larger bulk solution. Typical concentrations required are also several orders of magnitude higher than for OPE experiments, usually being in the 10^{-3}–10^{-5}M range[82,83,147]. PCF has been shown by others to be effective in guiding the required powers for TPE excitation to a sample and for exciting TPE induced fluorescence from within doped single crystal fibres[148]. The next step is to perform

TPE on a bulk solution within a PCF. This should allow the sample to be exposed to the high intensity excitation over, potentially, very long path lengths, limited only by the broadening of laser pulses due to dispersion through the fibre, which reduces peak power density. As the whole sample is excited, this system should provide a highly efficient modality for performing TPE experiments. Presented are initial results of TPE of Fluorescein, chosen for its relatively high two photon absorbance cross-section and to allow comparison with the OPE experiments, excited within a HC kagomé PCF. The use of PCF as a TPE system opens up the possibility for studying many systems that were previously technically challenging, for example the study of the two-photon excited photochemistry of drugs used for photodynamic therapy in cancer research[149] which are typically required to be excited in the longer wavelength regions of the spectrum to allow for tissue penetration.

4.2. Experimental Methods

4.2.1. Materials

The Fluorescein and Rhodamine B fluorophores were obtained from Sigma Aldrich and the solvent used was HPLC grade water from Fisher Scientific.

4.2.2. Single Photon Excitation Measurements

Initial measurements were made with the goal of finding the detection limit of fluorescence using one photon excitation (OPE) with the PCF acting as a sample chamber for excitation of the fluorophore and detection of the emitted fluorescence.

The experimental setup used for the measurement of fluorescence is similar to that which was used for the photochemistry experiments (chapter 3) and is shown in Figure 4.7. A 470 nm pico–second (~50 ps pulses, rep rate 50 MHz) pulsed diode laser was used as the excitation source. This source was found to emit a faint green "glow", along with the principal laser line. This was removed using a 470 nm notch filter to prevent interference with the fluorescence signal; the filter was introduced before the fibre in-coupling to remove any effect on the excitation process. After the fibre a 488 nm long pass filter was used to block the excitation light and isolate the fluorescence signal for detection.

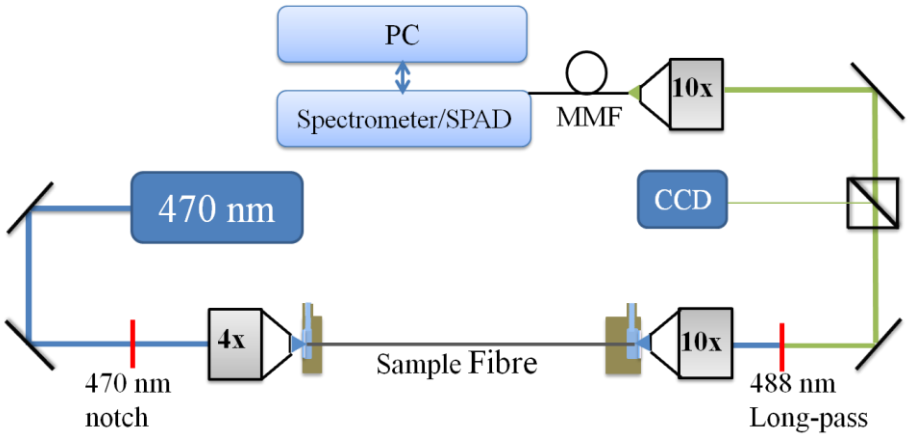

Figure 4.7: Schematic of the experimental setup used for measuring fluorescence excited by a 470 nm diode laser. A 470 nm notch filter insures only the laser line enters the fibre and a 488 nm long pass filter is used to remove the laser line at the output of the fibre to allow isolation of the fluorescence signal using a grating CCD spectrometer or a SPAD detector for lifetime measurements.

Fluorescence was detected and spectrally analysed by a grating spectrometer (Ocean Optics USB2000+) similar to the one used for the photochemistry experiments. A CCD camera was used to assist the alignment of the fibre in−coupling allowing the guided mode profile to be viewed. To ensure optimum coupling of light into the spectrometer, the path length between the fibre output objective and both the CCD and spectrometer were equal. In this way an in focus image on the CCD equates to optimal focus at the spectrometer. The out−coupling from the fibre is inherently wavelength-dependent due to increased dispersion by the lens as the wavelength is decreased. Therefore, to maximise the collection of fluorescence the out-coupling should be optimised for the peak emitted wavelength, not that of the excitation light. However due to the relatively small Stokes shift of the Fluorescein fluorophore, around 30 nm, and the very low intensity of fluorescence signal, no such correction was made.

As discussed in section 4.1.2, two contrasting types of PCF (30 cm in length in each case) were employed, a HC kagomé PCF with a 19 µm core such that was used in the photochemistry experiments and a suspended-core "Mercedes" fibre, with a core diameter of 500 nm. Due to the small core diameter of the suspended core fibre, a 60x objective was required (a 4x objective was used for the HC fibre, shown in Figure 4.7) along with very thin (0.1 mm) glass windows on the sample cells to allow efficient in and out coupling.

The fibres were initially filled with pure solvent at a rate of 1 mL hr^{-1} for 45 min and 30 min for the HC and suspended core fibres respectively to ensure all of the cladding holes were completely filled (in accordance to the calculations shown in chapter 2.1.6.1). Following this procedure, samples were introduced at the same pump rate for 15 min allowing the core of the HC fibre to be filled with sample and the cladding of the suspended core. The filling times for the samples are shorter than those for the initial fibre filling as, providing care is taken not to introduce bubbles, only the solution in the larger core region has to be replaced. Subsequent sample introduction could be made using the same 15 min pump times.

Solutions were prepared by producing a stock aqueous Fluorescein solution at 10^{-5} M. Dilutions were then performed and solutions left to equilibrate overnight before

being base adjusted to ~pH 7. Initial measurements using a reasonably concentrated solution of 10^{-8} M were completed showing the successful measurement of fluorescence using both fibre types using a pump intensity of ~100 µW. This pump intensity was found to cause significant photo−bleaching of the fluorophore and so was reduced for determination of the detection limit. Measurements were then conducted starting from 10^{-12} M solutions increasing in order of magnitude steps. For comparison a cuvette was excited using the same laser source with the collection of the emission made using an objective perpendicular to excitation using 10^{-5} M samples.

4.2.3. Fluorescence Lifetime Measurements

Fluorescence lifetime measurements were made using a Pico-quant TCSPAD (supplied by Edinburgh Instruments) system on the fluorophore Rhodamine B at a concentration of 10^{-8} M using the same setup as used for the detection limit measurements. The setup was initially aligned and optimised using the Ocean Optics spectrometer and CCD camera and then the detector was changed to the Pico-quant TCSPAD detector for measuring the lifetime of the fluorophore. Both fibre types were used to allow comparison between the lifetime of the molecule in bulk solution and when it is on, or very close to, a fibre surface. The data was fitted using F900 software (Edinburgh Instruments) to allow multi-exponential fitting and lifetime calculations.

4.2.4. Two-Photon Excitation Measurements

In order to perform the TPE measurements a femto−second pulsed Ti-Sapphire laser (Coherent, Mira 900), adjusted to 810 nm, providing ~100 fs pulses at a repetition rate of 80 MHz, was used to produce the high peak intensities needed. Due to the invisible nature of the 810 nm light produced by this laser system, making coupling of the light and alignment of the fibre output problematic, a second light source, a laser super-continuum source (nkt photonics SuperK, 400 nm – 2.4µm, maximum

total power ~4 W, variable rep rate), was co-aligned into the fibre. The super-continuum was used solely for alignment purposes. A schematic of the experimental setup is shown in Figure 4.8.

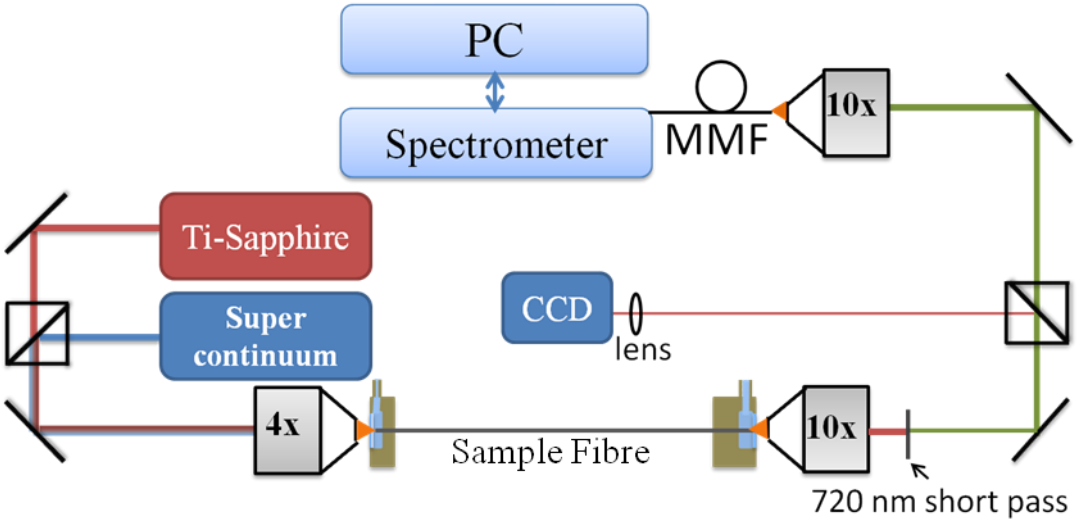

Figure 4.8: Schematic of the experimental setup used for two photon excited fluorescence. The excitation source was a femto second Ti-Sapphire laser and a super-continuum source ias used to aid alignment. The laser line was blocked by a 720 nm short pass filter after the output of the fibre.

This also allowed for the separate optimisation of the CCD camera for modal imaging of the 810 nm laser beam and the spectrometer in-coupling to 515 nm, the peak of the emission spectrum of the Fluorescein fluorophore. As discussed above, separate coupling into detector and camera is only required for the two-photon measurements due to the large difference in wavelength, ~300 nm, between excitation and emission light. Due to the wavelength difference the dispersion of the out-coupling objective after the fibre for the two wavelengths is significantly different and so separate focusing is required. A lens was added before the CCD camera to aid this optimisation. The laser line was blocked using a filter as before, here a 720 nm short pass filter was required. After initial measurements had been made to find the detection limit for TPE Fluorescein, in a similar manner as for the OPE measurements, a further experiment was performed to confirm that the detected fluorescence was indeed being induced by TPE. The fibre was filled with a 10^{-6} M Fluorescein solution and TPE fluorescence was excited using the full power of the laser, ~32 mW. This excitation power was then incrementally reduced allowing the dependence of fluorescence intensity on excitation power to be recorded.

4.3. Results and Discussion

4.3.1. Single Photon Fluorescence

Initial measurements were made on 10^{-8} M Fluorescein in both kagomé HC and suspended-core fibres to demonstrate the excitation and detection of fluorescence from within the fibre structures. The guided mode profiles of the excitation light for both fibres are shown in Figure 4.9, highlighting the different excitation regimes.

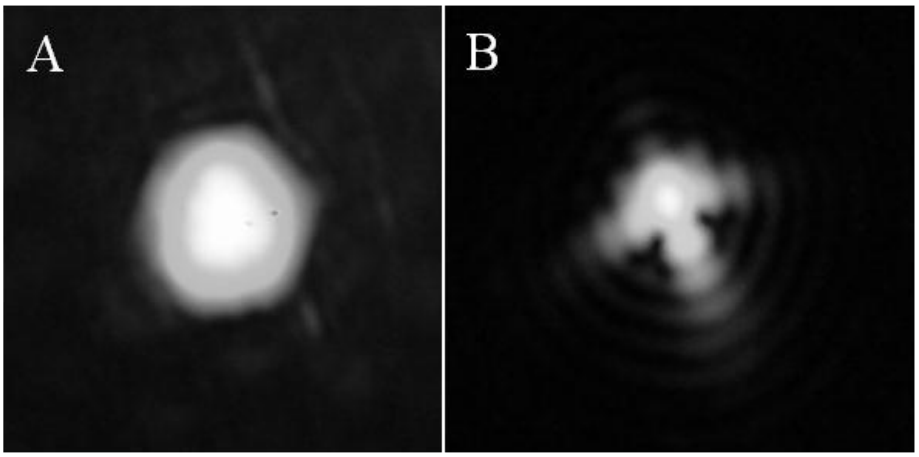

Figure 4.9: Guided modes of the 470 nm laser through (A) the kagomé hollow core fibre and (B) the suspended–core fibre. Note that, in the latter case, due to the very small core, a 60x objective is needed and the fibre tip was very close to the glass window of the sample cell, distorting the measured image.

The recorded spectra, shown in Figure 4.10, are in good agreement with the measured cuvette spectrum. Due to relatively low concentration of fluorophore, long path length and relatively high pump intensity of the 470 nm laser, at 100 μW, a significant amount of Stokes Raman scattering from the water solvent is detected, this can be seen as a perturbation in the recorded fluorescence spectrum. An isolated Raman band, recorded from the water only, is shown in the inset of the figure.

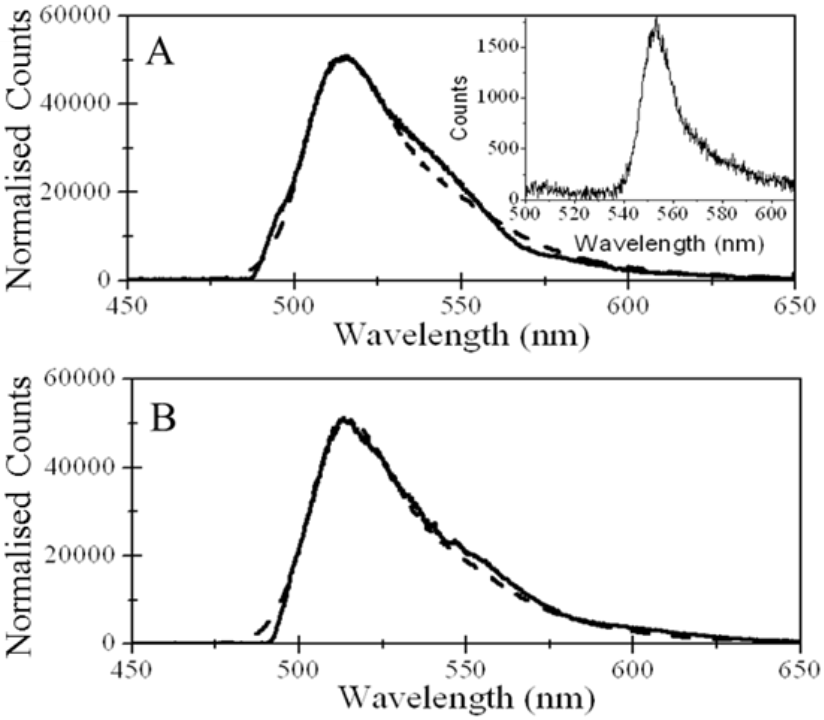

Figure 4.10: Fluorescence spectra recorded using a CCD spectrometer for Fluorescein at 10^{-8}M in water, excited at 470 nm, for both the hollow core (A) and suspended core (B) fibres compared with a cuvette measurement at 10^{-5}M. A spectrum of the water solvent, showing the Raman band, is presented in the inset.

Whilst the measurement of the fluorescence excited within the fibre was successful, it was noted that there was a rapid decrease in fluorescence intensity over time using this excitation power, due to photo-bleaching of the dye. Whilst observed in both fibre types the effect was less pronounced in the suspended core fibre, most likely due to diffusional replenishment of fluorophores near the core from the larger bulk solution. A set of spectra showing the effect of photo-bleaching over time on the signal from the Fluorescein fluorophore in the kagomé PCF is shown in Figure 4.11. Using a 30 ms integration time spectra are recorded after each integration. After 600 ms a reduction in intensity of 50% is observed. Complete photo–bleaching is not reached, probably due to the relative decrease in concentration (and therefore absorbance) and possible non-zero flow in the fibre replenishing the un-bleached fluorophore concentration.

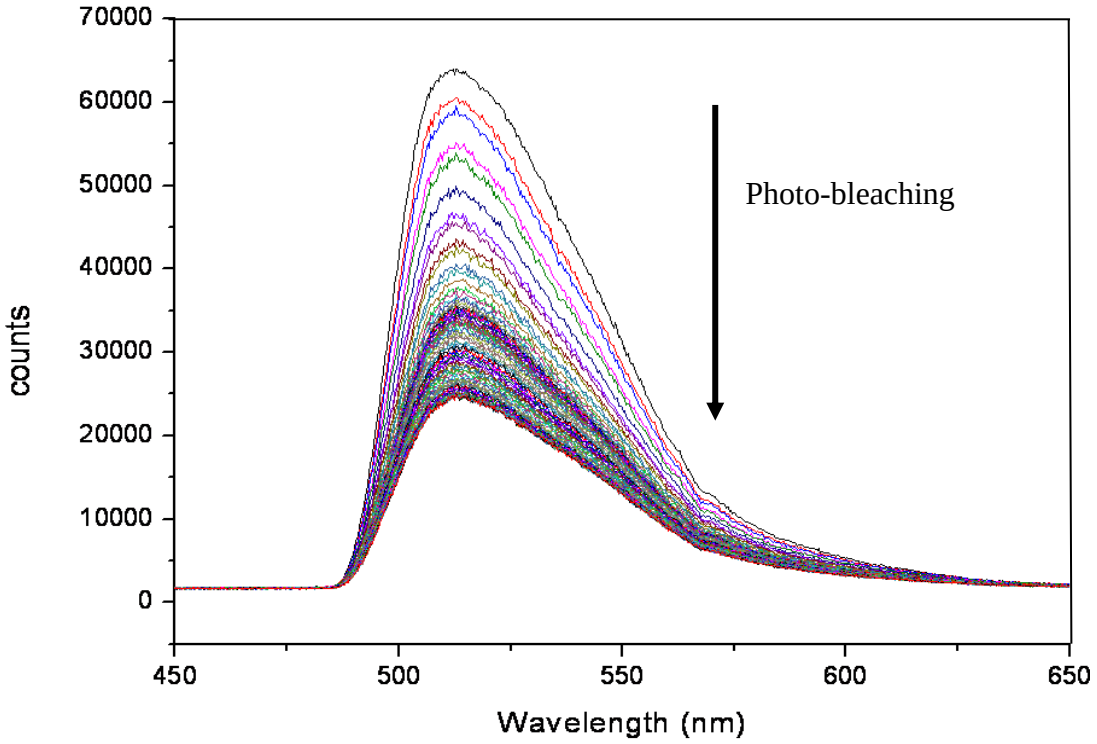

Figure 4.11: Spectra of 10^{-7} M Fluorescein in the kagomé PCF in water recorded sequentially over 600 ms, at 30 ms intervals (the spectrometer integration time). The large reduction in fluorescence observed is due to photo bleaching of the fluorophore.

Following these measurements the laser power was adjusted until maximum fluorescence was observed whilst minimising the rate of photo bleaching. This was found to be ~10 µW of CW pump power.

With the measurement system optimised the concentration of fluorophore was reduced to 10^{-12} M and then incrementally increased. The observed detection limit of Fluorescein in the HC kagomé fibre of $2x10^{-11}$ M, using the longest possible integration time of 15 s is shown in Figure 4.12. At this low concentration, the water Raman band is now the dominant feature in the spectrum relative to the greatly reduced fluorescence signal. Background subtraction using a pure water reference for the Raman peak allowed for successful removal of this Raman band recovering the correct spectrum for Fluorescein emission.

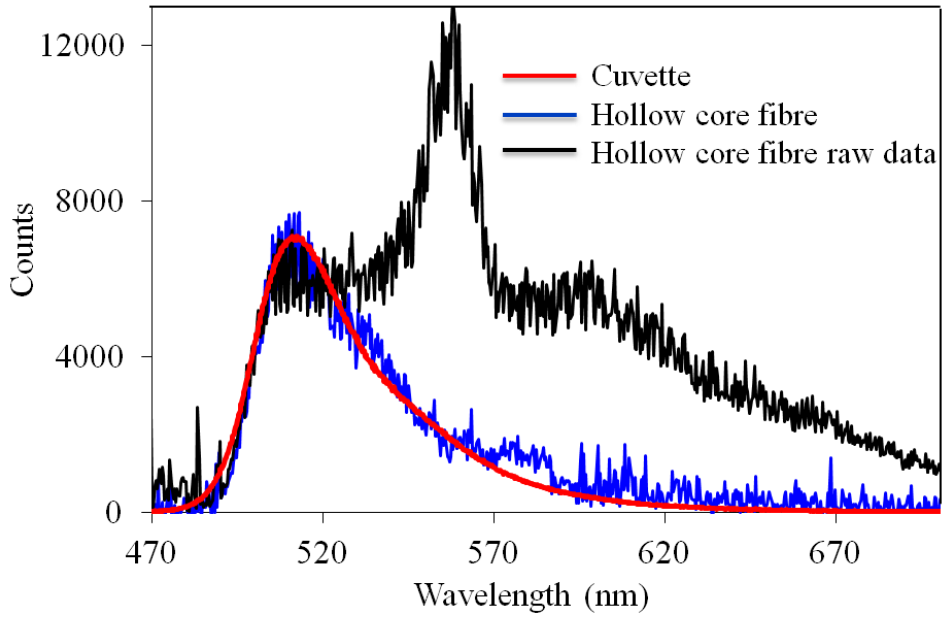

Figure 4.12: Emission spectrum of Fluorescein at $2x10^{-11}$ M in water in 30 cm of HC kagomé PCF using 15 s integration time. Raw data (black) shows the water Raman band becoming dominant, covering the fluorescence signal. After background subtraction (blue) the correct spectrum is obtained, as shown by reference to the cuvette measurement (red).

This concentration of Fluorescein in 30 cm of kagomé fibre, which contains ~90 nL of sample in the core region, equates to the excitation and detection of fluorescence from approximately 1.8×10^{-18} moles (1.8 attomoles) of dye or 10^6 molecules. Whilst this is impressively low, the detection limit for this fibre type can be extrapolated down to 10^{-11} M considering the good signal–to–noise ratio 6 in the current measurement. This is an order of magnitude more sensitive than previously reported in the literature[136]. The main limiting factor on the measurements was the noise induced by increasing integration time, to a maximum used of 15s, along with the ever dominant water Raman band, requiring background subtraction. The detection limit could be reduced further by changing the measurement regime to use a TCSPAD detector. This would improve sensitivity in two ways; as the lifetime of the fluorescence emission is much longer than the near instantaneous Raman scattering, the TCSPAD can distinguish between the two allowing for complete removal of the Raman interference. Being a photon counting detector a SPAD is also inherently far more sensitive than the CCD array used by the spectrometer.

Using this detection method a detection limit closer to 10^{-12} M or lower, equating to less than 10^{-19} moles or sub attomolar detection should be possible.

The equivalent measurement, performed in the suspended core fibre, is shown in Figure 4.13.

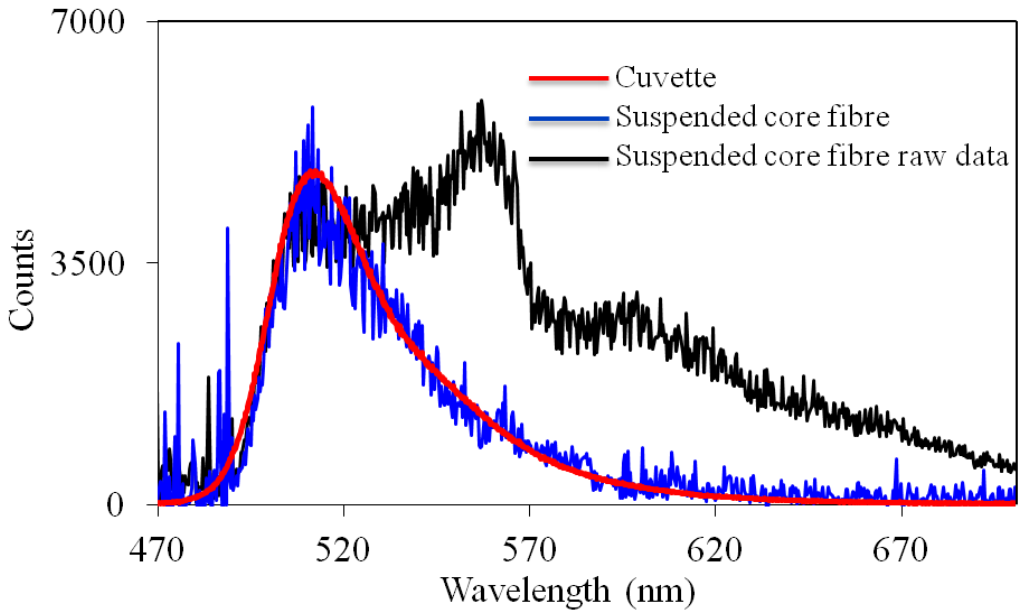

Figure 4.13: Emission spectrum Fluorescein at 10^{-10} M in water in 30 cm of suspended core PCF. Raw data (black) shows that the water Raman band is less dominant then in the HC fibre. After background subtraction (blue) the correct spectrum is obtained, as shown by reference to the cuvette measurement (red).

The fibre contains ~9 nL cm^{-1} of sample, however, due to less fluorophore molecules being excited than in the kagomé PCF, around 8% [150] of the solution compared to 98%, the inherent sensitivity is lower. The detection limit, displaying similar signal to noise as achieved within the HC fibre, was 10^{-10} M. This equates to 10 attomoles of Fluorescein within the fibre, however, due to the small light–sample overlap, a similar number of molecules are excited as in the detection limit ($2x10^{-11}$ M) case for the kagomé fibre. With a smaller volume being probed the amount of water Raman detected is also lower making the main limitation in this measurement the signal to noise ratio, allowing concentration to be reduced as for the HC–PCF measurement.

Whilst lower than the kagomé fibre the detection limit for the suspended–core fibre is not proportionally lower when compared to the probed sample volume, almost an

order of magnitude less. This can possibly be attributed to sample build up on the fibre surface increasing the measured concentration over the expected concentration; repeat measurements using a new fibre and filling times derived from the analysis in chapter 2.1.6.1 to minimise the possible amount of build-up discount this as the only factor. Another possible reason for the better than expected detection sensitivity is a greater collection angle for the emitted fluorescence. As the emission is isotropic this is an important fibre property with respect to the efficiency of fluorescence collection. As the kagomé fibre is not a true PBG–PCF it displays less–efficient confinement of the guided wavelengths within the core. This makes collection of light in the core more angle-dependent than a true PBG-HC–PCF. Light was collected from the whole of the kagomé fibre and it was noted that some light was collected by the cladding struts rather than the core as shown in Figure 4.14 as was reported in previous studies on HC fibres[130]. This is possible due to the cladding of a kagomé PCF supporting photonic states, as discussed in chapter 2.1. However, the close proximity of the fluorophores to the high NA index guiding core of the suspended core fibre may offer greater collection potential in this fibre type, explaining the relatively low detection limit compared to the kagomé fibre.

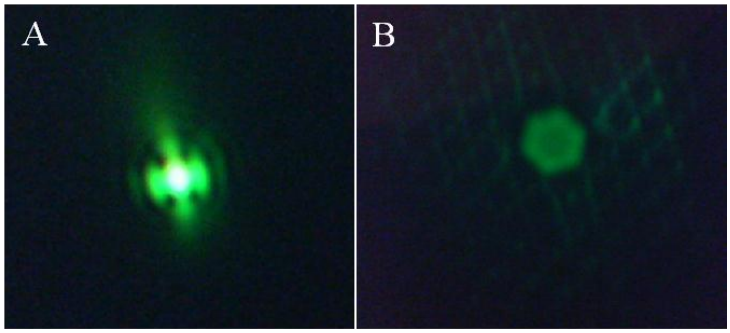

Figure 4.14: Recorded Fluorescein emission from (A) the suspended core fibre and (B) the HC kagomé fibre. Note that for the latter the guided fluorescence is not limited to the fibre core and some is also collected by the struts in the cladding which can form effective index guiding fibres with a higher acceptance angle than the core itself.

Compared to a perpendicular collection system found in a traditional cuvette spectrometer, where the maximum possible fluorescence collection efficiency is ~16 %, in a PCF ~35% of the emitted fluorescence is guided to the detector.

4.3.2. Fluorescence Lifetime Measurements

The fluorescence spectrum of Rhodamine B at 10^{-9} M in water within the kagomé fibre, measured using the ocean optics spectrometer is shown in Figure 4.15. Following this measurement the detector was changed to the SPAD for the fluorescence decay measurements.

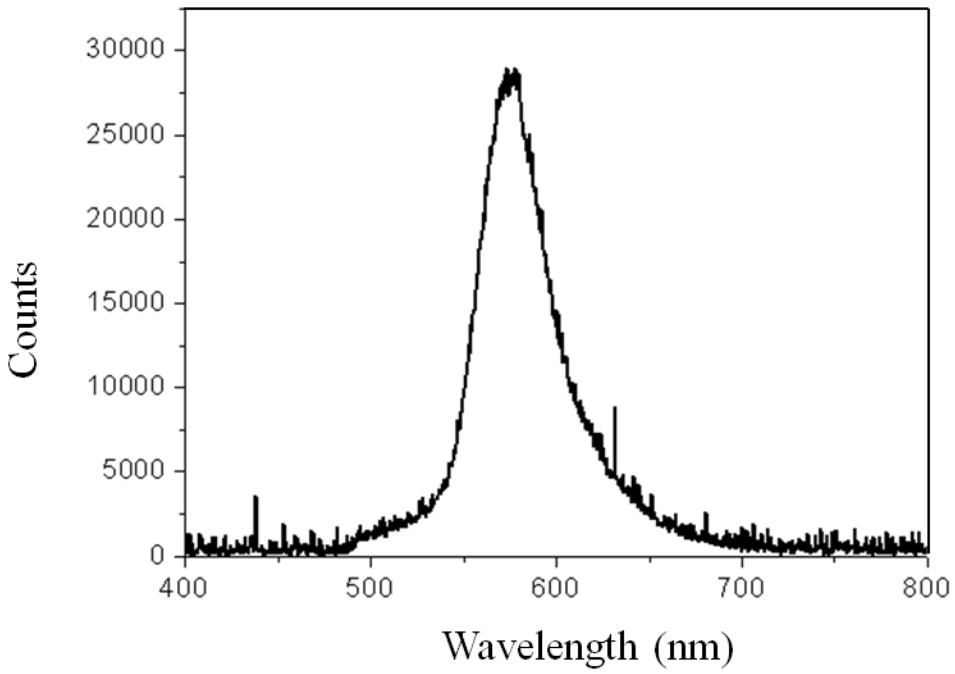

Figure 4.15: Emission spectrum of 10^{-8} M Rhodamine B excited using the 470 nm diode laser in 30 cm of kagomé fibre.

The fluorescence decay measured for the same sample concentration in the suspended core fibre is shown in Figure 4.16 . The fit to the decay performed using the instruments F900 software gave a single exponential decay with a lifetime of 3.64 ns with a χ^2 value of 1.001 indicating an excellent fit for a single lifetime. This result is in very good agreement with the value of 3.65 ns for the Rhodamine B fluorophore when attached to silica[93]. As discussed in section 4.2.2, surface adsorption prevents the rotation of the alkylamino groups reducing, the rate of non-radiative decay. This, therefore, shows that measurements made in the suspended–core fibre give a very good measure of the interaction between the fibre surface and the sample, with very little perturbation from the molecules in the larger bulk solution. The suspended–core fibre is thus an ideal environment in which to study

surface effects via evanescent field spectroscopy, given the large surface to volume ratio, of ~10 in this case, and the long path lengths that can be used.

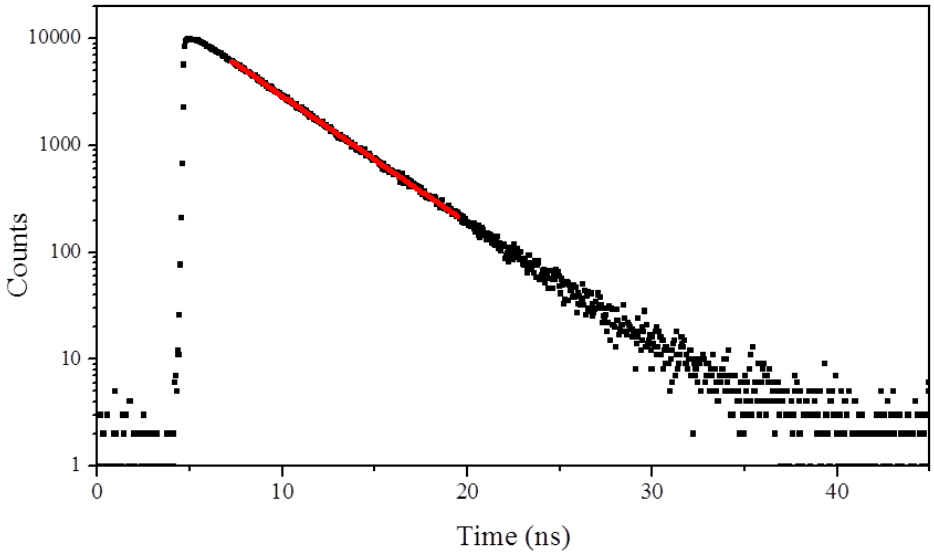

Figure 4.16: Fluorescence lifetime decay of Rhodamine B in the suspended core fibre, fitted using the F900 software (red line). A single exponential with an excellent fit is found giving a single lifetime of 3.64 ns.

The same measurement was carried out using the HC kagomé fibre and the fitted curve is show in Figure 4.17

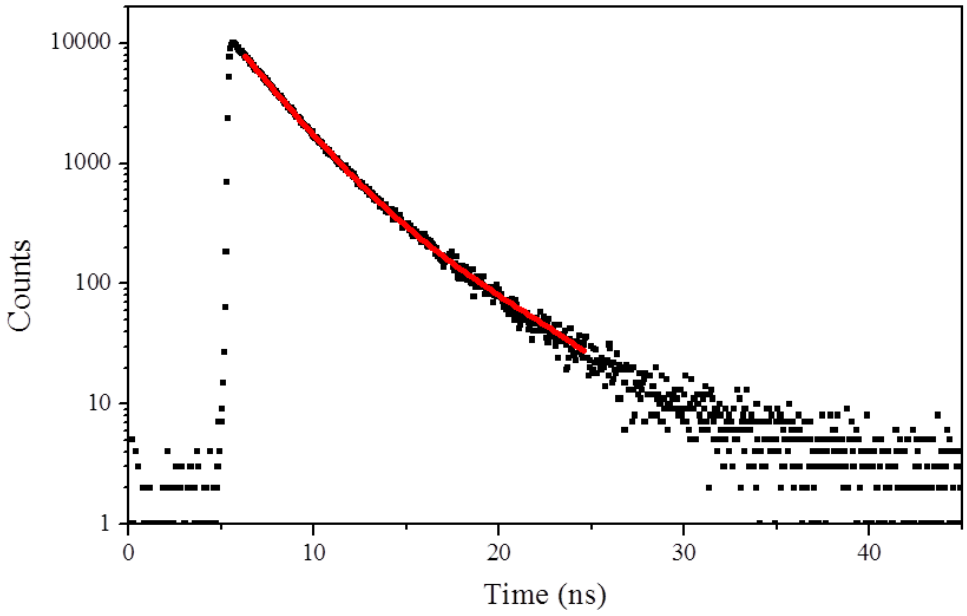

Figure 4.17: Fluorescence lifetime decay of Rhodamine B in the hollow core fibre, fitted to a bi-exponential decay function using the F900 software (red line).

The fit shows a bi-exponential decay indicating that the fluorophores being excited are in more than one environment with differing effects on the non-radiative decay processes. A summary of the exponential decay values for both fibres is given in Table 5.

Fibre Type	A factor	Uncertainty (σ)	Lifetime (ns)	Uncertainty (ns)
Suspended Core	8060	16.9	3.64	0.17
Hollow Core	7958	135.1	2.12	0.13
	538.8	117.1	4.21	1.43

Table 5: Summary of the decay components for Rhodamine B in both fibre types and the corresponding lifetimes.

In the hollow core fibre the main decay component accounts around 90 % of the emitting population and has a lifetime of 2.1 ns with an uncertainty of 3 %. Rhodamine B has a temperature dependent lifetime, as discussed in chapter 4.2.2, and so a lifetime of 2.1 ns would equate to a lab temperature of 20 degrees which is reasonable. The second decay component corresponds to a lifetime of around 4 ns, which is attributed to excitation of surface attached Rhodamine B. Whilst this value is higher than established through both the literature and our measurements in the suspended core fibre, the uncertainty is very high at ~35% due to the very low intensity of the signal compared to the fluorophores in bulk solution. This easily places the measured value within the accepted range for Rhodamine B on a surface.

These results show that the HC fibre can indeed be used for measurement of the bulk sample, with only a small influence of the surfaces, though the effect of the surface adhering molecules reducing the measured concentrations is still a problem to be overcome.

4.3.3. TPE Measurements

With the HC–PCF showing the greater sensitivity for the single photon excitation measurements it was the logical fibre of choice for the attempt to induce TPE fluorescence in PCF. The initial measurement was made using a concentration of 5×10^{-5}M Fluorescein. This is far higher than that used in the single photon measurements, due to the decrease in absorption cross section between OPE and TPE, though is still over an order of magnitude lower concentration than used in previous solution phase TPE studies of Fluorescein as discussed in section4.1.2. The average laser power of the Ti-Sapphire laser was 30 mW, and the pulse duration was around 150 fs at a repetition rate of 76 MHz. This equates to a peak irradiance in the fibre core of ~9.3×10^{8} W cm^{-2} which is over an order of magnitude lower than a typical setup where the same laser is focussed down to a smaller area[145]. The guided mode of the laser is shown in Figure 4.18 showing good confinement to the fibre core.

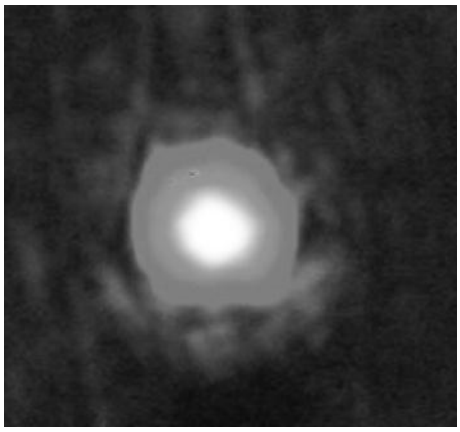

Figure 4.18: Recorded transverse mode profile of the 810 nm Ti-Sapphire laser through 30 cm of Kagomé PCF.

The result of the initial TPE measurement, using an integration time of 200 ms, is shown in Figure 4.19. Excellent signal to noise was achieved showing the emission spectrum of Fluorescein. An image of the fibre under excitation is shown Figure 4.20, the fluorescence emitted at angles greater than the collection angle of the fibre can be seen escaping from along the fibre length with decreasing intensity as the pump intensity is reduced due to dispersion of the laser pulses, reducing power density, and inherent fibre losses.

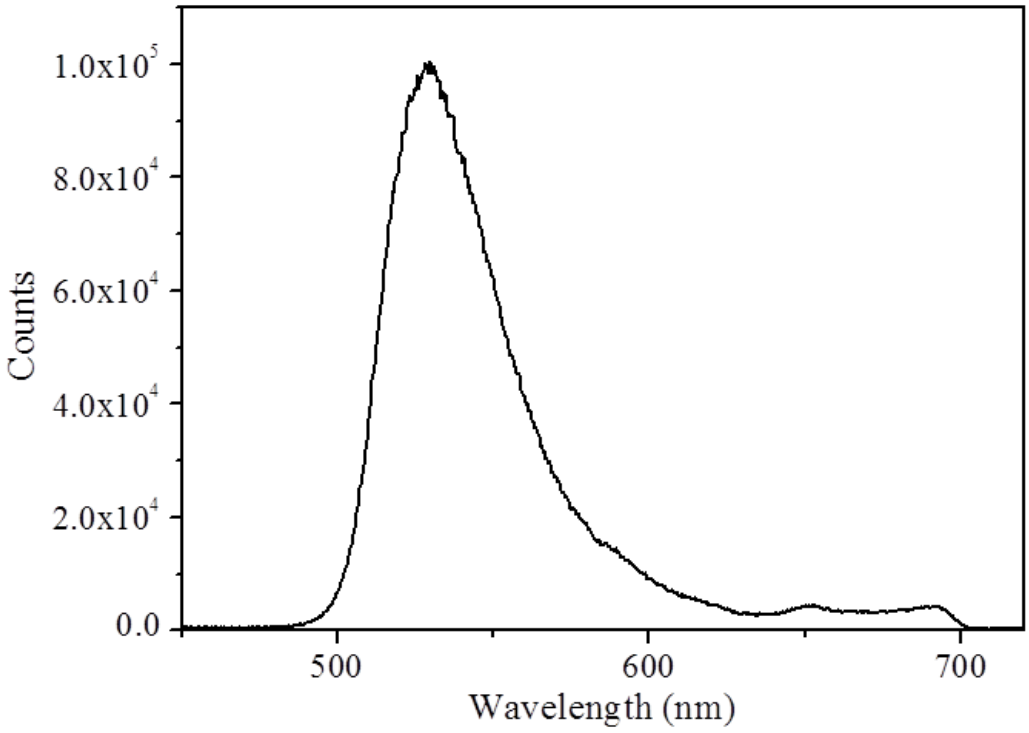

Figure 4.19: Fluorescence emission of Fluorescein excited using TPE at 810 nm using ~9.3×10^{8} W cm^{-2} from a Ti-Sapphire laser collected with an integration time of 200 ms.

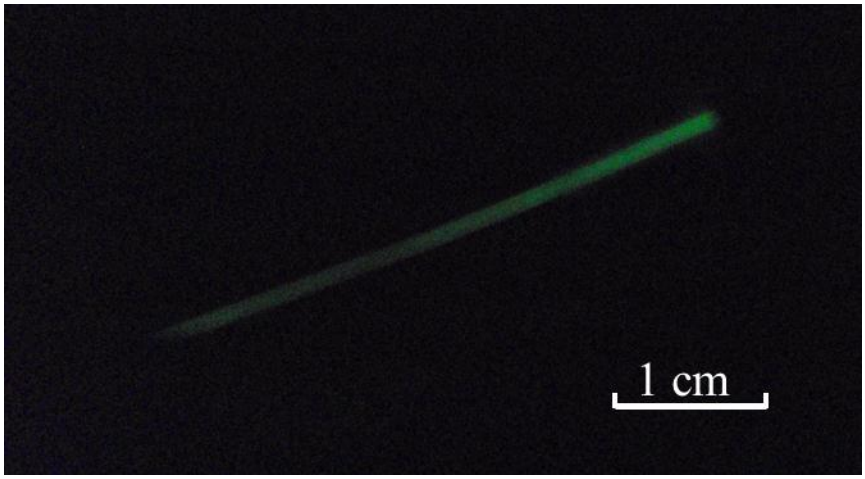

Figure 4.20: Photograph of ~7 cm of the fibre filled with 10^{-5} M Fluorescein under 810 nm excitation. In-coupling is from the right and a drop in intensity can be observed as the path length is increased.

The concentration was reduced and measurement on a concentration series performed to find the detection limit for TPE detection under these experimental

conditions, the results of this are shown in Figure 4.21 with the low concentration plots expanded in Figure 4.22.

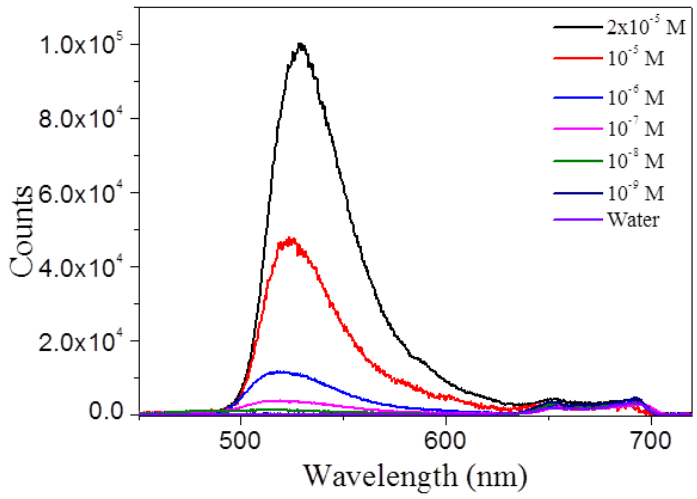

Figure 4.21: Fluorescence intensity spectra for Fluorescein in 30 cm kagomé PCF at various concentrations

The collected fluorescence intensity does not scale linearly with increasing concentration; this can be attributed to reabsorption of emitted photons down the length of the fibre, reducing observed intensity. This is discussed in more detail below.

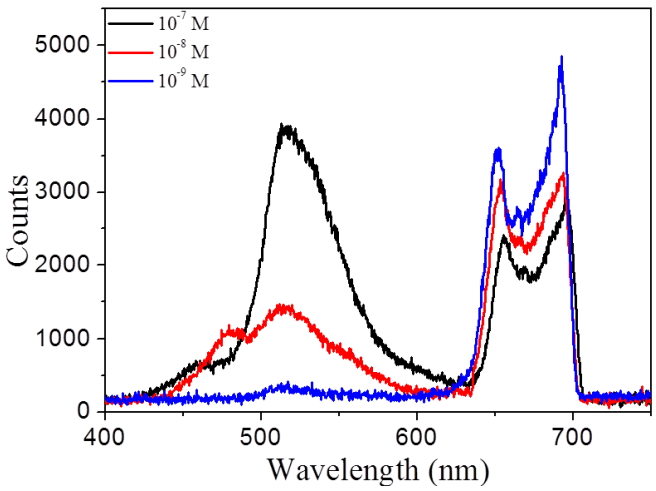

Figure 4.22: Fluorescence intensity spectra for Fluorescein in 30 cm kagomé PCF at low concentrations

It is seen that the detection limit for Fluorescein under these experimental conditions is ~10^{-9} M or 100 attomoles. Also observed are a set of peaks leading up to the 720 nm cut-off from the short pass filter used to block the laser beam. These features are

apparently independent of sample concentration and are present when the fibre is filled with the pure solvent (water). This can be attributed to the generation of a small amount super-continuum from non-linear effects within the fibre by the laser pulses at these high intensities. This would not usually be observed due to the very low intensity of the super-continuum with respect to the laser itself. Unlike the water Raman band observed in the OPE measurements, the super-continuum peaks do not coincide with the observed fluorescence and therefore do not affect the measurement.

The observed detection limit for TPE of Fluorescein with respect to the OPE, 1×10^{-9} M vs ~ 4×10^{-12} M (extrapolated), is remarkably low at only 2–3 orders of magnitude difference. This result is around four orders of magnitude lower than those reported in conventional studies on bulk solutions, even with the large core area reducing irradiance to 9.3×10^{8} W cm^{-2}, well below that used in the majority of previous studies. Studies that have used comparable excitation irradiances to those used here have relied on much higher concentrations, for example Xu[136] irradiated 100 µM solutions at $8x10^{8}$–10^{11} W cm^{-2} to produce TPE. The increase in TPE efficiency by using HC–PCF can be attributed to several factors. The confinement and guidance of the laser pulses allows for excitation of TPE fluorescence over far greater path lengths than typically possible, ~1 µm; providing a irradiance can be reached that is sufficient for TPE it will be maintained along the fibre. Further, there is high collection efficiency of the fluorescence from within the fibre, something that is hard to achieve in traditional setups, where the excitation occurs at a point in a solution and collection is made from the side. In the kagomé HC–PCF, as noted in the OPE measurements, not just the fibre core but the cladding structure aids the collection of emitted light enhancing the collection efficiency further. These measurements show that HC–PCF can be utilised to perform a measurement that is traditionally difficult, requiring high sample concentrations and exhibiting very low collection efficiency. The benefit of being able to use a lower concentration is not just the need for less material; this also avoids the effect of reabsorption that influence measurements made on high concentration samples. As some of the emitted light lies within the single photon absorption spectra of the dye it can be absorbed by the vastly more efficient OPE mechanism. As discussed in section 2.3.1.1 this has the effect of red shifting the peak of the observed emission spectrum.

The overlap of the absorption and emission spectrum for Fluorescein is shown in Figure 4.23.

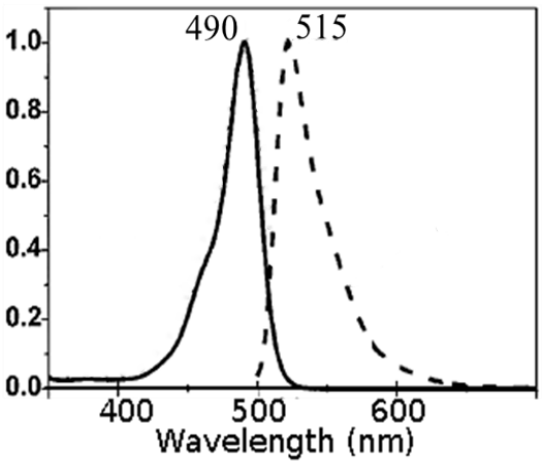

Figure 4.23: Normalised absorption (solid line) and emission (dashed line) spectrum of Fluorescein showing the overlap of the two due to the small Stokes shift.

The effect this has on the peak of the emission spectrum observed in this study is shown in Figure 4.24, it is seen that at concentrations above 10^{-8} M the presence reabsorption can be observed. This is a lower concentration than would typically be attributed to the onset of this phenomenon because of the long path length being using in comparison to traditional setups, greatly increasing the probability of a reabsorption event occurring.

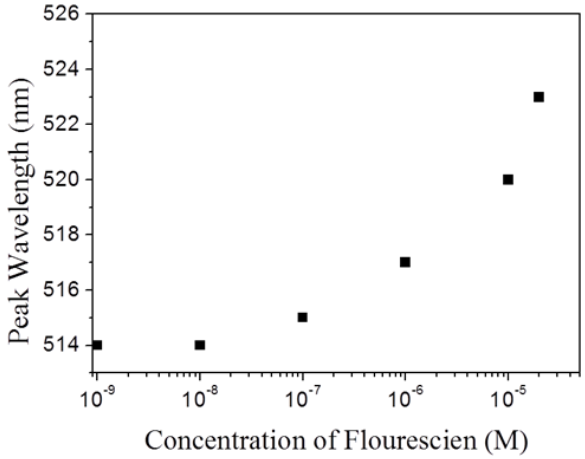

Figure 4.24: Effect of increasing concentration on the observed peak of the fluorescence emission of Fluorescein due to reabsorption of lower wavelengths.

To confirm that the observed fluorescence was being induced by TPE rather than another mechanism, further measurements were made in which the excitation intensity was varied whilst the concentration of fluorophore remained constant. As with all TPE processes, the increase of fluorescence intensity with pump intensity should follow a non-linear square law relationship, until excitation saturation is achieved. The results of such a measurement series on a solution of 10^{-6} M Fluorescein are shown in Figure 4.25 with a corresponding plot of the integrated emission intensity vs average incident laser power shown in Figure 4.26.

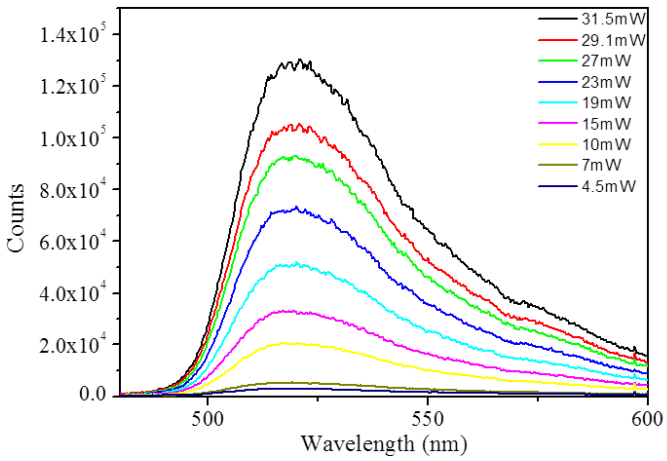

Figure 4.25: Dependence of fluorescence emission intensity of on incident average laser power at 810 nm.

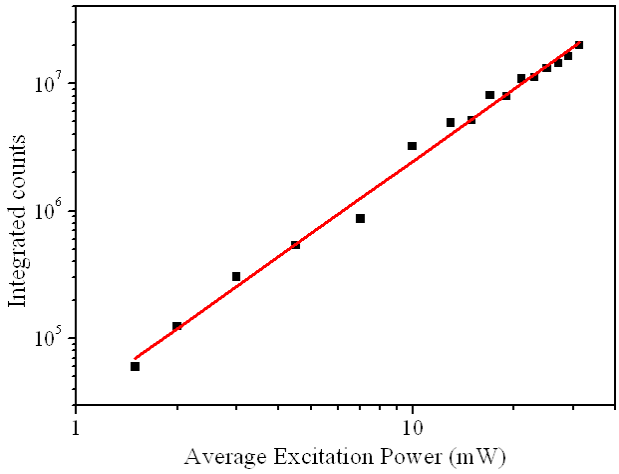

Figure 4.26: Log–log plot of emission intensity versus incident average laser power at 810 nm. The fitted red curve shows a power law dependence of 1.89.

The fluorescence emission intensity scales as the laser power raised to the power 1.89 (fitted line on plot) which confirms the excitation process as being TPE.

4.4. Conclusions

It has been demonstrated that PCF can be used as a highly efficient system for the excitation and detection of fluorescence from within the fibre structure. The use of a HC–PCF, designed to guide when filled with solution, allowed the excitation and detection of fluorescence from 90 nL of 2×10^{-11} M Fluorescein which equates to only 1.8×10^{-18} moles (1.8 attomoles) or $\sim10^{6}$ molecules. This is the lowest reported detection limit from within PCF, and is due to the long path–lengths that could be obtained by having a well-defined PCF guidance mechanism, which efficiently collected the emitted fluorescence. The use of a suspended-core fibre demonstrated the extremely high sensitivity for evanescent field excitation. A Fluorescein concentration as low as 10^{-10} M could be detected, showing the potential of PCF for long path length highly sensitive evanescent field detection.

The ability of PCF to preserve the fluorescence lifetime profile of a fluorophore was demonstrated, allowing accurate measurement of this property for both evanescent and bulk excitation. These measurements allowed for the location of the excited fluorophores to be determined with respect to the fibre surface, by using a fluorophore with a lifetime that differed between bulk solution and surface adsorption. In–fibre lifetime measurements on a dye such as Rhodamine B used here open up the possibilities for in fibre temperature detection. This could be extremely useful in future experiments where, for example, bio-molecules or cells could be studied within the fibres. In such experiments the addition of a temperature–dependent fluorophore could ascertain any temperature fluctuation due to laser heating, or other external influence.

Furthermore, it has been shown that PCF is a highly efficient system for TPE fluorescence measurements on solution–phase samples. The detection limit of 10^{-9} M is four orders of magnitude lower than those achieved in traditional measurements, made possible by the excellent confinement and guidance of high power densities over a long path length. The ability to perform such measurements on extremely small sample volumes in a highly contained environment, allowing for efficient quantitative excitation and collection of fluorescence, opens up the possibility for the relatively straight-forward study of two–photon systems that are

expensive and difficult to observe in traditional systems. The potential demonstrated for two-photon excitation within PCF paves the way for the study of two-photon induced photochemistry which is of particular interest in areas such as photodynamic therapy for cancer treatment where there is increasing interest in the development of photodynamic agents that can be activated by two-photon excitation.

5. Overall Conclusions and Outlook

The work presented in this thesis has demonstrated the potential of using photonic crystal fibres as a means for performing highly sensitive optical measurements in very small sample volumes under extremely controlled conditions.

PCF used as a micro–reaction chamber allowed the monitoring of the photoisomerisation process of two azobenzene–based dyes, Disperse Red 1 and Disperse Orange 1, using pump–probe UV–Vis absorption spectroscopy in near real-time. Both the 488 nm excitation laser and the broadband light source for measurements were co-coupled through the fibre, giving perfect overlap of both beams with the sample, allowing accurate knowledge of the sample excitation parameters. The hollow core kagomé-type fibre with a core diameter of 19 µm allowed measurements over a 30 cm path length whilst requiring only 90 nL of at a concentration of 10^{-5} M, five orders of magnitude less volume and an order of magnitude lower concentration than required in a conventional spectrometer.

The kinetics of the photoisomerisation from the *trans* to the *cis* isomers of the dyes and the thermally driven *cis* to *trans* isomerisation were tracked on the millisecond timescale. This provided data which was numerically fitted using a custom model give isomerisation rate values in excellent agreement with previously established figures. Due to the well-known irradiation parameters, calculation of the quantum yield of the processes could be determined, which for "push–pull" azo-benzene molecules has only once been previously achieved. Furthermore, the measurement of the dyes in pentane, in which they are highly insoluble, could be achieved due to the low concentrations that could be used; such measurements have not previously been reported.

The study of photonic crystal fibre as a system for the excitation and collection of fluorescence was demonstrated in two types of fibre; the same kagomé based hollow core fibre and a suspended core "Mercedes" fibre. This allowed for the excitation of fluorophores in two contrasting environments. In the kagomé fibre fluorophores in bulk solution are excited whilst, in the Mercedes fibre, only fluorophores either on or in close proximity to the silica core interact with the evanescent field of the

excitation light. The Fluorescein fluorophore was used initially to measure the exceptional detection limits in both fibre types and limits of 2×10^{-11} M in the kagomé and 10^{-9}M in the Mercedes fibre were obtained. This equates to 10^{6} molecules in the kagomé fibre, which displays the lower detection limit due to greater light-sample interaction. Two-photon excitation of the Fluorescein fluorophore was then carried out using a mode-locked Ti-Sapphire laser as an excitation source demonstrating the ability of the fibre system to sustain two-photon excitation of a long (30 cm) path length. The detection limit of 10^{-9} M in the hollow core fibre is excellent at over 4 orders of magnitude lower than a typical two-photon excitation experiment, proving PCF to be an exceptionally advantageous system in which to monitor TPE processes on small sample volumes.

Using the two fibre types, measurement of the fluorescence lifetime of the Rhodamine B fluorophore was achieved. Unperturbed lifetimes could be measured in the fibres showing no interference from the guidance of fluorescence through the fibre length. The measurements were in excellent agreement with known lifetime values, showing that in the kagomé fibre the excited fluorophores are in the bulk solution with only a minor influence from surface effects, whilst in the Mercedes fibre the majority of the excited molecules experience interaction with the surface of the silica core. This, therefore, gives an accurate method of locating the fluorophores with respect to the fibre surface and the ability to choose between measurement of bulk solution and long–path–length evanescent field–induced fluorescence.

5.1 Outlook

The work presented shows proof–of–principle results for a well–known photochemical process and fluorescence measurements in the novel environment of PCF. The extremely well defined excitation and probe parameters over very long path lengths allowed the reaction kinetics of the photochemical process and the fluorescence detection of fluorophores to be carried out on far lower concentrations than typically possible and with lower excitation powers. The work paves the way for extensive further work in this area. Directly related to the photoisomerisation work presented, the further development of the experimental design to allow for continuous measurements to be performed instead of using the pump–probe regime

can be achieved through using a counter–propagating setup where the pump and probe light enter at opposite ends of the fibre. The experimental construction to achieve this is non–trivial and the development so far is presented in Appendix A. As a final improvement for the specific cases such as the reversible photoisomerisation process studied here, the addition of a further excitation source of different wavelength would allow for the use of the Fischer method[151] to determine the absorbance spectrum of the *cis* isomer, something which it is typically not possible to observe directly. This is also covered in Appendix A.

Moreover, the incorporation of PCFs as photochemical reactors in lab-on-a-chip type devices could revolutionise high-throughput screening of photoactive targets and the application of photochemistry based assays in micro-total-analysis systems. The development of an all-fibre optofluidic photo-reactor can be envisaged, in which fibre lasers and/or PCF-based supercontinuuum sources, as pump and probe, are integrated with the sample-containing PCF.

When combining the excellent TPE excitation results from the fluorescence portion of the work into the photochemistry setup for the study of two-photon induced photochemical process on small sample volumes in bulk solution with high sensitivity can be achieved, this should allow straight forward monitoring of molecules such as are being developed for PDT. Combining coated fibres such as previously reported with the highly sensitive bulk solution or evanescent–field detection shown here should allow for the construction of compact, highly sensitive detectors for a vast array of applications.

Appendix A. Improvements to Photochemistry Experimental Design

The final experimental design used for the experimental results used in the work presented in this thesis can be improved in a numbers of ways.

Counter-Propagating Setup

By moving the pump laser source to the opposite end of the fibre, thereby creating counter-propagating beam paths for the pump and probe light, the need to use shutters to protect the spectrometer from saturation can be avoided. A schematic for such a setup is shown in Figure A.1.

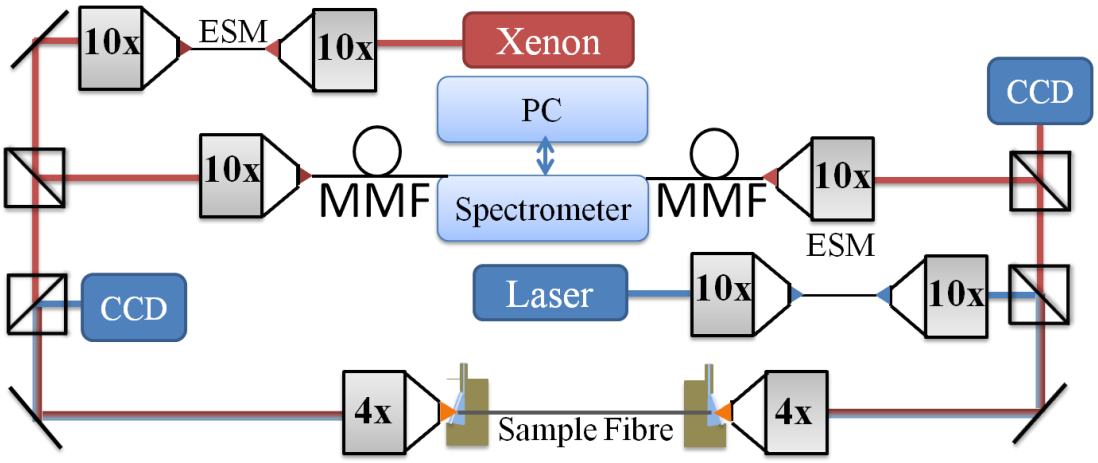

Figure A.1: Schematic of the experimental setup for a counter-propagating beam path. New sample cells reduce reflection of the laser beam.

Whilst in theory this method of conducting the experiments should allow for real–time shutter–less measurements to be performed, reflections from the glass windows on the liquid cells combined with those of the in-coupling objective was still sufficient to saturate the spectrometer. To try and alleviate this problem the sample cells were redesigned to have the glass windows through which light is coupled into and out of the fibres at an angle. This made in-coupling more difficult as due to the displacement caused by the angled glass but the reflected light was now misaligned with the incoming beam, removing it from the measured light path. With this improvement a complete counter-propagating setup is almost possible, antireflective

objectives and cell windows should reduce the excitation light entering the spectrometer to a manageable level.

Bi-laser Counter-Propagating Setup

A final improvement that could be made to the experimental design, for the purpose of measuring the photoisomerisation of the azobenzene–based dyes used in this work would be the addition of a second excitation wavelength through additional excitation sources. This is shown in Figure A.2. With measurements made at two distinct wavelengths the analysis technique known as the Fischer method can be used to determine the exact *cis*-isomer absorption spectra, something that is normally unobservable with a conventional UV–Vis measurement due to the continual thermal process producing *trans* isomer molecules.

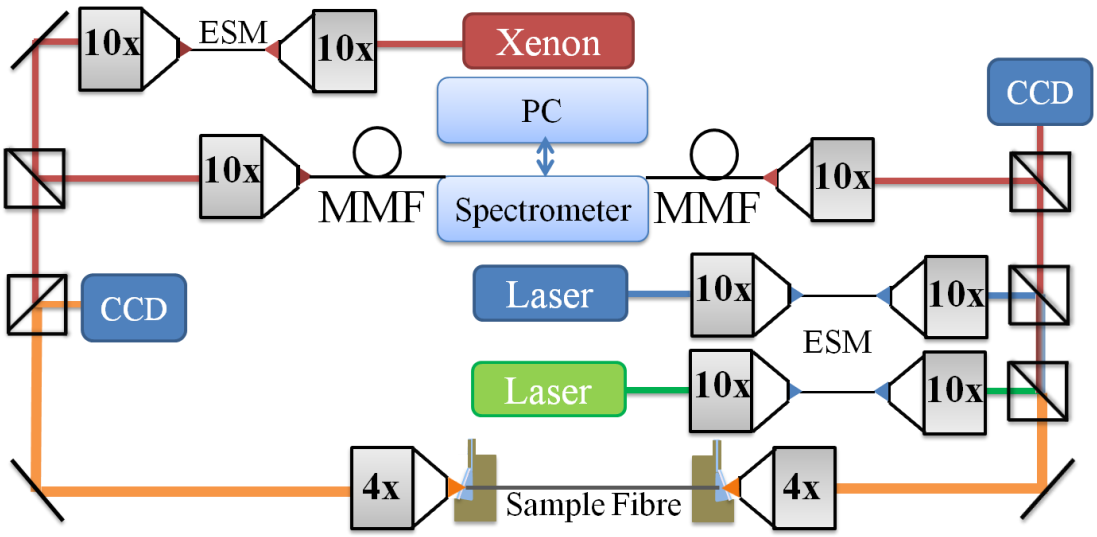

Figure A.2: Counter-propagating setup with two excitation lasers at 488 nm and 532 nm allowing application of the Fischer method for product spectra determination.

Appendix B. Photochemistry Kinetic Model

The kinetic modelling of the photoisomerisation of azobenzene dyes takes place in two stages. First the data for the thermal *cis–trans* process is fitted with a single exponential decay to allow this perimeter to be set when fitting the data for the photo–induced isomerisation process. The only unknown variables in the rate equations for the process (given in section 2.2.4) are now the rates of photoisomerisation from *trans–cis* and *cis–trans*. From a given starting value for the *trans-cis* rate the model program runs an optimised least squared fit to the data by varying the ratio of the two process rates and a second optimisation to then find the optimum values of the rates. As the quantum yield of the *trans–cis* proccess is simply

$$\phi = \frac{\Gamma_{trans-cis}}{\Gamma_{cis-trans} + \gamma}$$

Where Γ is a photoinduced rate and γ is the thermal *cis-trans* rate, which is small in comparison to the photo–induced–rates. The final ratio given by the model program, therefore, represents the quantum yield of the *trans–cis* process.

For both parts of the fitting process a complete numerical calculation is performed integrating through time and using a discrete integration through the length of the fibre to take into account reduction in incident intensity on the sample along the fibre length due to both absorption and fibre guidance losses.

The relevant parts of the JAVA™ code written for the modelling of the photo isomerisation kinetics of azobenzene dyes in PCF are presented below along with the program graphical user interface allowing for input of known and free parameters for fitting both the complete photoisomerisation or just the thermal process, after prior excitation. The code was written in collaboration with Gwylim Williams.

First the fibre is populated with molecules according to the parameters input by the user, such as concentration, absorbance cross section, wavelength of excitation, fibre length:

```
package com.gwylim.fibre.logic.state;
1
import com.gwylim.fibre.logic.paramiters.SimulationParameters;
2
3
/**
4
 * Create the initial state of the fibre. All segments contain the same
5
 * initial values for cis and trans molecules.
6
 * @author Rage
7
 *
8
 */
9
public class InitialState extends State {
10
    public InitialState(final SimulationParameters p, final double time) {
11
        super(time, p.getAccuracy());
12
        for(int i=0;i < p.getAccuracy().LengthSegments();i++) {
13
            _segments.add(new SegmentMolecularState(p.trans0MoleculeOPErSegment(),
14
            p.cis0MoleculeOPErSegment(), 0, p));
15
        }
16
    }
17
}
```

The fibre state is then progressed through time and space globally from the initial state with a space "integration" being performed for each time step. Due to the enormous computational load of a full integration through space a "length segment" chosen by the user over which the loss is small, for example 1cm. Light intensity entering each segment is then calculated and used when performing absorbance calculations for the following segment as so on. When the irradiation intensity is zero only the thermal calculation is performed, otherwise the pump probe procedure us replicated. The state of the fibre at a given time is calculated as follows.

```java
package com.gwylim.fibre.logic.state;
import java.util.ArrayList;
import com.gwylim.fibre.logic.paramiters.SimulationAccuracy;
/**
 * The state of the whole fibre at a given time.
 * @author Gwylim
 *
 */
public class State {
    /** The simulation Parameters */
    private final SimulationAccuracy _paramiters;
    /**
   * List of segments that this fibre contains.
   */
    final public ArrayList<SegmentMolecularState> _segments = new
    ArrayList<SegmentMolecularState>();
    /** The time from start that this state occurred. */
    private final double _time;
    public State(final double time, final SimulationAccuracy simulationAccuracy) {
        _time = time;
        _paramiters = simulationAccuracy;
    }
    /**
   * Gets the absorbance at the end of the fibre as calculated. Ie at the end of
   * all the segments that have CURRENTLY been added to the fibre.
   * @return The absorbance value.
```

```
27    */
28    public double getAbsorbance() {
29        double absorbance = 0;
30        for (final SegmentMolecularState segment : _segments) {
31            absorbance += segment.absorbance();
32        }
33        return absorbance;
34    }
35    /**
36    * Add a state to the end of this fibre.
37    * @param state the state to add.
38    */
39    private void add(final SegmentMolecularState state) {
40        _segments.add(state);
41    }
42    /**
43    * Get the segment at the given position in the fibre.
44    */
45    private SegmentMolecularState get(final int pos) {
46        return _segments.get(pos);
47    }
48    /**
49    * Get the time for this state.
50    */
51    public double getTime() {
52        return _time;
```

```
53  }
54  @Override
55  public String toString() {
56      final StringBuilder sb = new StringBuilder();
57      sb.append("State\nTime: " + _time);
58      sb.append("\nAbsorbance: " + getAbsorbance());
59      return sb.toString().substring(0);
60  }
61  /**
62  * Perform the thermal step of the simulation. This state is unchanged.
63  * @return The new state after thermal step.
64  */
65  public State thermal(final double duration) {
66      State lastState = this;
67      final int numberOfThermalTimeSteps = _paramiters.ThermalTimeSteps();
68      final double thermalTimeStepLength = duration / numberOfThermalTimeSteps;
69      for (int timeStep = 0; timeStep < numberOfThermalTimeSteps; timeStep++) {
70          final State workingState = new State(lastState.getTime() +
71          thermalTimeStepLength, _paramiters);
72          for (int spaceStep = 0; spaceStep < _segments.size(); spaceStep++) {
73              final SegmentMolecularState previousSegmentState = lastState.get(spaceStep);
74              final SegmentMolecularState next =
                previousSegmentState.nextState(thermalTimeStepLength, 0);
75              workingState.add(next);
76          }
77          lastState = workingState;
78      }
```

```
79      return lastState;
80    }
81    /**
82   * Perform the irritation step. This state is unchanged.
83   * @param incidentIntencity The intensity into the start of the fibre.
84   * @return The irritation step of the simulation.
85   */
86    public State irradiation(final double duration, final double incidentIntencity) {
87      State lastState = this;
88      final int numberOfIrradiationTimeSteps = _paramiters.IrradiationTimeSteps();
89      final double irradiationTimeStepLength = duration / numberOfIrradiationTimeSteps;
90      for (int timeStep = 0; timeStep < numberOfIrradiationTimeSteps; timeStep++) {
91        final State workingState = new State(lastState.getTime() +
          irradiationTimeStepLength, _paramiters);
92
93        for (int spaceStep = 0; spaceStep < _segments.size(); spaceStep++) {
94          final double intensity = workingState.getIntensity(incidentIntencity);
95          final SegmentMolecularState previousSegmentState = lastState.get(spaceStep);
96          final SegmentMolecularState next =
           _previousSegmentState.nextState(irradiationTimeStepLength, intensity);
97          workingState.add(next);
98        }
99        lastState = workingState;
100     }
101     return lastState;
102   }
103   /**
104  * Get the intensity at the end of the fibre in its current state... This is
```

```
105     * used during construction to find the intensity going into the next segment
106     * to be calculated.
107     */
108     private double getIntensity(final double incidentIntensity) {
109         double intensity = incidentIntensity;
110         for (final SegmentMolecularState segment : _segments) {
111             intensity = segment.getIntensity(intensity);
112         }
113         return intensity;
        }
    }
```

Called from this method is the calculation of the absorbance at each time and space, this is calculated and moved on in time using the Runge–Kutta method as discussed in the photochemistry in PCF chapter (3). This is the actual integrator for time within the program.

```
1   package com.gwylim.fibre.logic.state;
2   import com.gwylim.fibre.logic.paramiters.Constants;
3   import com.gwylim.fibre.logic.paramiters.SimulationParameters;
4   /**
5    * A representation of a segment of a fibre for a n instant in time.
6    * @author Gwylim
7    */
8   public class SegmentMolecularState {
9       private final double _trans;
10      private final double _cis;
11      private final double _excited;
12      private final SimulationParameters _paramiters;
```

```
13  public SegmentMolecularState(final double trans, final double cis, final double
    excited, final SimulationParameters p) {
14      _trans = trans;
15      _cis = cis;
16      _excited = excited;
17      _paramiters = p;
18  }
19
20  private double getTrans() {
21      return _trans;
22  }
23  private double getCis() {
24      return _cis;
25  }
26  private double getExcited() {
27      return _excited;
28  }
29  /**
30  * The absorbance of this section of fibre.
31  * @return The absorbance.
32  */
33  public double absorbance() {
34      return (
35              (((_trans / Constants.avagadrosConstant) /
36                _paramiters.getSegmentVolume()) *
37                _paramiters.getSpecification().transExtinctioneCoef())
38              +
```

```
39                  ((_cis / Constants.avagadrosConstant) / _paramiters.getSegmentVolume())
40                   * _paramiters.getSpecification().cisExtinctionCoef()
41                 )
42                 * _paramiters.getLengthOfSegment();
43  }
44  /**
45 * Gets the intensity that comes out of this section of fibre given the input
46 * intensity.
47 * @param incidentIntensity The input intensity.
48 * @return The intensity that emerges from the other end of the segment.
49 */
50  public double getIntensity(final double incidentIntensity) {
51     return (incidentIntensity * Math.exp(-_paramiters.getSpecification().FibreLoss() *
              _paramiters.getLengthOfSegment())) * Math.pow(10, -absorbance());
52  }
53  /**
54 * Calculate the state of this segment of fibre after the given length of
55 * time. Using the 4th order Runge Kutta method.
56 * @param time The time until the next state.
57 * @param intensity The intensity of light during that time.
58 * @return The state of the fibre after the time.
59 */
60  public SegmentMolecularState nextState(final double time, final double intensity) {
61     final double k1 = time * t(getTrans(), getCis(), getExcited(), intensity);
62     final double l1 = time * c(getTrans(), getCis(), getExcited(), intensity);
63     final double m1 = time * e(getTrans(), getCis(), getExcited(), intensity);
64     final double k2 = time * t(getTrans() + k1 / 2, getCis() + l1 / 2, getExcited()
```

```
                    + m1 / 2, intensity);
    final double l2 = time * c(getTrans() + k1 / 2, getCis() + l1 / 2, getExcited()
                    + m1 / 2, intensity);
    final double m2 = time * e(getTrans() + k1 / 2, getCis() + l1 / 2, getExcited()
                    + m1 / 2, intensity);
    final double k3 = time * t(getTrans() + k2 / 2, getCis() + l2 / 2, getExcited()
                    + m2 / 2, intensity);
    final double l3 = time * c(getTrans() + k2 / 2, getCis() + l2 / 2, getExcited()
                    + m2 / 2, intensity);
    final double m3 = time * e(getTrans() + k2 / 2, getCis() + l2 / 2, getExcited()
                    + m2 / 2, intensity);
    final double k4 = time * t(getTrans() + k3, getCis() + l3, getExcited() + m3,
    intensity);
    final double l4 = time * c(getTrans() + k3, getCis() + l3, getExcited() + m3,
    intensity);
    final double m4 = time * e(getTrans() + k3, getCis() + l3, getExcited() + m3,
    intensity);
    final double znew = getCis() + (l1 + 2 * (l2 + l3) + l4) / 6;
    final double ynew = getTrans() + (k1 + 2 * (k2 + k3) + k4) / 6;
    final double wnew = getExcited() + (m1 + 2 * (m2 + m3) + m4) / 6;
    return new SegmentMolecularState(ynew, znew, wnew, _paramiters);
}
/** ODE for TRANS state with irritation. */
private double t(final double trans, final double cis, final double excited, final
double intensity) {
    return ((-intensity / (Constants.planksConst *
            _paramiters.getSpecification().frequency())) * _paramiters.transCrossSection()
            * trans)
                + (_paramiters.getSpecification().Thermalrate() * cis)
```

```
91                  + (_paramiters.getSpecification().ExciteDeacayRateTrans() * excited);
92      }
93      /** ODE for Cis state with irritation */
94      private double c(final double trans, final double cis, final double excited, final
        double intensity) {
95
          return ((-intensity / (Constants.planksConst *
                  _paramiters.getSpecification().frequency())) * _paramiters.cisCrossSection()
100               * cis)
                    - (_paramiters.getSpecification().Thermalrate() * cis)
                    + (_paramiters.getSpecification().ExciteDecayRateCis() * excited);
      }
      /** ODE for excited state state with irritation */
      private double e(final double trans, final double cis, final double excited, final
      double intensity) {
          return (((intensity / (Constants.planksConst *
                  _paramiters.getSpecification().frequency())) * _paramiters.transCrossSection()
                  * trans)
                    + ((intensity / (Constants.planksConst *
                  _paramiters.getSpecification().frequency())) * _paramiters.cisCrossSection()
                  * cis))
                    - (_paramiters.getSpecification().ExciteDeacayRateTrans() +
                  _paramiters.getSpecification().ExciteDecayRateCis()) * excited;
      }
  }
```

The exact nature of each experiment is simulated using the above at each step by the following code, where experimental data for absorbance values and timeframes for excitation and “dark” measurement times are read in. This is how the pump–probe nature of the experiments is accounted for.

```
1   package com.gwylim.fibre.logic.simulations;
```

```
2  import java.awt.geom.Point2D;
3  import java.util.LinkedList;
4  import java.util.List;
5  import com.gwylim.charter.Series;
6  import com.gwylim.fibre.logic.Curve;
7  import com.gwylim.fibre.logic.CurveImpl;
8  import com.gwylim.fibre.logic.Simulation;
9  import com.gwylim.fibre.logic.paramiters.SimulationParameters;
10 import com.gwylim.fibre.logic.state.InitialState;
11 import com.gwylim.fibre.logic.state.State;
12 /**
13  * Simulation that just simulates the given experiment. The times are aligned
14  * with the recorded times given.
15  *
16  * (Parameter->ThermalDuration) is unused.
17  *
18  * @author Rage
19  */
20 public class TimeAlignedSimulation implements Simulation {
21     private final SimulationParameters _paramiters;
22     /** List of states we have been in. */
23     private LinkedList<State> _fibreStates;
24     / **
25   * List of times we are going to calculate for.
26  */
27   private final LinkedList<Double> _times;
```

```
28  public TimeAlignedSimulation(final SimulationParameters paramiters, final Series
    points) {
29      _paramiters = paramiters;
30      _times = new LinkedList<Double>();
31      for (final Point2D point : points.getData()) {
32          _times.add(point.getX());
33      }
34  }
35  /**
36  * Run the simulation.
37  */
38  @Override
39  public void run() {
40      if (_fibreStates != null) {
41          throw new IllegalStateException("You cannot reuse TimeAlignedSimulations");
42      }
43      _fibreStates = new LinkedList<State>();
44      // Add the initial state of the fibre.
45      _fibreStates.add(new InitialState(_paramiters, _times.get(0)));
46      // loop for running though irritation steps
47      for (final Double time : _times) {
48          if (time == _times.get(0)) {
49              continue;
50          }
51          final State last = _fibreStates.getLast();
52          final double duration = time - last.getTime();
53          final double irradiationDuration =
```

```
54          _paramiters.getSpecification().IrradiationDuration();
55          final double thermalDuration = duration - irradiationDuration;
56          // advance by one time step.
57          if (irradiationDuration == 0) {
58              // No irritation.
59              final State afterThermal = last.thermal(thermalDuration);
60              _fibreStates.add(afterThermal);
61          }
62          else {
63
64              // Irritation.
65              final State afterIrradiation = last.irradiation(irradiationDuration,
66            _paramiters.getSpecification().IncidentIntesity());
67              final double probeLightIntensity =
68            _paramiters.getSpecification().probeLightIntensity();
69              if (probeLightIntensity == 0) {
70                  // Thermal with no probe light...
71                  final State afterThermal = afterIrradiation.thermal(thermalDuration);
72                  _fibreStates.add(afterThermal);
73
74              } else {
75                  // Thermal with probe light...
76                  final State afterThermal = afterIrradiation.irradiation(thermalDuration,
77                  probeLightIntensity);
78                  _fibreStates.add(afterThermal);
79              }
```

```
80          }
81      }
82      /**
83     * Get the list of states.
84     */
85      @Override
86      public List<State> getStates() {
87          if (_fibreStates == null) {
88              throw new IllegalStateException("getStates() called on TimeAlignedSimulation
                before it has been run!");
89          } else {
90              return _fibreStates;
91          }
92      }
93      /**
94     * Get the absorbance curve over time for duration of the simulation.
95     */
96      @Override
97      public Curve getAbsorbanceCurve() {
98          return new CurveImpl(getStates());
99      }
100 }
101
```

An example of the model interface for the thermal fitting:

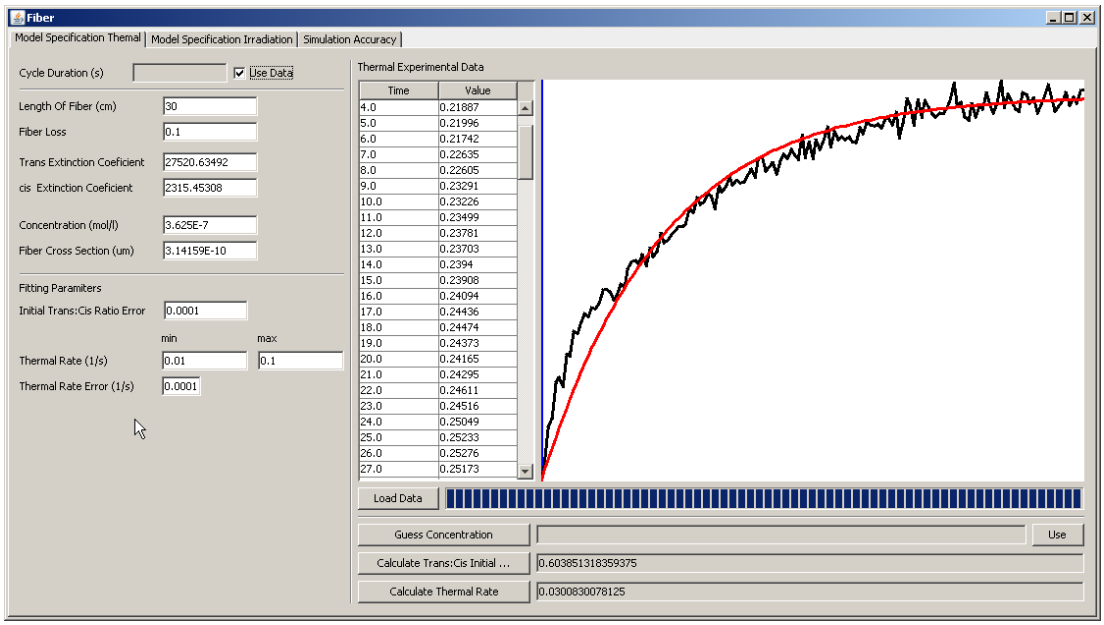

An example of the model interface for the photoisomerisation fitting:

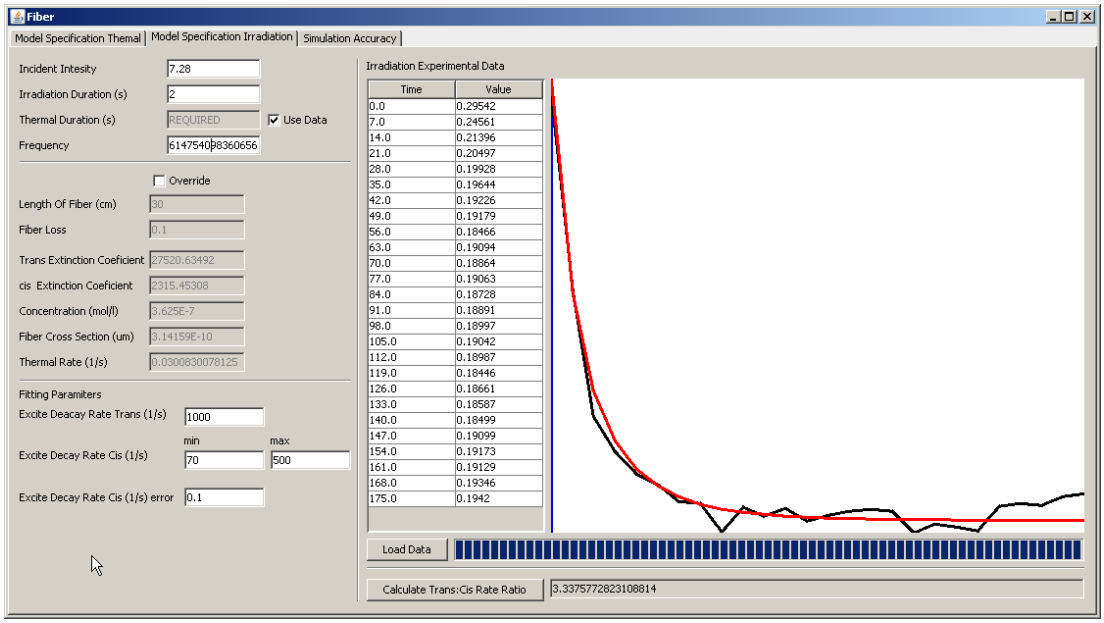

References

[1] J.C. Knight, T.A. Birks, P.St.J. Russell, D.M. Atkin, *Opt. Lett.* 21, 1547 (1996)

[2] J.C. Knight, Nature, Vol. 424, 847-851 (2003)

[3] J.M. Dudley, G. Genty, S. Coen. *Rev. Mod. Phys*., 78(4), 1135-1184 (2006)

[4] W.J. Wadsworth, R.M. Percival, G. Bouwmans, J.C Knight, P.St.J. Russell, *Opt. Express*, 11(1), 48-53 (2003)

[5] A.M.R. Pinto, M. Lopez-Amo, *Journal of Sensors*, 2012, 1-21 (2012)

[6] K.C. Kao, H.G.A Hockham, *Proc. IEEE*, 133, 1151-1158 (1966)

[7] F.P. Kapron, D.B. Keck, R.D. Maurer, *Appl. Phys. Lett*, 17, 423-425 (1970)

[8] K. Saito, M. Yamaguchi, H. Kakiuchida, A.J Ikushima, K. Ohsono, *Appl.Phys. Lett.*, 83, 5175-5177 (2003)

[9] P.St.J. Russell, *Science*, 299, 358-362 (2003)

[10] P. Vukusic, J.R. Sambles, *Nature*, 424, 852-855 (2003)

[11] W. Bragg, L. Bragg, *Proc. Camb. Phil. Soc.*, 17, 43-57 (1912)_

[12] V. N. Melekhin and A. B. Manenkov, *Zhunral Tekhnicheskoi Fiziki*, 38, 2113-2117 (1968)

[13] P. Yeh, A. Yariv, E. Marom, *J. Opt. Soc. Am.*, 68, 1196-1201 (1978)

[14] Y. Fink. D. J. Ripin, S. Fan, C. Chen, J. D. Joannepoulos, E.L. Thomas, *Journal of Lightwave Technology*, 17 2039-2041 (1999)

[15] D. Torres, O. Weisberg, G. Shapira, C. Anastassiou, B. Temelkuran, M. Shuragalin, S. A. Jacobs, R.U. Ahmad, T. Wang, U. Kolodny, S. M. Shapshay, Z. Wang, A. K. Devaiah, U. D. Upadhyay, J. A. Koufman, *Proc. Of SPIE*, 5686. 310-321 (2005)

[16] E. Yablonovitch, *Phys. Rev. Lett.*, 58, 2059-2062 (1987)

[17] E. Yablonovitch, *J. Opt. Soc. Am.*, 283-295 (1993)

[18] S. G. Johnson, P. R. Villeneuve, S. Fan, J. D. Joannopoulos, *Phys. Rev. B*, 62, 8212-8222 (2000)

[19] T. A. Birks, J. C. Knight, P. St. J. Russell, *Opt. Lett.*, 22, 961-963 (1997)

[20] R. F. Cregan, B. J. Magan, J. C . Knight, T. A. Birks, P. St. J. Russell, P. J. Roberts. D. C. Allan, *Science*, 285, 1573-1539 (1999)

[21] J. K. Ranka, R. S. Windeler, A. J. Stentz, *Opt. Lett.*, 25, 25-27 (2000)

[22] F. Benabid, J. C. Knight, P.St. J. Russell, *Optics Express*, 10, 1195-1203 (2002)

[23] K. M. King, K. Framptom, T. M. Monro, R. Moore, T. Tucknott, D. W. Hewak, D. J. Richardson, H. N. Rutt, *Electronic Letters*, 38, 546-547 (2002)

[24] V. V. R. K. Kumar, A. K. George, J. C. Knight, P. St. J. Russell, *Opt. Express*, 11, 2641-2645 (2003)

[25] E. Couny, F. Benabid, P. S. Light, *Opt. Lett.*, 31, 3574-3576 (2006)

[26] J. W. Fleming, D. L. Wood, *Applied Optics*, 22, 3102-3104 (1983)

[27] J. B. Keller, Bulletin of the American Mathematical Society, 85, 727-750 (1978)

[28] R. Buczynski, *Acta Physica Polonica A*, 106, 141-167 (2004)

[29] J. M. Dudley, G. Genty, S. Coen, *Rev. Mod, Phys.*, 78, 1135-1184 (2006)

[30] H. Ebendorff-Heidepriem, P. Petropoulos, S. Asimakis, V. Finazzi, R.C. Moore, K. Frampton, F. Koizumi, D.J. Richardson, T.M. Monro, *Opt. Express*,12, 5082-5087 (2004)

[31] V. V. R. K. Kumar, A. K. George, W. H. Reeves, J. C Knight, P. St. J. Russell, 1520-1525 (2002)

[32] J. Y. Y. leong, P. Petropoulos, J. H. V. Price, H. Ebendorff-Heidepriem, S. Asimakis, R. C. Moore, K. E. Frampton, V. Finazzi, X. Feng, T. M. Monro, D. J. Richardson, *Journal of Lightwave Technology*, 24, 183-190 (2006)

[33] K. Kurokawa, K. Nakajima, K. Tsujikawa, T. Yamamoto, K. Tajima, *Journal of Lightwave Technology*, 27, 1653-1662 (2009)

[34] A. S. Webb, F. Poletti, D. J. Richardson, J. K. Sahu, *Optical Engineering*, 46, 1-3 (2007)

[35] R. K. Nubling, J. A. Harrington, *Applied Optics*, 34, 327-380 (1996)

[36] R. L. Kozodoy, A. T. Pagkalinawan, J. A. Harrington, *Applied Optics*, 35, 1077-1082 (1996)

[37] J. Dai, J. A. Harrington, *Applied Optics*, 36, 5072-5077 (1997)

[38] T. G. Euser, G. Whyte, M. Scharrer, J. S. Y. Chen, A. Abdolvand, J. Nold, C.F. Kaminski, P. St. J. Russell, *Opt. Express*,16, 17972-17981 (2008)

[39] G. Humbert, J. C. Knight, G. Bouwmans, P. St. J. Russell, D. P. Williams, P. J. Roberts, B. J. Magan, *Opt. Express*, 12, 1477-1484 (2004)

[40] P. J. Roberts, F. Couny, H. Sabert, B. J. Magan, D. P. Williams, L. Farr, M. W. Mason, T. A. Birks, J. C. Knight, P. St. J. Russell, *Opt. Express*, 13, 236-244 (2005)

[41] T.D. Hedley, D. M. Bird, F. Benabid, J. C. Knight, P. St. J. Russell, *QELS* (2003)

[42] G. J. Pearce, G. S. Wiederhecker, C. G. Poulton, S. Burger, P. St. J. Russell, *Opt. Express*, 15, 12680-12685 (2007)

[43] A. Argyros, J. Pla, *Opt. Express*, 15, 7713-7719 (2007)

[44] F. Couny, F. Benabid, P. S. Light, *Opt. Lett.*, 31, 3574-3576 (2006)

[45] L. Chen, G. J. Pearce, T. A. Birks, D. M. Bird, *Opt. Express*, 19, 6945-6956 (2011)

[46] Y. Y. Wang, N. V. Wheeler, F. Couny, P. J. Roberts, F. Benabid, *Opt. Lett.*, 36, 669-671 (2011)

[47] R. R. Gattass, E. Mazur, *Nature Photonics*, 2, 219-225 (2008)

[48] E. A. J. Marcatili, R. A. Schmeltzer, *Bell System Technical Journal*, 43, 1783-1809 (1964)

[49] T.A. Birks, D. M. Bird, T. D. Hedley, J. M. Pottage, P. St. J. Russell, *Opt. Express*, 12, 69-74 (2004)

[50] G. Antonopoulos, F. Benabid, T. A. Birks, D. M. Bird, J. C. Knight, P. St. J. Russell, *Opt. Express*, 14, 3000-3006 (2006)

[51] B. V. Zhmud, F. Tiberg, K. Hallstensson, *Journal of Colloid and Interface Science*, 228, 263-269 (2000)

[52] K. Nielsen, D. Noordegraaf, T. Sørensen, A. Bjarklev, T. P. Hansen, *J. Opt. A: Pure Appl. Opt.*, 7, L13-L20 (2005)

[53] J. M. Fini, *Meas. Sci. Technol.*, 15 1120-1128 (2004)

[54] G. S. Hartley, *Nature*, 140, 281, (1937)

[55] M. W. Mosher, J. M. Ansell, *J. Chem. Educ.*, 52, 195-196 (1975)

[56] K. G. Yager, C. J. Barrett, *J. Photochem. Photobiol. A: Chemistry*, 182, 250-261 (2006)

[57] M. Irie, *Chem. Rev.*, 100, 1683-1684 (2000)

[58] M. B. Sponsler, *Optical Sensors and switches, (Eds: V. Ramamurthy, K. S. Schanze)*, Marcel Dekker, New York and Basel, 2001, chapter 8

[59] R. H. El Halabieh, O. Mermut, C. J. Barrett, *Pure Appl. Chem. 76. 1445-1465 (2004)*

[60] V. Balzani, A. Credi, M. Venturi, *Pure Appl. Chem.*, 75, 541-547 (2003)

[61] A. A. Beharry, G. A. Woolley, *Chem. Soc. Rev.*, 40, 4422-4437 (2011)

[62] Tait, K. M., *University of Edinburgh* (2005)

[63] P. Atkins, J. De Paula, *Atkins' Physical Chemistry, 8th Edition*

[64] J. R. Lakowicz, *Principles of Fluorescence Spectroscopy, 3rd Edition*

[65] N. Wazzan, *University of Edinburgh* (2009)

[66] M. Poprawa-Smoluch, J. Baggerman, H. Zhang, H. P. A. Maas, L. De Cola, and A. M. Brouwer, *J. Phys. Chem. A*, 110, 11926-11937 (2006)

[67] T. Fujino, S. Yu. Arzhantsev, and T. Tahara, *Bull. Chem. Soc. Jpn*.,75, 1031–1040 (2002)

[68] J. Wachtveitl, T. Nägele, B. Puell, W. Zinth, M. Krüger, S. Rudolph-Böhner, D. Osterhelt, L. Moroder, *J. Photochem. Photobiol A: Chem.*, 105, 283-288 (1997)

[69] I. K. Lednev, T. Q. Ye, P. Matousek, M. Towrie, P. Foggi, F. V. R. Neuwhal, S. Umapathy, R. E. Hester, J. N. Moore, *Chem. Phys. Lett.*, 290, 68-74 (1998)

[70] A. Cembran, F. Bernardi, M. Garavelli, L. Gagliardi, G. Orlandi, *J. Am. Chem. Soc.*, 126, 3234-3243 (2004)

[71] M. L. Tiago, S. Ismail-Beigi, S. G. Louie, *J. Chem. Phys.*, 122, 094311-1-7 (2005)

[72] A. Yamaguchi, N. Nakagawa, K. Igarashi, T. Sekikawa, H. Nishioka, H. Asanuma, M. Yamashita, *Applied Surface Science*, 255, 9864-9868 (2009)

[73] K. M. Tait, J. A. Parkinson, D. I. Gibson, P. R. Richardson, W. J. Ebenezer, M. G. Hutchings, A. C. Jones, *Photochem. Photobiol. Sci.*, 6, 1010-1018 (2007)

[74] S. W. Megennis, F. S. Mackay, A. C. Jones, K. M. Tait, P. J. Sadler, *Chem. Mater.*, 17, 2059-2062 (2005)

[75] Griffiths, J. *Chemical Society Reviews* 1972, *1(4)*, 481-493

[76] B. Valeur, M. N. Berberan-Santos, *J. Chem. Educ.*, 88, 731-738 (2011)

[77] G. G. Stokes, *Philos. Trans.*, 143, 385-398 (1853)

[78] W. A. Bonner, *Rev. Sci. Instruments*, 43, 404

[79] W. B. van Munster, T. W. J. Gadella, *Adv. Biochem. Engin/Biotechnol*,. 95, 143-175 (2005)

[80] E. M. Graham, *University of Edinburgh*, (2007)

[81] C. M. Marian, *WIREs Comput. Mol. Sci.*, 2, 187-203 (2012)

[82] A. Diaspro, G. Chirico, C. Usai, P. Ramoino, J. Dobrucki, *Handbook of Biological Confocal Microscopy, Third Edition* (2006)

[83] M. A. Albota, C. Xu, W. W. Webb, *Appl. Opt.*, 37, 7352-7356 (1998)

[84] G. H. Patterson, D. W. Piston, *Biophysical Journal*, 78, 2159-2162 (2000)

[85] S. Brown, *Nat. Photonics*, 2, 394-395 (2008)

[86] S. Cova, M. Ghioni, A. Lotito, I. Rech, F. Zappa, *J. Mod. Opt.*, 15, 1267-1288 (2004)

[87] P. D. McQueen, S. Sagoo, H. Yao, R. A. Jockusch, *Angew. Chem. Int. Ed.*, 9193-9196 (2010)

[88] R. Sjöback, J. Nygren, M. Kubista, *Spectrochimica Acta. Part A*, 51, L7-L21 (1995)

[89] T. Chang, H. C. Cheung, *J. Phys. Chem.*, 96, 4874-4878 (1992)

[90] F. L. Arbeloa, T. Arbeloa, M. J. T. Estévez, I. L. Arbeloa, *J. Phys. Chem.*, 95, 2203-2208 (1991)

[91] J. J. Shah, M. Gaitan, J. Geist, *Anal.Chem.*,81, 8260-8263 (2009)

[92] K. G. Casey, E. L. Quitevis, *J. Phys. Chem.* 92, 6590-6594 (1988)

[93] D. A. Mendels, E. M. Graham, S. W. Megennis, A. C. Jones, F. Mendels, *Microfluidic Nanofluidic*, 5, 603-617 (2008)

[94] T. A. Smith, M. Irwanto, D. J. Haines, K. P. Ghiggino, D. P. Millar, *Colliod Polym. Sci.*, 276, 1032-1037 (1998)

[95] D. Phillips, *Photochem. Photobiol. Sci.*,9, 1589-1596 (2010)

[96] D. Gust, T. A. Moore, A. L. Moore, *Acc, Chem. Res.*, 42, 1890-1898 (2009)

[97] F. Li, S. H. Lee, J. H. Kim, C. B. Park, *Lab Chip, 11, 2309-2311 (2011)*

[98] H. C. Hunt, J. S. Wilkinson, *Microfluidic Nanofluidic*, 4, 53-79 (2008)

[99] P. Anzenbacher, Jr & M. A. Placios, *Nat. Chem.*, 1, 80-86 (2009)

[100] C. Monat, P. Domachuk, C. Grillet, M. Collins, B. J. Eggleton, M. Cronin-Golomb, S. Mutzenich, T. Mahmud, G. Rosengarten, A. Mitchell, *Mirofluidic Nanofluidic*, 4, 81-95 (2008)

[101] C. Monat, P. Domachuk, B. J. Eggleton, *Nat. Photonics*, 1, 106-114 (2007)

[102] V. R. Horowitz, D. D. Awschalom, S. Pennathur, *Lab Chip*, 8, 1856-1863 (2008)

[103] P. Measor, B. S. Phillips, A. Chen, A. R. Hawkins, H. Schmidt, *Lab Chip*, 11, 899-904 (2011)

[104] C. M. B. Cordeiro, M. A. R. Franco, C. J. s. Matos, F. Sircilli, V. A. Serrão, C. H. B. Cruz, *Opt. Lett.*, 32, 3324-3326 (2007)

[105] Y. L. Hoo, W. Jin, H. L. Ho, D. N. Wang, *Opt. Eng.*, 41, 8-9 (2002)

[106] C. M.B. Cordeiro, M. A. R. Franco, G. Chesini, E. C. S. Barretto, R. Lwin, C. H. B. Cruz, M. C. J. Large, *Opt. Exp.*, 14, 13056-13066 (2006)

[107] T. G. Euser, J. S. Y. Chen, M. Scharrer, P. St. J. Russell, N. J. Farrer, P. J. Sadler, *J. Appl. Phys.*, 103, 103108 (2008)

[108] G. J. Pearce, J. M. Potrttage, D. M. Bird, P. J. Roberts, J. C. Knight, P. St. J. Russell, *Opt. Exp.*, 13, 6937-6946 (2005)

[109] J. S. Y. Chen, T. G. Euser, N. J. Farrer, P. J. Sadler, M. Scharrer, P. st. J. Russell, *Chem. Eur. J.*, 16, 5607-5612 (2010)

[110] A. Khetani, M. Laferriere, H. Anis, J. C. Scaino, *J. Mater. Chem.*, 18, 4769-4774 (2008)

[111] K. M. Tait, J. A. Parkinson, S. P. Bates, W. J. Ebenezer, A. C. Jones, *J. Photochem. Photobiol. A: Chemistry*, 154, 179-188 (2003)

[112] N. A. Wazzan, P. R. Richardson, A. C. Jones, *Photochem. Photobiol. Sci.*, 9, 968-974 (2010)

[113] C. Toro, A. Thibert, L. De Boni, A. E. Masunov, F. E. Hernández, *J. Chem. B.*, 112, 929-937 (2008)

[114] K. Baba, H. Ono, E. Itoh, S. Itoh, K. Noda, T. Usui, K. Ishihara, M. Inamo, H. D. Takagi, T. Asano, *Chem. Eur. J.*, 12, 5328-5333 (2006)

[115] S. R. Hair, G. A. Taylor, L. W. Schultz, *J. Chem. Edu.*, 67, 709-712 (1990)

[116] S. Kobayashi, H Yokoyama, H. Kamei, *Chem. Phys. Lett.*, 138, 333-338 (1987)

[117] K. Gille, H. Knoll, K. Quitzsch, *Int. J. Chem. Kinet.*, 31, 337-350 (1999)

[118] P. D. Wildes, J. G. Pacifici, G. Irick, Jr., D. G. Whitten, *J. Am. Chem. Soc.* 93, 2004-2008 (1971)

[119] T. Asano, T. Okada, *J. Org. Chem*, 49, 4387-4391 (1984)

[120] T. Asano, T. Okada, S. Shinkai, K. Shigematsu, Y. Kusano, O. Manabe, *J. Am. Chem. Soc.* 103, 5161-5165 (1981)

[121] H. M. D. Bandara and S. C. Burdette, Chem Soc Rev, 2012 DOI:10.1039/c1cs15179g;

[122] G. Gabor, E. Fischer, *J. Phys. Chem.*, 75, 581-583 (1971)

[123] M. D. Nielsen, N. A. Mortensen, J. R. Folkenberg, A. Bjarkev, *Opt. Lett.*, 28, 2309-2311 (2003)

[124] N. A. Mortensen, J. R. Folkenberg, M. D. Nielsen, K. P. Hansen, *Opt. Lett.*, 28, 1879-1881 (2003)

[125] X. Jiangm, T. G. Euser, A. Abdolvand, F. Babie, N. Joly, P. St. J. Russell, *Conference on Lasers and Electro-Optics Europe (CLEO Europe)*, 22-26 May (2011)

[126] J. Shan, S. Xu, W. Shi, L. Liu and L. Xu, "Control of Photoisomerization Quantum Efficiency by Metallic Nanostructures," in Laser Science, OSA Technical Digest (CD) (Optical Society of America, 2010), paper LTuA6

[127] J. Dokic, M. Gothe, J. Wirth, M. V. Peters, J. Schwarz, S. Hecht, P. Saalfrank, *J. Phys. Chem.* A, 2009, 113, 6763–6773.

[128] S. Weiss, *Science*, 283, 1676-16**8**3 (1999)

[129] B. A. Flusberg, E. D. Cocker, W. Piyawattanametha, J. C. Jung, E. L. M. Cheung. M .J. Schnitzer, *Nat. Meth.* 2, 941-950 (2005)

[130] J. Ma, W. J. Bock, *IEEE Transactions on Instrumentation and Measurement*, 57, 2813-2818 (2008)

[131] T. Fujii, Y. Taguchi, T. Saiki, Y. Nagasaka, *Sensors*, 11, 8358-8369 (2011)

[132] S. K. Vengalathundakal, V. M. Murukeshan, S. Padmanabhan, P. Padmanabhan, *Optical Engineering*,48, 103601 (2009)

[133] M. T. Myaing, J. Y. Ye, T. B. Norris, T. P. Thomas, J. R. Baker, W. J. Wadsworth, G. Bouwmans, J. C. Knight, P. St. J. Russell, *Proceedings of SPIE*, 5317 (2004)

[134] Y. Chang, J. Y. Ye, T. Thomas, Y. Chen, J. R. Baker, T. B. Norris, *Opt. Exp.*, 16, 12640-12649 (2008)

[135] F. Knorr, D. R. Yankelevich, J. Liu, S. Wachsmann-Hogiu, L. Marcu, *J. Biophotonics*, 5, 14-19 (2012)

[136] S. O. Konorov, A. M. Zheltikov, M. Scalora, *Opt. Epress*, 13, 3454-3459 (2005)

[137] J. B. Jenson, P. H. Hoiby, L. H. Pedersen, A. Carlson. L. B. Nieslsen, A. Bjatklev, T. P. Hansen, *Proceedings of SPIE.* Vol. 5317 (2004)

[138] S. Smolka, M. Barth, O. Benson, *Opt. Express*, 15, 12783-12791 (2007)

[139] V. K. Shinoj, V. M. Murukeshan, *Opt. Photonics. J.* 1, 85-90, (2011)

[140] S. Padmanabhan, V. Shinoj, V. M. Murukeshan, *J. Biomedical Opt.*, 017005-1-6 (2010)

[141] J. B. Jensen, P. E. Hoiby, L. H. Pedersen, J. R. Folkenberg, A. Bjarklev, *Conference on Lasers and Electro-Optics Europe (CLEO Europe)*, (2004)

[142] Y. Peng, Y. Cheng, *Proceedings of SPIE.* Vol. 5381, 73810G-1 (2009)

[143] B. Larrión, M. Hernáez, F. J. Arregui, J. Goicoechea, J. Bravo, I. R. Matias, *Journal of Sensors*, 1-6 (2009)

[144] M. S. Rutowska, F. C. G. Gunning, F. Kivleham, E. Moore, D. Brennan, P. Galvin, A. D. Ellis, *Meas. Sci. Technol.*, 21, 1-8 (2010)

[145] S. Smolka, M. Barth, O. Benson, *Appl. Opt. Lett.*, 90, 111101, 1-3 (2007)

[146] K. Tanaka, T. Miura, N. Umezawa, Y. Urano, K. Kikuchi, T. Higuchi, T. Nagano, *J. Am. Chem. Soc*, 123, 2530-2536 (2001)

[147] C. Xu, W. W. Webb, *J. Opt. Soc. Am. B.*, 13, 481-491 (1996)

[148] C. J. Dalzell, T. P. J. Han, I. S. Ruddock, *IEEE Sensors Journal*, 12, 164-167 (2012)

[149] O. Kazuya, K. Yoshiaki, *Anticancer Agents Med. Chem.*, 8, 269-279 (2008)

[150] T. M. Monro, D. J. Richardson, P. J. Bennett, *Electronic Lett.*, 35, 1188-1189 (1999)

[151] G. Gade, Th. Porada, *J. Photochem. Photobiol. A: Chem.*, 107, 27-34 (1997)

Publications

Papers

Williams, G. O. S., Chen, J. S. Y., Euser, T. G., Russell, P. S. J. and Jones, A. C., "Photonic crystal fiber as an opto-fluidic micro-rector for sub pico-litre photochemical kinetics" Lab Chip, 12, 3356-3361, (2012)

Williams, G. O. S., Euser, T. G., Russell, P. S. J. and Jones. A. C., "Spectrofluorimetry with Attomole Sensitivity in Photonic Crystal Fibre", *In press*, Methods and Applications in Fluorescence, (2013)

Williams, G. O. S., Euser, T. G., Arlt. J., Russell, P. S. J. and Jones, A. C., Long path length nano-molar two-photon fluorescence excitation utilising photonic crystal fiber. (in prep)

Abstracts

Williams, G. O. S., Euser, T. G., Chen, J. S. Y., Russell, P. S .J., Fluorescence Spectroscopy in Photonic Crystal Fiber CLEO/Europe and EQEC 2011 Conference Digest, OSA Technical Digest, 2011, paper CH4_4

Chen, J. S. Y., Euser, T. G., Williams, G. O. S., Jones, A. C., Russell, P. S. J., Photoswitching in Photonic Crystal Fiber, Optical Sensors, OSA Technical Digest, 2010, paper SThB4

Presented at the Royal Society of Chemistry Photochemistry Group Meeting, Dublin, Ireland, 16 th-18th May 2011